Quantum Synchronisation of Molecular Motions in Bio-Inspired Energy Transfer Systems

Stefan Siwiak-Jaszek

A dissertation submitted in partial fulfillment

of the requirements for the degree of

Doctor of Philosophy

of

University College London.

Department of Physics and Astronomy

University College London

August 6, 2019

I, Stefan Siwiak-Jaszek, confirm that the work presented in this thesis is my own. Where information has been derived from other sources, I confirm that this has been indicated in the work.

Abstract

Synchronisation is a collective phenomenon extensively studied in classical oscillators and, more recently, in quantum systems. The precise mechanisms of the phenomena in the latter regime remain unclear. In this thesis we investigate the fundamental mechanisms of quantum synchronisation through the theoretical analysis of a bio-inspired energy transfer system.

Firstly, we numerically explore the oscillatory displacements of underdamped intramolecular vibrations in a vibronic dimer during energy transfer with Markovian decoherence and dissipation. We reveal that the vibrations synchronise in the timescale of the energy transfer process. We show that this synchronisation depends on the survival of specific vibronic coherences and explain how the competition between coherent and dissipative processes promotes synchronising coherences. We show that the time taken for synchronisation to emerge is positively correlated with fast coherent energy transport.

Secondly, we investigate how the synchronisation dynamics of these vibrational motions contain signatures of quantum properties of the system. We reveal that a transient negatively synchronised period is a signature of excitonic coherence dominating the dynamics. We show that synchronisation with a constant phase difference occurs and is proportional to the detuning between the energies of the vibrations. We show that this may be a general feature of quantum synchronisation with detuning. Furthermore we show that this phase difference is correlated with a reduction in quantum correlations between synchronising subsystems. This result implies that our measure of synchronisation could be used as an indirect measure of a purely quantum property.

Finally, we investigate synchronisation in the presence of non-Markovian environments and show that non-Markovian effects can be both beneficial and detrimental to synchronisation.

Impact Statement

The research presented in this thesis contributes separately to two distinct academic fields: the first which explores the nature of synchronisation phenomena in the quantum regime and the second which aims to highlight the role of quantum coherence in bio-inspired energy transfer processes.

To the former it contributes novel physical insight into the underlying mechanisms of synchronisation in the quantum regime and the roles that quantum coherence plays; it introduces a new setting in which we show synchronisation to be present and connected to a possible biological function; it contributes the first investigation of transient spontaneous synchronisation in the presence of non-Markovian environments; it contributes an adaptation to a synchronisation measure [24] that, to our knowledge, has not been used as a dynamical measure of phase in this setting before. Together these may have impact in the future design of quantum technologies due to their contribution to understanding of the control of quantum states. To the latter it contributes a novel perspective from which to explore the role of exciton-vibration coherences; it reinforces the importance of molecular motions in electronic energy transfer and gives further motivation to experimentally investigate the phenomena.

Code written for the calculations in this thesis may continue to be used for research as they are applicable to a range of problems in open quantum systems. Content from this thesis will be submitted for publication in peer-review journals. During the research period for this thesis the author developed and delivered multiple outreach projects based on topics from the field. Work from this thesis will continue to be used for teaching and outreach in the future.

Contents

Chapter 1

Introduction

Synchronisation can be broadly defined as the adjustment of rhythms of oscillating objects due to their weak interaction [61]. This description corresponds to numerous processes throughout the natural world that occur on a wide range of length and time scales. This is especially true in living systems, where synchronisation is common and is often closely related to biological function [7, 50]. On the metre scale, the synchronous flashing of male fireflies aids each individual in reproduction [7] and on the micrometre scale, cardiac cells synchronise contractions with their neighbours [50]. The question of whether this phenomenon persists on even smaller length scales such as that of individual biomolecules (nanometre) and time scales such as the relaxation times of intramolecular motions (picoseconds) has not been investigated. On these length and time scales quantum phenomena cannot be neglected and synchronisation, if it occurs, could exhibit features that have no equivalence in the classical regime [26, 33, 40, 43, 63, 83].

An interesting natural setting in which one can explore synchronisation in the quantum regime and at the same time investigate its possible relations to biological function, is the widely studied electronic excitation transport (ET) process in photosynthetic complexes. Whether molecular motions can synchronise during the transport process, and if this aids in any way biological function are open questions to be investigated. Using quantum synchronisation as a lens through which we explore the quantum dynamics of bio-inspired vibronic dimers, and vice versa, are the central focuses of this work.

1.1 Quantum Synchronisation

Investigations of synchronisation in the quantum regime are often focused on searching for features that are different from the classical version of the phenomena. Examples of these unique aspects include: the 'synchronisation blockade' [43], which predicts that in the deep-quantum regime synchronisation can be inhibited if the frequencies of two oscillating objects are too close; and a step-like transition to synchronisation [83] as a function of increasing coupling strength of oscillators, which differs from the smooth transition in the classical case. However, motivation for studying quantum synchronisation also comes from its importance in experimental and technological applications. Electromagnetic modes, trapped ions and nano-electromechanical resonators can all be represented, to a first approximation, as coupled oscillators. Therefore understanding quantum synchronisation phenomena fundamentally, especially its predictable control of quantum states, may provide future design principles of experimental and technological set-ups [44]. However, experimental exploration of quantum synchronisation is not yet common. Reports of observations are limited to polariton condensates [2, 89] and micrometer scale opto-mechanical oscillators [90] in the near-quantum regime. Theoretical studies predict observations are within reach in trapped ions. For example: quantum synchronisation could be indirectly measured through spin states [33]; and the phase-locking of oscillations are predicted to be stronger in a quantum model than in the classical model [40]. Investigation into quantum synchronisation is therefore primarily computational and theoretical. In this thesis we also proceed with theoretical and computational analysis.

The form of synchronisation that we focus on is best described as *transient*, emphasising the transience of the phenomenon before relaxation to the steady state, and *spontaneous*, emphasising the spontaneity of synchronisation occurring solely due to the interactions within the quantum system considered and specifically not due to the influence of an external fixed-frequency driving force [25]. This point is to emphasise the difference from studies of quantum synchronisation where self-sustaining oscillations are essential [42, 43, 83, 84]. Transient spontaneous quantum

synchronisation (referred to from here on as synchronisation) has been recently investigated in a range of open quantum systems [3, 25, 27, 44, 48]. In the simplest case of coupled two-level systems (TLSs), it has been shown that synchronisation cannot occur in the presence of dephasing channels alone and dissipation appears to be essential [27]. In quantum harmonic oscillator (QHO) networks, adjusting the coupling between oscillators can create asymptotically synchronised states that avoid dissipation altogether [44]; and in hybrid TLS-QHO systems the form of coupling of QHOs to TLSs can induce and control synchronisation between QHOs with a well-defined phase difference [48].

Across these cases there are multiple explanations given for the mechanism of synchronisation. Some relate synchronisation to the survival of a specific eigen-mode of the system-environment interaction that dominates dynamics after a short evolution from the initial state [25, 27]. This eigenmode is one in which the desired observables are synchronised. Others provide analytic equations for the emergence of synchronisation and reveal its dependence on coupling strength, initial state and mode frequencies [26, 48].

Within this literature there is a need for a more physically insightful explana-tion of the mechanism of synchronisation that includes a description of the quantum states, coherences and dissipation processes. An eigenmode analysis alone fails to explain why a specific mode exhibits synchronisation or lives for a long time, and the analytic solutions are only for specific solvable cases. In this thesis we aim to contribute a new perspective on the mechanism of synchronisation in open quan-tum systems. Specifically we present a detailed analysis of the early-time dynamics of synchronisation, which are often overlooked as an incoherent transient. At this timescale coherent and dissipative processes overlap and have a complex relation-ship, an analysis of which can give insight into the mechanism of synchronisation.

1.2 Photosynthetic Pigment Protein Complexes

Photosynthetic light-harvesting proteins exhibit complex ET dynamics due to an overlap of energy scales in electronic and vibrational degrees of freedom and the timescales of their associated coherent and incoherent processes. Experiments and theory suggest that these complexes are capable of sustaining quantum coherence at room temperature lasting several hundred femtoseconds [14, 20, 22, 29, 59, 67, 74]. The leading hypothesis for the mechanism underlying long-lived coherent dynamics in these biophysical systems is the quantum mechanical exchange of energy between excitonic and vibrational degrees of freedom [10, 11, 17, 22, 31, 39, 52, 58, 65, 67]. Despite some controversy surrounding the observations [19], there remains a widespread interest in understanding the intertwined dynamics of electronic and vibrational motions during energy transfer.

Excitonic spectra from the photosynthetic pigment-protein Fenna-Matthews-Olson complex have recently been observed to exhibit synchronous oscillations [66]. Although this is not an observation of the synchronisation process, it suggests that synchronisation phenomena may be relevant in these settings. An early fluorescence depolarisation study of Light Harvesting Complex 1 from photosynthetic bacteria Rhodobacter Sphaeroides [5] shows spectral motions initially out-of-phase shift to in-phase during ET. These motions were later modelled theoretically where they were attributed to excited state vibrational coherence [13]. However, the potential synchronisation dynamics of these motions were not analysed. The literature is lacking an in-depth theoretical modelling of vibrational synchronisation in photosynthetic ET. This thesis attempts to address this gap.

1.3 Contribution of this work

This thesis aims to investigate in-depth the synchronisation of molecular motions in a bio-inspired vibronic dimer. It aims to contribute further understanding to both the quantum dynamics of bio-inspired dimers and the fundamental mechanisms involved in quantum synchronisation.

The thesis is organised as follows: in Chapter 2 we introduce the bio-inspired dimer model we use throughout the thesis and characterise its important dynamics; in Chapter 3 we delve into the synchronisation of molecular motions in the excited state dynamics, explain the underlying mechanism with exciton-vibration coherences and demonstrate its connection to coherent excitation transfer; in Chapter 4 we explore the dynamics of synchronisation as a function of the frequency difference between molecular vibrations and reveal that our synchronisation measure can indicate changes in quantum correlations between synchronising subsystems; in Chapter 5 we couple the dimer to a more realistic non-Markovian environment and explore its impact on synchronisation using the Hierarchical Equations of Motion; in Chapter 6 we summarise and conclude.

Chapter 2

Energy Dynamics of a Bio-Inspired Vibronic Dimer

2.1 The Exciton-Vibration Dimer

In this section we introduce the Hamiltonian description of a bio-inspired vibronic dimer which we call the Exciton-Vibration Dimer Model [39, 58]. We describe the initial state and parameters used throughout the thesis.

2.1.1 Hamiltonian Description

Consider a pair of chromophores with single excited states $|e_{i=1,2}\rangle$ of energy $e_{i=1,2}$ interacting via dipole-dipole coupling of strength V and each locally coupled to an intramolecular vibration (modelled as a QHO) of energy $\omega_1 = \omega_2 = \omega$ (throughout the thesis we set $\hbar$ to 1) and coupling strength $g_1 = g_2 = g$. The system has a total Hamiltonian of the form:

$$H = H_{el} + H_{vib} + H_{el-vib} \tag{2.1}$$

The electronic Hamiltonian reads:

$$H_{el} = e_1|e_1\rangle\langle e_1| + e_2|e_2\rangle\langle e_2| + V^*|e_2\rangle\langle e_1| + V|e_1\rangle\langle e_2| \tag{2.2}$$
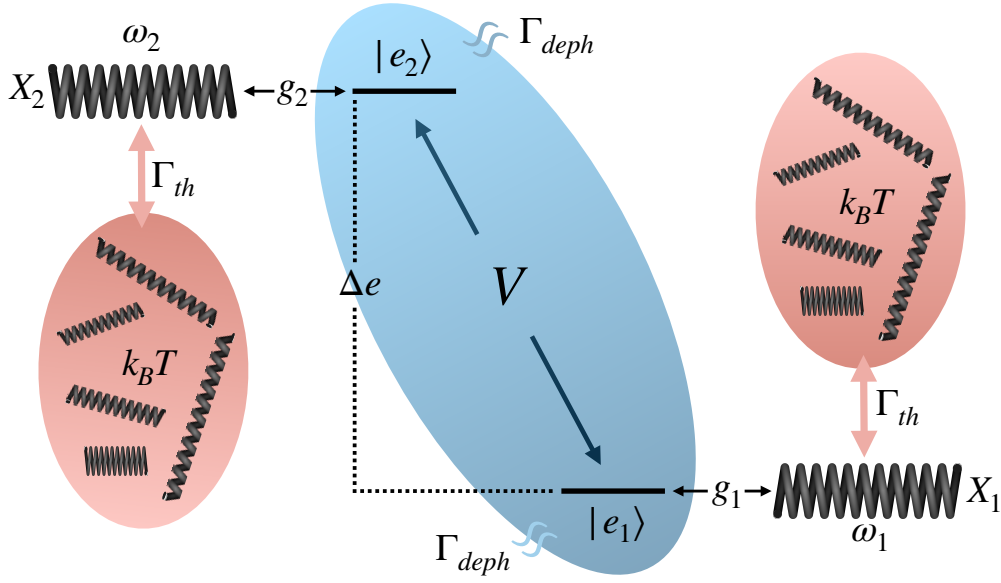
Figure 2.1: Schematic diagram of the bio-inspired vibronic dimer studied throughout this thesis. Two chromophores (subscripts 1 and 2) with single excited states $|e_i\rangle$ interact via dipole-dipole coupling of strength V. Each electronic state is coupled linearly with strength g_i, to an intramolecular mode of energy ω_i. The electronic subsystem (blue oval) experiences dephasing at rate Γ_{deph}, each mode dissipates into a separate thermal bath (red oval) of temperature $k_B T$ at a rate Γ_{th}.

Then defining $|e_1\rangle = \begin{pmatrix} 1 \\ 0 \end{pmatrix}$ and $|e_2\rangle = \begin{pmatrix} 0 \\ 1 \end{pmatrix}$ we can present H_{el} as a matrix:

$$H_{el} = \begin{pmatrix} e_1 & V \\ V^* & e_2 \end{pmatrix} \tag{2.3}$$

The eigenstates of H_{el} are delocalised electronic states known as excitons, which we label $|E_{d=1,2}\rangle$, and have energies:

$$\begin{aligned} E_1 &= \frac{1}{2}\left(e_1 + e_2 - \sqrt{\Delta e^2 + 4|V|^2}\right) \\ E_2 &= \frac{1}{2}\left(e_1 + e_2 + \sqrt{\Delta e^2 + 4|V|^2}\right) \end{aligned} \tag{2.4}$$

where $\Delta e = e_2 - e_1$ and $|V| = \sqrt{VV^*}$.

The unitary rotation $U(\theta)$ which diagonalises H_{el} to create an excitonic Hamiltonian $H_{exc} = U(\theta)H_{el}U^{\dagger}(\theta)$ has the form [47]:

$$U = \begin{pmatrix} \cos\theta & \sin\theta \\ -\sin\theta & \cos\theta \end{pmatrix} \tag{2.5}$$

where $\theta = \frac{1}{2}\arctan(2|V|/\Delta e)$ is an effective measure of delocalisation of the electronic sub-system. This is easy to see by considering, for example, $\theta = 0$ which corresponds to a Hamiltonian in which delocalised states do not exist. After diagonalisation the resultant excitonic Hamiltonian has the form:

$$H_{exc} = E_1|E_1\rangle\langle E_1| + E_2|E_2\rangle\langle E_2| = \begin{pmatrix} E_1 & 0 \\ 0 & E_2 \end{pmatrix} \tag{2.6}$$

The bare vibrational Hamiltonian reads:

$$H_{vib} = \omega b_1^{\dagger}b_1 + \omega b_2^{\dagger}b_2 \tag{2.7}$$

where $b_{i=1,2}^{\dagger}(b_{i=1,2})$ are the creation (annihilation) operators for the modes. The eigenstates of H_{vib} are Fock states which we write as: $|n_1\rangle \otimes |n_2\rangle$, where n_1 and n_2 are vibrational quanta in mode 1 and mode 2 respectively. The matrix representation of the bosonic creation operator depends on the maximum occupation number M in each mode. It has the general form:

$$b = \begin{pmatrix} 0 & \sqrt{1} & 0 & 0 & \cdots & 0 \\ 0 & 0 & \sqrt{2} & 0 & \cdots & 0 \\ 0 & 0 & 0 & \sqrt{3} & \cdots & 0 \\ 0 & 0 & 0 & 0 & \cdots & \vdots \\ \vdots & \vdots & \vdots & \vdots & \ddots & \sqrt{M-1} \\ 0 & 0 & 0 & \cdots & 0 & 0 \end{pmatrix} \tag{2.8}$$

The interaction Hamiltonian reads:

$$H_{el-vib} = g|e_1\rangle\langle e_1|\left(b_1 + b_1^\dagger\right) + g|e_2\rangle\langle e_2|\left(b_2 + b_2^\dagger\right) \tag{2.9}$$

where we have assumed a linear coupling between electronic and vibrational degrees of freedom [64, 68]. We define the electronic operators in the exciton basis as $\Theta_i = U(\theta)|e_i\rangle\langle e_i|U^\dagger(\theta)$ and insert into H_{el-vib} to give:

$$H_{exc-vib} = g\Theta_1\left(b_1 + b_1^\dagger\right) + g\Theta_2\left(b_2 + b_2^\dagger\right) \tag{2.10}$$

The final exciton-vibration Hamiltonian is then:

$$\begin{aligned} H = &+ E_1|E_1\rangle\langle E_1| + E_2|E_2\rangle\langle E_2| \\ &+ \omega b_1^\dagger b_1 + \omega b_2^\dagger b_2 \\ &+ g\Theta_1 X_1 + g\Theta_2 X_2 \end{aligned} \tag{2.11}$$

where we have introduced the position operator for each mode $X_{i=1,2} = b_i + b_i^\dagger$. The eigenstates of H which we label $|\psi_j\rangle$ are exciton-vibrational (or vibronic) which we can represent in the quasi-local basis as:

$$\begin{aligned} |\psi_j\rangle &= \sum_{d=1,2} \alpha_d|E_d\rangle \otimes \sum_{n_1=1}^{M} \beta_{n_1}|n_1\rangle \otimes \sum_{n_2=1}^{M} \gamma_{n_2}|n_2\rangle \\ &= \sum_{dn_1n_2} c(d,n_1,n_2)|E_d,n_1,n_2\rangle \end{aligned} \tag{2.12}$$

where eigenstates $|\psi_j\rangle$ are labelled in ascending energy.

2.1.2 Density Matrix Representation

The state of a quantum system can be represented using a density matrix which has the general form:

$$\rho = \sum_a p_a|\lambda_a\rangle\langle\lambda_a| \tag{2.13}$$

where p_a is the probability that the system is in pure state $|\lambda_a\rangle$. Using the eigenvectors $|\psi_j\rangle$ of our Hamiltonian we write the density matrix of our system as:

$$\rho(t) = \sum_{jk} \rho_{jk}(t)|\psi_j\rangle\langle\psi_k| \tag{2.14}$$

where $\rho_{jk}(t) = \langle\psi_j|\rho(t)|\psi_k\rangle$ and we have allowed for the time dependence of the system probabilities. We analyse the states of our system in both the eigenbasis of H, $\{|\psi_j\rangle\}$, and the quasi-local exciton-mode-mode basis, $\{|E_d, n_1, n_2\rangle\}$, at different sections of the thesis. We use the quasi-local picture to construct states from the subsystems and to gain physical insight into the effects of Markovian environmental coupling. We use the eigenbasis to understand the dynamics of synchronisation.

The measurement of a general operator O in the density matrix formalism is as follows:

$$\langle O\rangle(t) = Tr\{O\rho(t)\} \tag{2.15}$$

where $Tr\{\}$ is the trace. In figures throughout this thesis the time dependent expectation value of an operator will be labelled simply by the operator in order to compact the notation.

2.1.3 Initial State

Since we are interested in the process of synchronisation during electronic energy transfer, we begin in an excited electronic state, namely the the higher energy excitonic state $|E_2\rangle$. The initial state density matrix for our electronic subsystem is therefore:

$$\rho_{exc} = |E_2\rangle\langle E_2| = \begin{pmatrix} 0 & 0 \\ 0 & 1 \end{pmatrix} \tag{2.16}$$

We set the initial state for both intramolecular modes as the thermal equilibrium state before this excitation i.e. at thermal equilibrium with baths at temperature $T = 298$ K and electronic sites in their ground state. The density matrix that represents

a thermal distribution of Fock states has the form:

$$\rho_i^{th} = \sum_{n_i} \left(1 - e^{\frac{-\omega}{k_B T}} \right) e^{\frac{-n_i \omega}{k_B T}} |n_i\rangle\langle n_i| \quad (2.17)$$

where k_B is the Stefan-Boltzmann constant and T is the temperature. We combine these subsystem density matrices to construct the global initial state:

$$\rho(0) = |E_2\rangle\langle E_2| \otimes \rho_1^{th} \otimes \rho_2^{th} \quad (2.18)$$

2.1.4 Units and Parameters

Dimers in light-harvesting proteins in which intramolecular modes are predicted to be involved in ET exist in the parameter regime where $\Delta E \approx \omega > g > V$. Several examples exist in which Δe is large enough for ET to be interband-like: Crypto-phyte algae proteins Phycoerythrin 545 (PE545) from Rhodomonas CS24 [39] and Phycocyanin-645 (PC645) from Chroomonas CCMP270 [65]; Cyanobacteria pro-teins Allophycocyanin (APC) and C-phycocyanin (CPC) [87] and higher plant pro-tein Light Harvesting Complex II (LHCII) [54]. Whilst the majority of phenomena explored in this thesis are demonstrated with parameters that represent the central dimer in PE545, the methods and findings could easily be extended to any of the systems described above. The parameters are based on experimental values [39, 53] and are displayed in Table 2.1. All energies or rates given in cm^{-1} are spectroscopic wavenumbers.

Δe	V	ω	g	$k_B T$	Γ_{th}	Γ_{deph}
1042	92	1111	267.1	207.1	[1ps]$^{-1}$	[0.1ps]$^{-1}$

Table 2.1: Set of parameters used as a base for numerical calcula-tions throughout this thesis. Extracted from [39, 53] and represents the central dimer in cryptophyte algae protein PE545 ($PEB_{50/61}$). Units in spectroscopic wavenumbers cm^{-1} except final two columns.

These parameters correspond to a mostly localised excitonic system as $\theta = 0.087 \ll \theta_{max} = \frac{\pi}{4}$. As the site-mode coupling strength g is relatively small also, the

vibronic states, $|\psi_j\rangle$, formed by this system are not far from the quasi-local states $|E_d, n_1, n_2\rangle$. This local nature is visualised in Figure 2.2 where the energies of both vibronic and quasi-local states are shown to be very similar. To obtain convergent dynamics we account for a maximum occupation $M = 8$ in each mode.
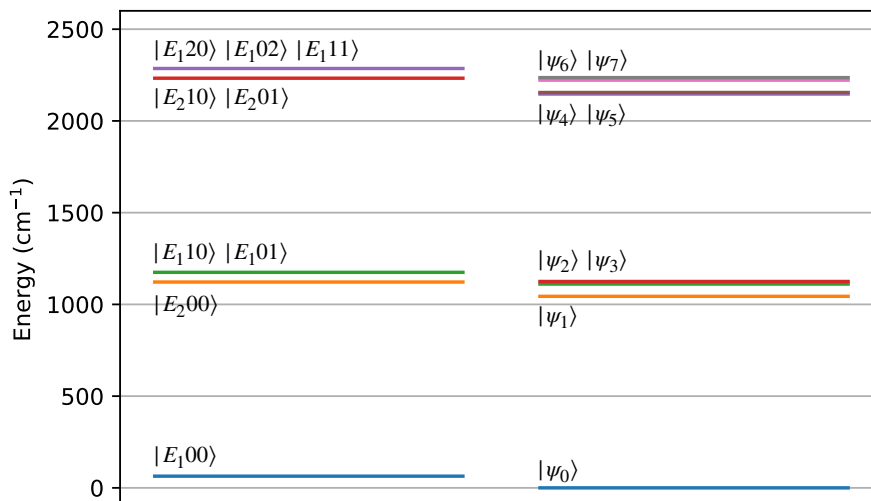
Figure 2.2: Comparison of energies of vibronic eigenstates $|\psi_j\rangle$ and quasi-local picture states $|E_d, n_1, n_2\rangle$ for PE545 parameters listed in Table 2.1. Note that for illustration, the energies are shifted such that the energy of $|\psi_0\rangle$ is set to zero.

2.2 Isolated Hamiltonian Evolution

Any completely isolated quantum system, when initiated in a non-eigenstate of its Hamiltonian, will coherently sample its Hilbert space in a cyclic pattern that depends on the initial state. In the following, the isolated Hamiltonian evolution of the Exciton-Vibration dimer introduced in the previous section is explored.

2.2.1 Solving Time Evolution

The time evolution of an isolated quantum system is described by the Liouville von Neumann equation:

$$\dot{\rho}(t) = -i[H, \rho(t)] \tag{2.19}$$

which is the density matrix form of the time dependent Schrödinger equation. This has the solution:

$$\rho(t) = e^{-iHt}\rho_0 e^{iHt} \tag{2.20}$$

Equation 2.20 can be solved exactly if H can be diagonalised analytically. This would allow exact equations of motion for system observables to be derived and therefore the dynamics of, for example, synchronisation could be determined. In practice however, H is not trivially diagonalisable, especially in systems consisting of multiple degrees of freedom. Exact diagonalisation of exciton-vibration dimers has been demonstrated [4, 21] but for the number of Fock states required for convergent eigenvalues in the parameter regime of PE545 it is not practical. With this considered, the closed system dynamics must be obtained by numerical solution of Equation 2.19.

2.2.2 Coherent transport mechanism

One of the most important features of the prototype system considered is that efficient ET is aided by a resonance in energy between the exciton energy splitting and an energy quanta of the local intramolecular modes [17, 39, 58]. This resonance results in a range of eigenstates $|\psi_j\rangle$ that are close in energy yet in the quasi-local basis $\{|E_d, n_1, n_2\rangle\}$ have significantly different weights (see Figure 2.2). When coherently evolving from the initial state considered (with the excitonic system being initially in the highest-energy exciton state) joint exciton-vibrational transfer pathways are open and population can be coherently transferred to eigenstates involving the lowest lying exciton.

Figure 2.3 displays the coherent evolution of the exciton populations and the absolute value of inter-exciton coherence. The dominant oscillation in exciton populations is due to coherent transition between eigenstates $|\psi_1\rangle$ and $|\psi_3\rangle$ which have an energy difference that corresponds to a frequency with period 0.4 ps. As will be discussed further in Chapter 3, these eigenstates have different weights over each exciton and hence transfer population. This exciton-vibrational coherent transport mechanism is a key feature of the bio-inspired vibronic dimers which we refer to

throughout this thesis.
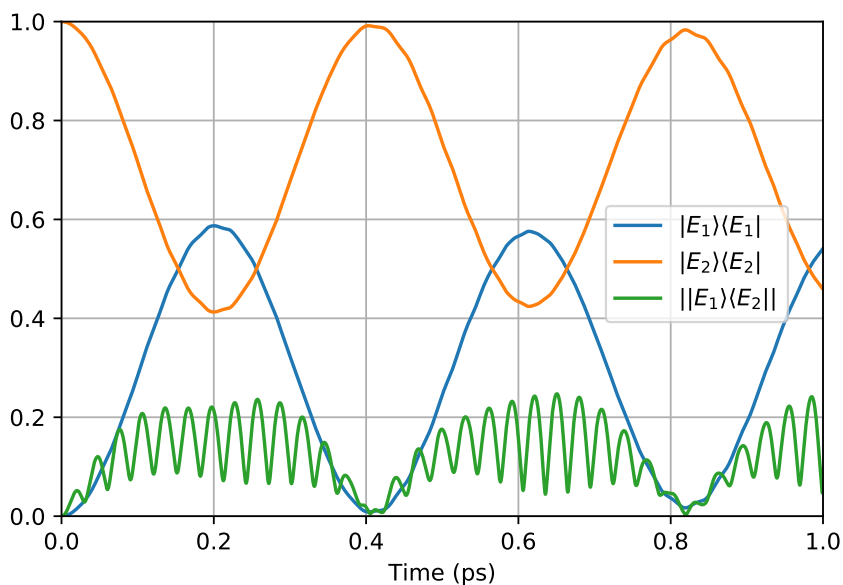
Figure 2.3: Closed system evolution of exciton populations and ab-
solute value of inter-exciton coherence from initial state
Equation 2.18. Measurements are labelled in-figure by
their operator. Notation $||E_1\rangle\langle E_2||$ indicates absolute
value. PE545 parameters listed in Table 2.1.

Additionally we note that the inter-exciton coherence follows the same slow
oscillatory envelope but with an additional fast oscillating component. This fast
oscillation is the natural frequency of the intramolecular modes $\omega = 1111$ cm^{-1}
which has a time period of approximately 0.03 ps and will be investigated in later
chapters.

2.3 Open Quantum Systems

In general, quantum systems are not isolated and interact with a large number of environmental degrees of freedom that limit and destroy coherent evolution of quantum superposition states [6]. However, when the energy scales of the system and system-environment interaction are comparable, and environmental fluctuations exhibit well defined spectral features, the system and environment can enter in a fruitful interplay where coherent superpositions can last long and exhibit a rich dynamics. Indeed, this is what is argued to be the case for electronic excitation transfer in photosynthetic pigment-protein complexes. In the following we introduce the theory to describe a quantum system interacting with a simple environment.

We define a new global Hamiltonian that includes the environment:

$$H_G = H_S + H_E + H_I \tag{2.21}$$

where H_S is the system of interest, H_E is the Hamiltonian of the environment(s) and H_I is the Hamiltonian describing their interactions. Using the Liouville von Neumann equation the equation of motion of the whole system-environment density matrix ρ_G is:

$$\dot{\rho}_G(t) = -i[H_G, \rho_G(t)] \tag{2.22}$$

Considering that realistic environments often consist of an infinite bath of QHOs, Equation 2.22 has many degrees of freedom and is intractable. Instead several methods have been developed to solve the dynamics of the reduced density matrix of the system: $\dot{\rho}_S(t) = Tr_E\{\dot{\rho}_G(t)\}$ that takes into account the effects of the environment but does not keep explicit information on them. The methods can be split into two main branches: Markovian, where the environment is assumed to relax on a time-scale much faster than the system therefore is essentially unchanged by any system interaction and is considered 'memory-less'; and non-Markovian where the environment can interact with the system coherently and its state is changed by its interaction with the system. In the following section we focus only on the former whilst in Chapter 5 we introduce the latter.

2.3.1 Markovian Environment: The Master Equation

A very successful and widely used approximation of the interaction of a reduced system density matrix with an environment is the Lindblad master equation. Its derivation is standard in many quantum mechanics textbooks [6, 47] so here we only state the important approximations and end result. Firstly the derivation assumes that the reduced density matrix $\rho_S(t)$ is separable from the state of the environment ρ_E at all times. This means there are no correlations between the system and environment and is known as the Born approximation. Secondly it assumes that the environment relaxes much faster than the system, i.e. the environment state is unchanged by interactions with the system at any time, therefore the state of the system or environment never depends on a past state of the environment and it is considered 'memory-less'. This is known as the Markov approximation. Using these approximations and a secular approximation the reduced system equation of motion can be cast in the Lindblad form:

$$\dot{\rho}_S(t) = -i[H_S, \rho_S(t)] + D[\rho_S(t)] \tag{2.23}$$

where the Lindblad-form superoperators are:

$$D_\nu[\rho] = \Gamma_\nu \left(O_\nu \rho O_\nu^\dagger - \frac{1}{2} \rho O_\nu^\dagger O_\nu - \frac{1}{2} O_\nu^\dagger O_\nu \rho \right) \tag{2.24}$$

and the choice of operators O_ν at rates Γ_ν can phenomologically describe a variety of environment effects. Finally we note that this model is valid in the regime of weak system-environment coupling relative to the inter-site coupling. In the following sections we introduce two commonly used environment-induced processes.

2.3.2 Pure Dephasing

A particular form of interaction with an environment can be derived in which the system energies are not changed. These processes are known as pure dephasing [6, 28, 47] and can be interpreted from a microscopic perspective as elastic system-environment collisions which only act to shift the phase of the system. For the

Exciton-Vibration Dimer this environment effect is applied to the onsite excited electronic states and has corresponding Lindblad transition operators $|e_1\rangle\langle e_1|$ and $|e_2\rangle\langle e_2|$. Pure dephasing is expected to exponentially decay coherences with the rate Γ_{ph} and in the long time limit it predicts equalisation of all system populations. This latter effect arises from the derivation assuming an infinite temperature bath of harmonic oscillators. Figure 2.4 displays an illustration of the effects of Pure
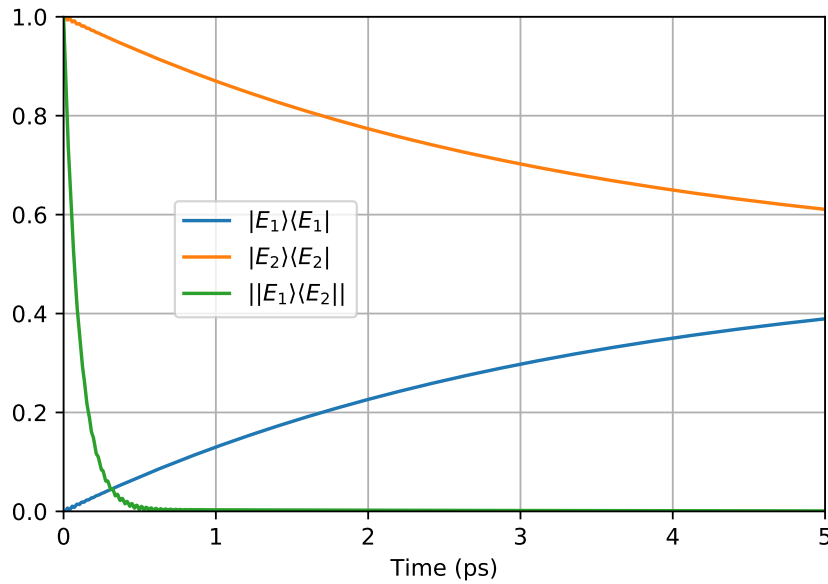
Figure 2.4: Demonstration of the action of Pure Dephasing on the exciton populations and inter-exciton coherence of a TLS. Γ_{deph}=[0.1 ps]$^{-1}$. Initial state: $|E_1\rangle\langle E_1| = 0$, $|E_2\rangle\langle E_2| = 1$, $|E_1\rangle\langle E_2| = 1$, $|E_2\rangle\langle E_1| = 0$.

Dephasing on the populations and coherences of an isolated excitonic system. As expected an equal mixing of the two states is formed when initialised in the upper excitonic state $|E_2\rangle$.

The choice of dephasing rate is of vital importance to accurately simulate a bio-inspired dimer as it determines the coherence lifetime of the electronic degrees of freedom. Studies of algal protein PC645 at cryogenic temperatures provides experimental evidence of electronic coherence on the timescale of 500 fs [65]. Other studies of PE545 have detected quantum beating on the order of hundreds of femtoseconds [14, 74]. It is reasonable therefore to choose a decay rate of Γ_{deph} =[0.1 ps]$^{-1}$.

2.3.3 Thermal Relaxation

It is often desirable to model the effect of an environment at a specific temperature with which the system can equilibrate. In the Exciton-Vibration Dimer we couple each intramolecular modes to a separate thermal reservoirs at 298 K. This is represented by transition operators b_1 and b_2 at rate $\Gamma_{th}(1+B)$ and $b_1^\dagger$ and $b_2^\dagger$ at rate $\Gamma_{th}B$. Here $B = \left(e^{\frac{\omega}{k_BT}} - 1 \right)^{-1}$ is the mean number of quanta in a thermally occupied mode of frequency ω, and $\Gamma_{th} = [1 \text{ ps}]^{-1}$ is the rate at which modes equilibrate [6].
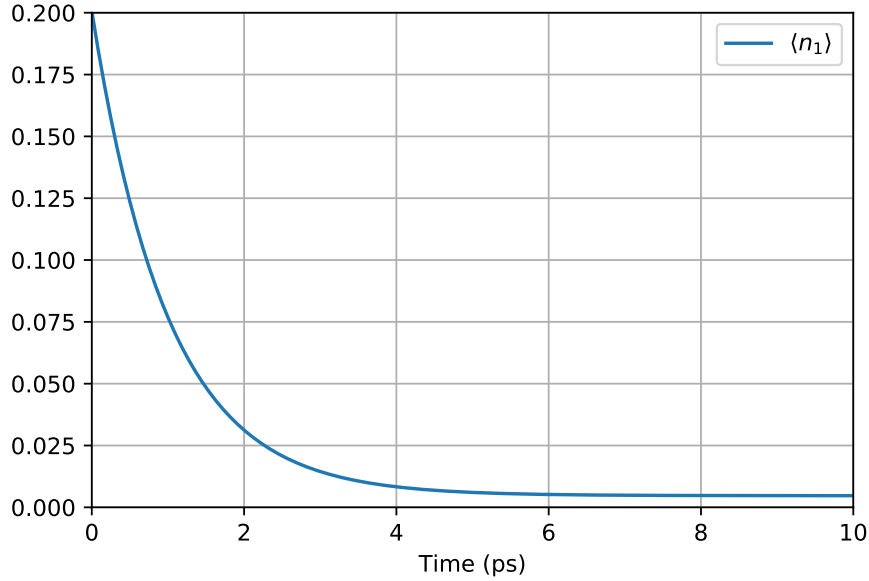
Figure 2.5: Demonstration of the thermal relaxation of a mode of frequency 1111 cm^{-1} with a bath at temperature 298 K at rate $\Gamma_{th} = [1 \text{ ps}]^{-1}$. Initial state is a thermal distribution at 900 K.

The lifetime of vibrational coherence in chromophores has been measured to be on the order of picoseconds [82]. Here we follow other recent works [58] in choosing an equilibration rate of $\Gamma_{th} = [1 \text{ ps}]^{-1}$. Figure 2.5 displays the average occupation number $\langle n \rangle = Tr\left\{ b^\dagger b \rho_{vib}(t) \right\}$ of one of the system modes as a function of time, in the absence of coupling to the electronic system and presence of thermal relaxation. The occupation exponentially relaxes from an initial thermal state at 900 K to equilibrium with the bath at 298 K. We note that for the modes of frequency $\omega = 1111$ cm^{-1} in PE545 parameters, the ambient temperature 298 K = 207.1 cm^{-1} corresponds to a low occupation number.

2.3.4 Relaxation to steady state

The total Markovian environment contributions in the Exciton-Vibration Dimer model are pure dephasing at equal rates Γ_{deph} on the electronic sites and thermal relaxation on the modes at equal rates Γ_{th}. These environment-induced processes are pictured schematically as coloured ovals in Figure 2.1. Their combined effect is to decohere the coherent evolution of the system (see Figure 2.3) and evolve it towards a new quasi-equilibrium steady state. Here quasi-equilibrium refers to the fact that we are focusing only on the ultra-fast ET process and have not included spontaneous emission which occurs on the nanosecond timescale. It is argued that the rates of decoherence and dissipation in the natural parameter regime of light-harvesting complexes place ET in the optimal regime where coherent contributions to the dynamics do not vanish fully [58].
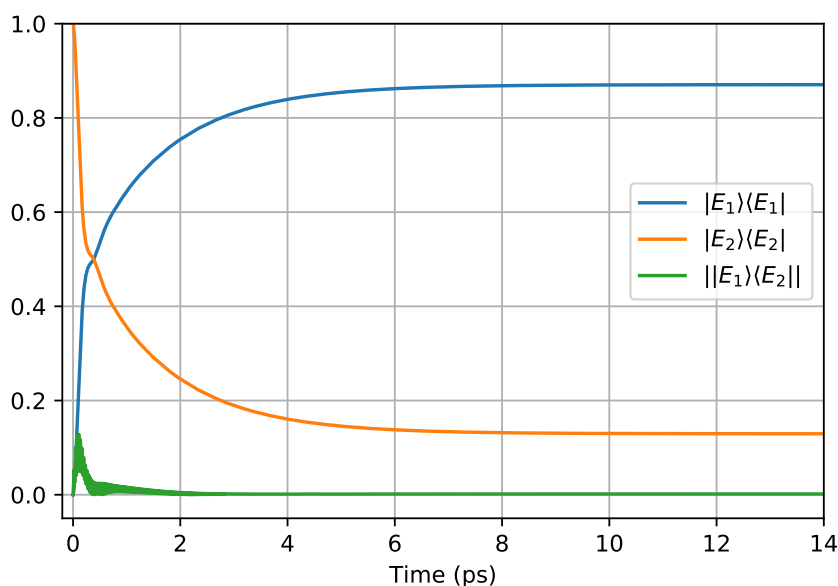
Figure 2.6: Open system evolution of exciton populations and absolute value of inter-exciton coherence. Initial state Equation 2.18 and PE545 parameters listed in Table 2.1.

Figure 2.6 and Figure 2.7 display the open system evolution of exciton populations and mode occupation numbers from initial state Equation 2.18. We can see numerical evidence that the initial dynamics $(0-0.5\ \text{ps})$ are dominated by coherent transitions. This is evidenced both by the sharp transfer of population to
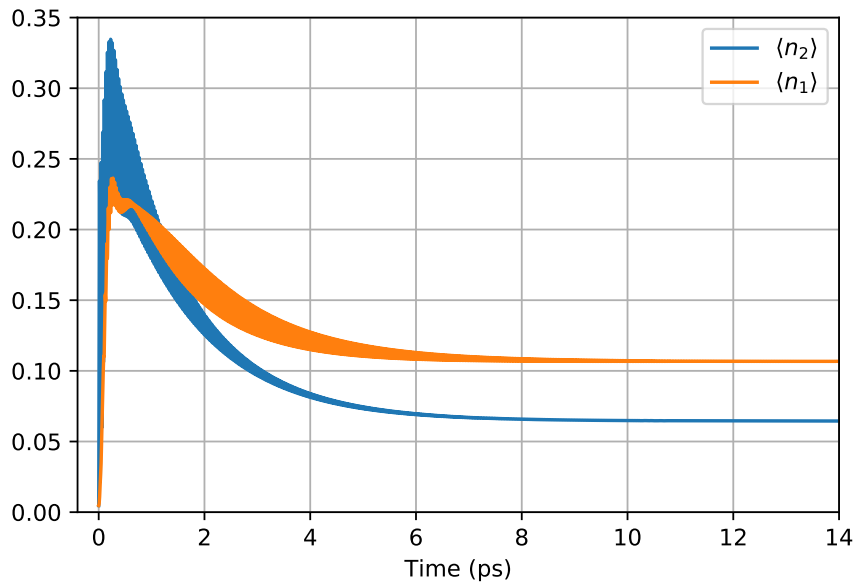
Figure 2.7: Open system evolution of mode average occupation numbers. Initial state Equation 2.18 and PE545 parameters listed in Table 2.1.

lower exciton $|E_1\rangle$ and growth of inter-exciton coherence in Figure 2.6 and by the sharp growth in occupation number of both modes in Figure 2.7. The dynamics during the next picosecond have contributions from both incoherent and coherent processes. From approximately 1.5 ps the dynamics are dominated by incoherent processes, characterised by exponential growth and decay, until steady state of all populations is reached at around 10 ps.

Examining the dynamics of mode occupation numbers of Figure 2.7 more closely we see that both initiate from thermal equilibrium with the bath, gain energy from the electronic system and then relax to a new equilibrium of the combined system. It is in this complex interplay between coherent and incoherent processes during relaxation to the steady state that presents a unique setting within which we will investigate synchronisation in Chapter 3.

2.3.5 Solving Numerically efficiently by vectorising

Equation 2.23 can be expressed in a linearised form to optimise the numerical calculation time. In this case we define a superoperator known as the Liouvillian which captures all the operations acting on our system density matrix but flattened into a

vector $|\rho(t)\rangle\rangle$.

$$|\dot{\rho}(t)\rangle\rangle = \mathscr{L}|\rho(t)\rangle\rangle \tag{2.25}$$

where $\mathscr{L}$ is the Liouvillian superoperator and $|\rho(t)\rangle\rangle$ are flattened density matrices. To find this form of the dissipator we make use of an identity of the Kronecker product. An equation of matrices $ABC = D$ can be expressed as $|D\rangle\rangle = \left(A \otimes C^T\right)|B\rangle\rangle$ where $|B\rangle\rangle$ is a vector constructed in row order from matrix B. This allows us to express:

$$[H,\rho] = H\rho\mathbb{1} - \mathbb{1}\rho H \implies \left(H \otimes \mathbb{1}^T - \mathbb{1} \otimes H^T\right)|\rho\rangle\rangle \tag{2.26}$$

and for a general dissipator:

$$
\begin{aligned}
D[\rho] =& \Gamma\left(O\rho O^\dagger - \frac{1}{2}\rho O^\dagger O - \frac{1}{2}O^\dagger O\rho\right) \\
\implies& \Gamma\left(O \otimes (O^\dagger)^T - \frac{1}{2}\mathbb{1} \otimes (O^\dagger O)^T - \frac{1}{2}O^\dagger O \otimes (\mathbb{1})^T\right)|\rho\rangle\rangle \\
\implies& \Gamma\left(O \otimes O^* - \frac{1}{2}\mathbb{1} \otimes O^T O^* - \frac{1}{2}O^\dagger O \otimes \mathbb{1}\right)|\rho\rangle\rangle
\end{aligned} \tag{2.27}
$$

We solve this ordinary differential equation in Python 3 with packages NumPy and SciPy and author generated scripts.

Chapter 3

Quantum Synchronisation and Coherence

In this chapter we study the synchronisation of molecular motions in a bio-inspired vibronic dimer where the dynamics of electronic excitation is mediated by coherent interactions with intramolecular vibrational modes. We show that the synchronisation dynamics of the displacement of these local modes exhibit a rich behaviour which arises directly from the distinct time-evolutions of different vibronic quantum coherences. Furthermore, our study shows that coherent energy transport in this bio-inspired system is concomitant with the emergence of positive synchronisation between mode displacements. This work provides further understanding of the relations between quantum coherence and synchronisation in open quantum systems and suggests an interesting role for coherence in biomolecules, that is promoting the synchronisation of vibrational motions driven out of thermal equilibrium. Content from this chapter has been published in a journal paper by the author [75].

3.1 Introduction

The mechanisms of how synchronisation phenomena manifest in the quantum regime are yet to be completely determined. Recent works have shown that investigating the dynamics of synchronisation in open quantum systems can give insight into this issue. As mentioned in Section 1.1 the emerging picture is that the specific forms of the decoherence channels and of the interactions among quantum subsystems play a pivotal role in reaching synchronisation. However, exactly how the interplay between coherent dynamics and decoherence enables synchronisation in a particular time scale, or how coherences may relate to synchronisation is not fully understood.

The results of this chapter form an understanding of synchronisation from the point of view of exciton-vibration eigenstates and decoherence processes that is both referred to and built upon throughout the entire thesis. It is the central contribution this thesis makes.

This chapter is organised as follows: In Section 3.2 we introduce and characterise the measure of synchronisation we use. In Section 3.3 we introduce our exciton-vibration coherences description of synchronisation by considering the purely coherent dynamics of the dimer. In Section 3.4 we show that when dissipative processes are included, spontaneous synchronisation of the displacements of intramolecular modes in exciton-vibration dimers emerges and it is accompanied by a negatively synchronised transient. We illustrate how this synchronisation can be understood as the dominance of a specific exciton-vibration coherence over a set of competing coherences that contribute to oscillatory dynamics in the position of the modes. Finally we provide a qualitative explanation for the dominance of one coherence over others. In Section 3.6 we discuss and summarise.

3.2 Quantifying Synchronisation

As discussed in Chapter 1, the form of synchronisation we study here is transient, spontaneous and between two oscillators only. We are interested in unravelling the influence of coherence and decoherence on the emergence of synchronisation. In order to do this effectively we require a quantitative measure that can both tell us whether synchronisation has occurred and give us information about the early-time dynamics before synchronisation is reached. A review of multiple different measures [24] suggests that the Pearson correlation factor is a good choice for this scenario. It is widely used in the quantum synchronisation literature, gives clear indication of synchronisation and shows some information about the timescales involved. However, in the form it is presented in [24] it does not give much information about the early-time transient dynamics before synchronisation is reached, only indication of when it has occurred. Here we present a modification to the measure that allows it to be used as a continuous measure of phase difference and therefore reveal information about the early times and the emergence of synchronisation.

Defined generally for any two time dependent functions $f_1(t)$ and $f_2(t)$:

$$C_{f_1,f_2}(t|\Delta t) = \frac{\int_t^{t+\Delta t} \delta f_1 \delta f_2 dt}{\left(\int_t^{t+\Delta t} \delta f_1^2 dt \int_t^{t+\Delta t} \delta f_2^2 dt\right)^{1/2}} \tag{3.1}$$

where $\delta f = f - \bar{f}$, $\bar{f} = \frac{1}{\Delta t}\int_t^{t+\Delta t} f(t') dt'$ is a time average and Δt is the averaging window. In ref [24] the Pearson correlation factor is said to return a value of 1 for positive synchronisation (in-phase), -1 for negative synchronisation (π out of phase) and 0 for asynchrony. Here we note that by an careful choice of Δt to be as close as possible to time period T of the dominant frequency in f_1 then $C_{f_1,f_2}(t|\Delta t = T)$ in fact is a continuous measure of phase difference between the two oscillating signals. This function returns a continuous value in the range of -1 to 1 corresponding to a phase shift between f_1 and f_2 of π to 0. We derive this relation analytically for two example sinusoids in the following. Choosing $f_1 = \sin \omega t$ and $f_2 = \sin(\omega t + \phi)$ such that the two oscillations have identical frequencies and amplitudes lie within the same range. With the choice of $\Delta t = \frac{2\pi}{\omega}$ it is straightfor-

ward to show that both $\bar{f}_1$ and $\bar{f}_2$ are zero:

$$\bar{f}_1 = \frac{\omega}{2\pi} \int_{t'}^{t' + \frac{2\pi}{\omega}} \sin \omega t \, dt = \frac{\omega}{2\pi} \left[\frac{-\cos \omega t}{\omega} \right]_{t'}^{t' + \frac{2\pi}{\omega}} = 0 \qquad (3.2)$$

$$\bar{f}_2 = \frac{\omega}{2\pi} \int_{t'}^{t' + \frac{2\pi}{\omega}} \sin(\omega t + \phi) \, dt = \frac{\omega}{2\pi} \left[\frac{-\cos(\omega t + \phi)}{\omega} \right]_{t'}^{t' + \frac{2\pi}{\omega}} = 0 \qquad (3.3)$$

In general the functions f_1 and f_2 may be more complex and have different amplitudes or be displaced from zero. In these cases the values $\bar{f}_1$ and $\bar{f}_2$ are not zero, the function $\delta f_1 = f_1 - \bar{f}_1$ acts to subract the average value of f_1 and center any oscillations around zero. This has the effect of emphasising the fluctuations around the mean and allows more accurate measurement of phase. The integral of their product is the main measure of synchronisation:

$$\int_{t'}^{t' + \frac{2\pi}{\omega}} \delta f_1 \delta f_2 \, dt = \int_{t'}^{t' + \frac{2\pi}{\omega}} \sin(\omega t) \sin(\omega t + \phi) \, dt$$

$$= \left[\frac{1}{2} t \cos \phi - \frac{\sin(2\omega t + \phi)}{4\omega} \right]_{t'}^{t' + \frac{2\pi}{\omega}} \qquad (3.4)$$

$$= \frac{\pi \cos \phi}{\omega}$$

This shows that for a sliding window of one time period $T = \frac{2\pi}{\omega}$ and two perfect sinusoids, the time dependence disappears. For any value of t, the measure returns a constant value that depends only on the phase difference between the signals ϕ. Finally, the role of the denominator in Equation 3.1 is to normalise the measure to the limits of 1 and -1. It is straightforward to show that for our example oscillations: $\left(\int_t^{t + \Delta t} \delta f_1^2 \, dt \int_t^{t + \Delta t} \delta f_2^2 \, dt \right)^{1/2} = \frac{\pi}{\omega}$. Together, this finally results in:

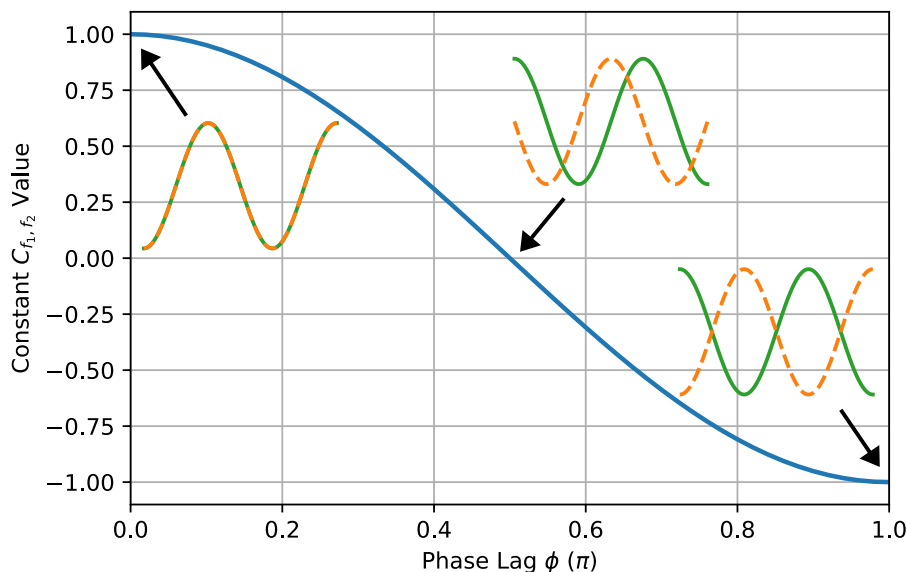$$C_{f_1, f_2} (\Delta t = T) = \cos \phi \qquad (3.5)$$

Figure 3.1: Value of synchronisation measure C_{f_1,f_2} for two identical sinusoids as a function of their phase shift ϕ. $f_1 = \sin(at)$, $f_2 = \sin(at + \phi)$, $\Delta t = 1/a$.

A characterisation of this relationship is presented in Figure 3.1 where the value of the synchronisation function is plotted as a function of constant phase difference ϕ. The synchronisation measure for three different scenarios is illustrated in Figure 3.2. We observe that for two waves of different frequency, $C_{f_1,f_2}(t|\Delta t = T_1)$ does not stabilise and oscillates as the phase relationship shifts over time. The frequency of oscillation is proportional to the frequency difference between the two oscillators.

These effects can be understood by analysing the form of Equation 3.4. For any two functions, Equation 3.4 has a maximum when they are identical, and therefore has a maximum value of 1. For any phase shift or frequency shift the integral of their product will be less than the square root of the product of their integrals.

At the time of writing this measure had not been explicitly applied as a dynamic phase measure between two signals elsewhere in the literature. It has only been used as an indicator of positive (value of $+1$, zero phase difference) or negative (value of -1, π phase difference) synchronisation. The only modification we made was to specify a choice of Δt. We emphasise that this choice is critical to the performance of this function as a dynamic phase measure.
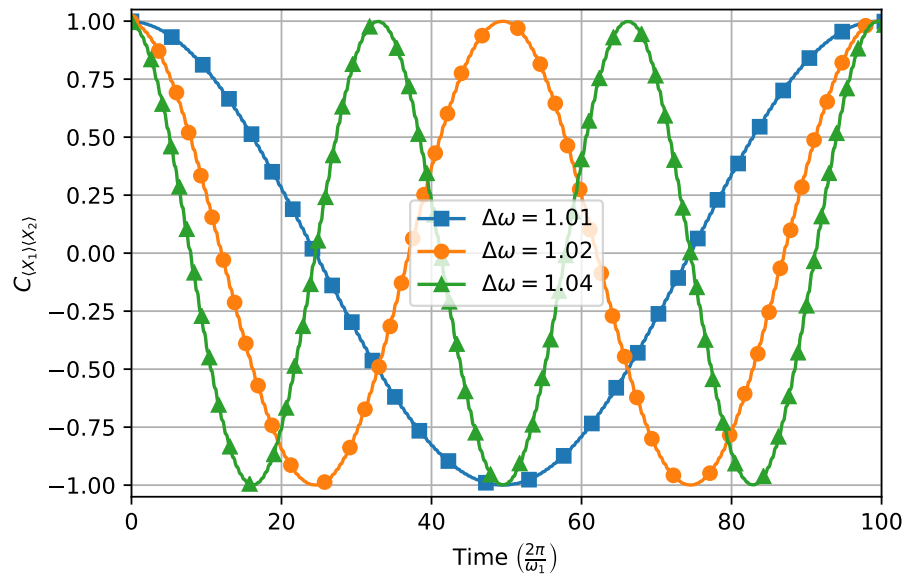
Figure 3.2: Value of synchronisation measure C_{f_1, f_2} for three sets of two uncoupled sinusoids of different frequencies $\Delta \omega = \omega_2 / \omega_1$.

Other attempts to develop a real-time phase measure between two oscillating signals have been conducted along the lines of sliding-window discrete Fourier transform methods [56], Hilbert transforms with data extension [71] and other correlation functions [70].

This measure is used repeatedly throughout the thesis as a dynamic measure of phase and allows us to connect synchronisation to system dynamics in novel ways.

3.3 Coherent Evolution

In order to understand the dynamical emergence of synchronisation between the positions of intramolecular modes we begin by exploring the time dependence of the expected values of the position operators, $\langle X_{i=1,2}(t)\rangle$.

In its eigenstate basis the density matrix of the exciton-vibration system reads $\rho(t) = \sum_{j,k}\rho_{jk}(t)|\psi_j\rangle\langle\psi_k|$ with $\rho_{jk}(t) = \langle\psi_j|\rho(t)|\psi_k\rangle$. The expectation value $\langle X_i(t)\rangle$ is then:

$$
\begin{aligned}
\langle X_i(t)\rangle &= \mathrm{Tr}\{X_i\rho(t)\} \\
&= \sum_l \langle\psi_l|\left(X_i\sum_{j,k}\rho_{jk}(t)|\psi_j\rangle\langle\psi_k|\right)|\psi_l\rangle \\
&= \sum_{j,k}\rho_{jk}(t)\langle\psi_k|X_i|\psi_j\rangle \\
&= \sum_{j,k}\rho_{jk}(t)X_{i,kj}
\end{aligned}
\tag{3.6}
$$

where $X_{i,kj} = \langle\psi_k|X_i|\psi_j\rangle$. Equation 3.6 indicates that the time-evolution of local positions are given by the matrix elements $\rho_{jk}(t)$, yet the ability to exhibit synchronised behaviour depends critically on the form of $X_{i,kj}$ as it is the only source of difference between $\langle X_1(t)\rangle$ and $\langle X_2(t)\rangle$.

To explore the consequences of Equation 3.6 in more detail we analyse whether synchronisation can occur in the closed quantum system whose dynamics is solely given by the system Hamiltonian H. Let us denote $\rho^H(t)$ as the density matrix of the closed system, which evolves according to:

$$
\rho^H(t) = \sum_{j,k}\rho_{jk}(0)e^{i\Omega_{kj}t}|\psi_j\rangle\langle\psi_k|
\tag{3.7}
$$

Here $\rho_{jk}(0) = \langle\psi_j|\rho(0)|\psi_k\rangle$ are the populations ($j=k$) and coherences ($j\neq k$) of the initial state while $\Omega_{kj} = \varepsilon_k - \varepsilon_j$ where ε_j are the eigenenergies of H. One can therefore see that in a closed quantum dynamics only coherences will contribute oscillatory components, with specific frequencies Ω_{kj}, to the dynamics of $\langle X_i(t)\rangle$.

To exhibit synchronisation we require oscillations in $\langle X_1(t)\rangle$ to align in fre-

quency and phase with $\langle X_2(t) \rangle$ for an extended period of time. Using Equations 3.6 and 3.7 this requires the equality:

$$\sum_{j,k} \rho_{jk}(0)e^{i\Omega_{jk}t}X_{1,kj} = \sum_{j,k} \rho_{jk}(0)e^{i\Omega_{jk}t}X_{2,kj} \tag{3.8}$$

for the oscillating components $j \neq k$. Equation 3.8 is trivially true if the initial state is an eigenstate of H. However this cannot be considered synchronised as there will be no time evolution at all. Hence Equation 3.8 can only be satisfied (and be non-zero) if the initial state $\rho(0)$ is such that element $\rho_{jk}(0)$ is zero when elements $X_{1,kj} \neq X_{2,kj}$. The only $\rho(0)$ that can fulfil these criteria contains either a single (or a specific combination of) eigenstate coherence(s), $|\psi_j\rangle\langle\psi_k|$.

	$|\psi_0\rangle\langle\psi_2|$	$|\psi_0\rangle\langle\psi_3|$	$|\psi_1\rangle\langle\psi_4|$	$|\psi_1\rangle\langle\psi_5|$	$|\psi_3\rangle\langle\psi_7|$	$|\psi_3\rangle\langle\psi_8|$	$|\psi_1\rangle\langle\psi_3|$
Ω_{kj} (cm^{-1})	1111.0	1125.0	1102.6	1111.0	1111.0	1119.2	81.0
$\langle\psi_k|X_1|\psi_j\rangle$	0.707	-0.637	0.767	0.707	0.707	-0.935	-0.174
$\langle\psi_k|X_2|\psi_j\rangle$	0.707	0.637	-0.767	0.707	0.707	0.935	0.174

Table 3.1: Seven largest amplitude exciton-vibration coherences. Top row is the associated oscillation frequency from Equation 3.6. The remaining rows are the matrix elements corresponding to coherence $|\psi_j\rangle\langle\psi_k|$ of different operators which represent the coupling to position of mode 1 and coupling to position of mode 2.

For the system under consideration, we identify the seven largest position matrix elements $X_{i,kj}$ contributing to the position dynamics and present their associated exciton-vibration coherences $|\psi_j\rangle\langle\psi_k|$ and frequencies, Ω_{kj}, in Table 3.1. Examining these values shows that in the parameter regime considered (specifically $\omega_1 = \omega_2$, see Section 3.6 for more details) the position matrix elements fall into two distinct groups: those for which $X_{1,kj} = X_{2,kj}$ and those for which $X_{1,kj} = -X_{2,kj}$. For the latter set, the amplitude scaling of -1 results in a phase factor of π between $\langle X_1(t) \rangle$ and $\langle X_2(t) \rangle$.

Consider an example $\rho(0) = \alpha|A\rangle\langle A| + (1-\alpha)|B\rangle\langle B|$. If $|A\rangle = |\psi_1\rangle + |\psi_5\rangle$ and $|B\rangle = |\psi_3\rangle + |\psi_7\rangle$, then the only coherences would be $|\psi_1\rangle\langle\psi_5|$ and $|\psi_3\rangle\langle\psi_7|$ and the resulting dynamics would consist of oscillations of frequency 1111.0 cm^{-1} with no phase separation between $\langle X_1(t) \rangle$ and $\langle X_2(t) \rangle$. Similarly, if $|A\rangle = |\psi_1\rangle + |\psi_4\rangle$ and

$|B\rangle = |\psi_3\rangle + |\psi_8\rangle$) then the only coherences would be $|\psi_1\rangle\langle\psi_4|$ and $|\psi_3\rangle\langle\psi_8|$, resulting in oscillations at a frequency between 1102.6 cm^{-1} and 1109.2 cm^{-1} except with a constant phase separation of π. Both of these scenarios can be identified as synchronised as there is a constant phase difference over time: in the former the displacements are positively synchronised and in the latter they are negatively synchronised. A combination of the two groups of coherences however would create interferences yielding a cyclic phase change between $\langle X_i(t)\rangle$.

Whilst it is possible to find an initial state in which the dynamics of $\langle X_i(t)\rangle$ evolve in a synchronised way, this cannot be classed as spontaneous synchronisation as it has not emerged from an initially non-synchronised state. In the closed system evolution, the ratio of these coherences is determined only by the initial state $\rho(0)$ thereby fixing the frequency composition and precluding that there can be no dynamical emergence of synchronisation. The fact that synchronisation cannot emerge in the closed quantum system concurs with previous studies of coupled TLSs which show that synchronisation cannot occur in the presence of dephasing alone and some energy loss is required [27]. This analysis allows us to postulate a mechanism for synchronisation in the open system which is as follows: in the presence of dissipation we would expect one (or a set) of coherences to emerge with a significantly larger amplitude than the others allowing it to dominate the dynamics of $\langle X_i(t)\rangle$ and produce a constant phase difference in $\langle X_i(t)\rangle$.

Figure 3.3 displays the numerical results of evolution of $\langle X_i(t)\rangle$ and the correlation measure $C_{\langle X_1\rangle\langle X_2\rangle}(t)$ in the closed system with initial state $\rho(0)$ (Equation 2.18). As expected, we see a large range of frequency oscillations in $\langle X_i(t)\rangle$. The value of $C_{\langle X_1\rangle\langle X_2\rangle}(t)$ changes in a cyclic pattern, indicating a continuous change in phase between the between the oscillations and a clear difference in frequency compositions.

The frequency components in each $\langle X_i(t)\rangle$ can be resolved by taking the real part of the Fourier Transform (FT) which we present in Figure 3.4. We note here how the frequencies present are exactly those in Table 3.1 and that the frequencies that correspond to negative synchronisation can be clearly seen as those which have
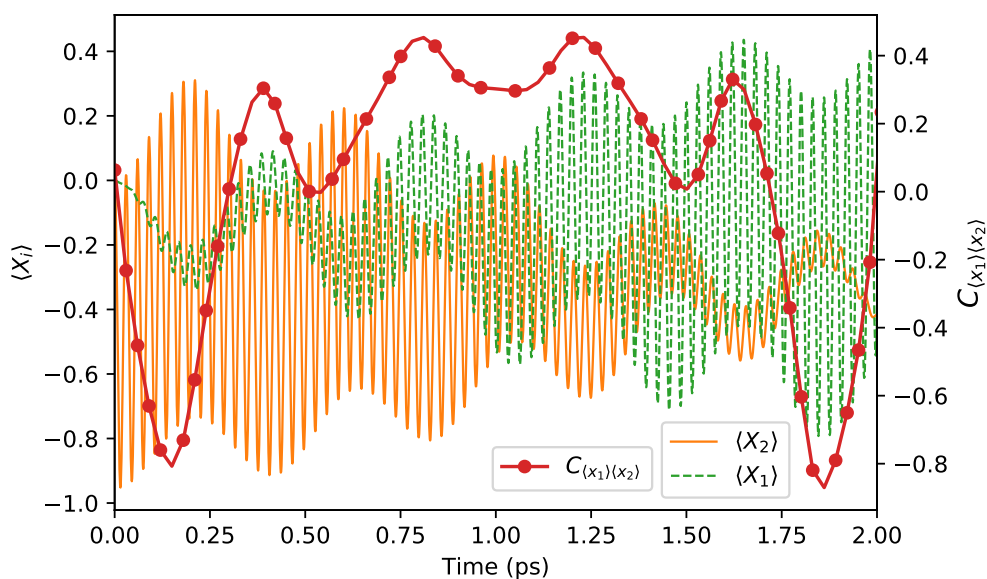
Figure 3.3: Coherent evolution of expectation value of intramolecular mode positions $\langle X_i(t) \rangle$ and their synchronisation $C_{\langle X_1 \rangle, \langle X_2 \rangle}(t)$.
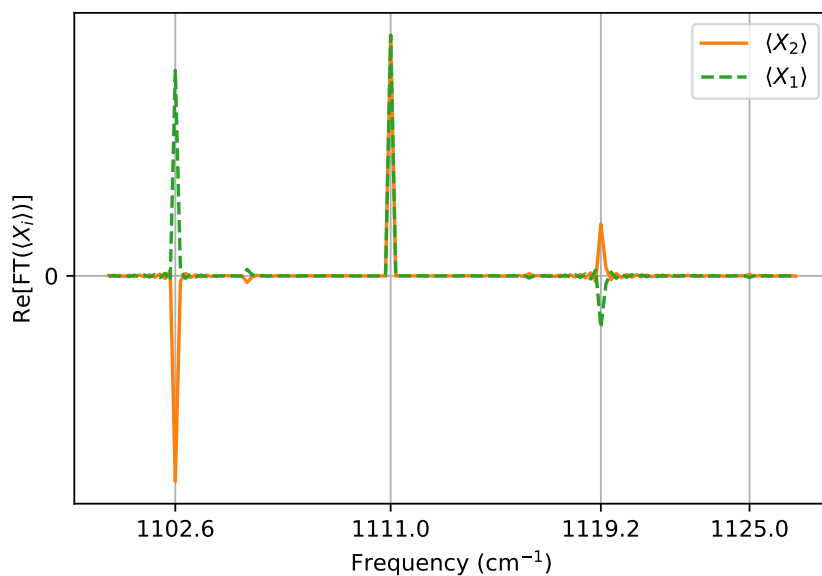
Figure 3.4: Real part of Fourier Transform of full time $\langle X_i(t) \rangle$ under coherent evolution.

opposite sign in the FT.

Figure 3.5 displays the short-time dynamics of the real parts of the five exciton-vibration coherences that dominate the evolution of $\langle X_i(t) \rangle$ (see Equation 3.6), weighted by their associated position matrix elements. Interference between these

Figure 3.5: Coherent evolution of Real part of exciton-vibration coherences scaled by their coupling to $\langle X_1(t) \rangle$ (top half) and $\langle X_2(t) \rangle$ (bottom half).

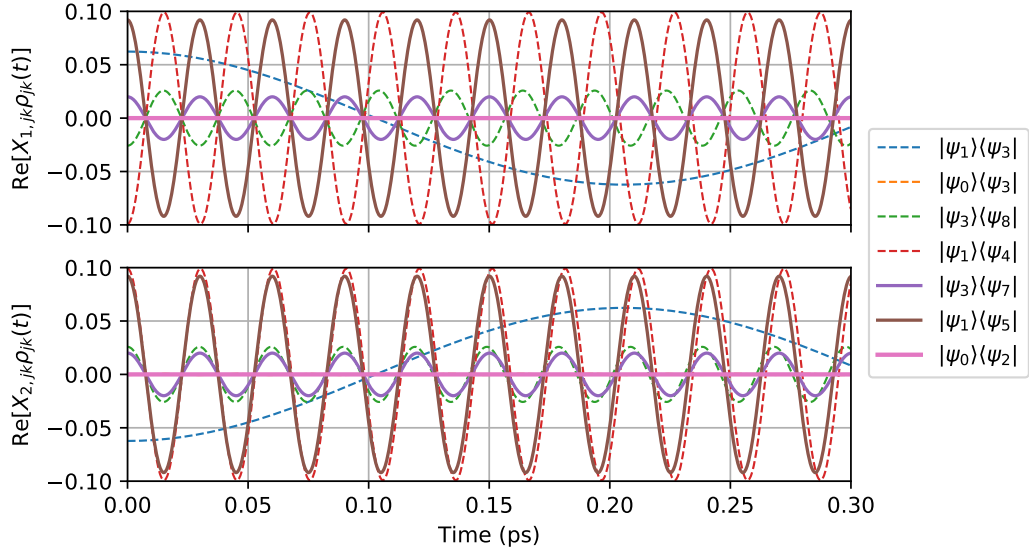coherences generate the overall $\langle X_i(t) \rangle$ signals. Coherences $|\psi_1\rangle\langle\psi_5|$ and $|\psi_3\rangle\langle\psi_7|$ (bold lines) have identical frequencies and remain in phase throughout, whereas coherences $|\psi_1\rangle\langle\psi_4|$ and $|\psi_3\rangle\langle\psi_7|$ (dotted lines) begin to accumulate a phase difference due to their differing frequencies. The phase shift over time manifests as an oscillation in $\langle X_i(t) \rangle$ at a frequency equal to the differences between the pairs of Ω_{kj} involved. These are 8 cm^{-1} (time period of 4.2 ps) and 17 cm^{-1} (time period of 1.9 ps) which explains the approximate 2 ps periodicity seen in Figure 3.3. The oscillation of period 0.4 ps is due to interference with low frequency coherence $|\psi_1\rangle\langle\psi_3|$ (dotted line slowly changing). It is clear that no single coherence dominates the dynamics and that synchronisation does not emerge from the chosen initial state in the closed system evolution.

3.4 Open System Dynamics and the Emergence of Synchronisation

To understand how a synchronised state can emerge from a non-synchronised state we must understand the form of $\rho_{jk}(t)$ in the open quantum system. Solving Equation 2.23 for an element jk results in a set of coupled differential equations (see Appendix A for detailed derivation):

$$\dot{\rho}_{jk}(t) = i\Omega_{jk}\rho_{jk}(t) + \sum_{\alpha,\alpha'} R_{j,k,\alpha,\alpha'}\rho_{\alpha,\alpha'}(t) \tag{3.9}$$

where $R_{j,k,\alpha,\alpha'}$ is commonly known as the Redfield tensor which captures the dependence of each $\rho_{j,k}$ on all other matrix elements as induced by the local dissipators. In this case we cannot say that the time dependence of each coherence $|\psi_j\rangle\langle\psi_k|(t)$ consists of only one single oscillation frequency Ω_{jk}. However, our numerical results show that the oscillatory dynamics of each of the seven coherences in Table 3.1 are in fact dominated by the coherent component and that the latter terms in Equation 3.9 contribute mainly a decaying dynamics. It is this decay that allows a change in ratio of coherences and the potential for synchronisation to emerge.

Figure 3.6 reports the synchronisation of $\langle X_1(t)\rangle$ and $\langle X_2(t)\rangle$ in the first two picoseconds of evolution. Inspection of the fast oscillations in the positions reveal an almost π phase difference between $\langle X_i(t)\rangle$ at 0.15 ps and exactly in phase oscillations after 1 ps. This observation is captured quantitatively with $C_{\langle X_1\rangle,\langle X_2\rangle}(t)$ dipping to -0.75 towards negative synchronisation at 0.15 ps and then up to 1 for positive synchronisation at 1 ps. These numerical results show that synchronisation indeed occurs between the displacements of intramolecular modes of exciton-vibration dimers during the energy transfer process. To understand the underlying mechanism we perform an analysis similar to the previous section.

Figure 3.7 displays the FT of $\langle X_i(t)\rangle$ at 0.15 ps and 1.50 ps. Synchronisation can be seen again in this figure as the change in frequency distribution between the two time points. At 0.15 ps the FT resembles that of the coherent case in Figure
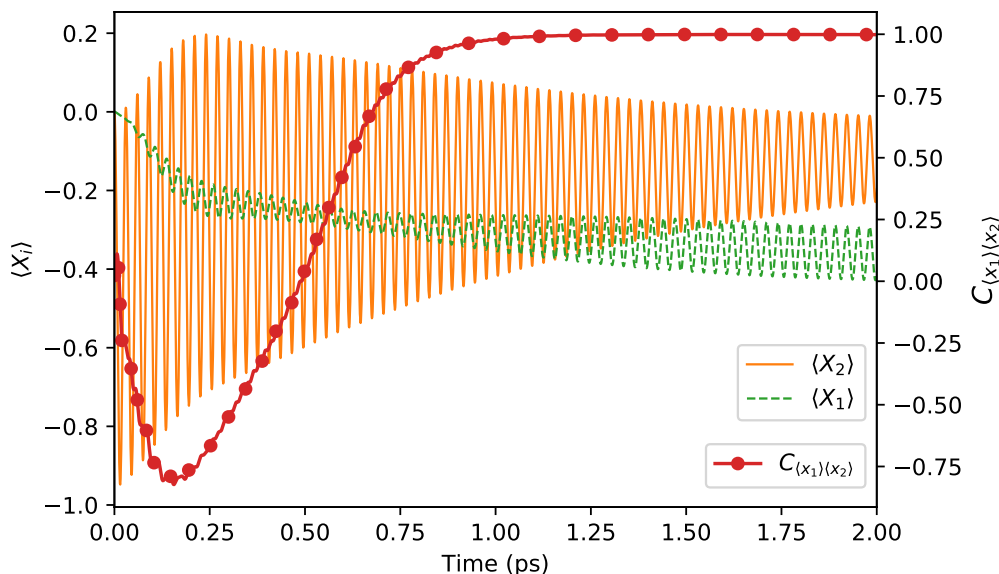
Figure 3.6: Evolution of the expectation value of intramolecular mode positions $\langle X_i(t)\rangle$ and their synchronisation $C_{\langle X_1\rangle,\langle X_2\rangle}(t)$. Initial state is Equation 2.18 and relevant parameters are listed in Table 2.1.

3.4 which indicates at this time coherent dynamics are dominating. The presence of negatively synchronised frequency $1102.6\ \mathrm{cm}^{-1}$ at a magnitude comparable to positively synchronised frequency $1111.0\ \mathrm{cm}^{-1}$ results in an interference and a non-stationary phase. This is reflected in $C_{\langle X_1\rangle,\langle X_2\rangle}(t)$ in Figure 3.6 at early times $(0 - 1\ \mathrm{ps})$ where the measure is continuously changing. At 1.5 ps we see the dominant frequency become $1111.0\ \mathrm{cm}^{-1}$ which has equal amplitude in both $\langle X_i(t)\rangle$ and corresponds to the value of 1 in $C_{\langle X_1\rangle,\langle X_2\rangle}(t)$.

Although it is useful for understanding the dynamics of synchronisation, this FT picture does not allow us to understand why the frequency composition of $\langle X_i(t)\rangle$ changes over time. To do so we must consider the underlying exciton-vibration coherence dynamics which we present in Figure 3.8. Initially we observe that the dominant frequency in the oscillation of each coherence is indeed the coherent part Ω_{jk} as can be evidenced by comparison to Figure 3.5. Figure 3.8a presents the first 0.30 ps of evolution of coherences where the two signals are measured as being towards negatively synchronised. Figure 3.8b presents the same coherences at 1.35 ps where they are measured as positively synchronised. We can immediately see
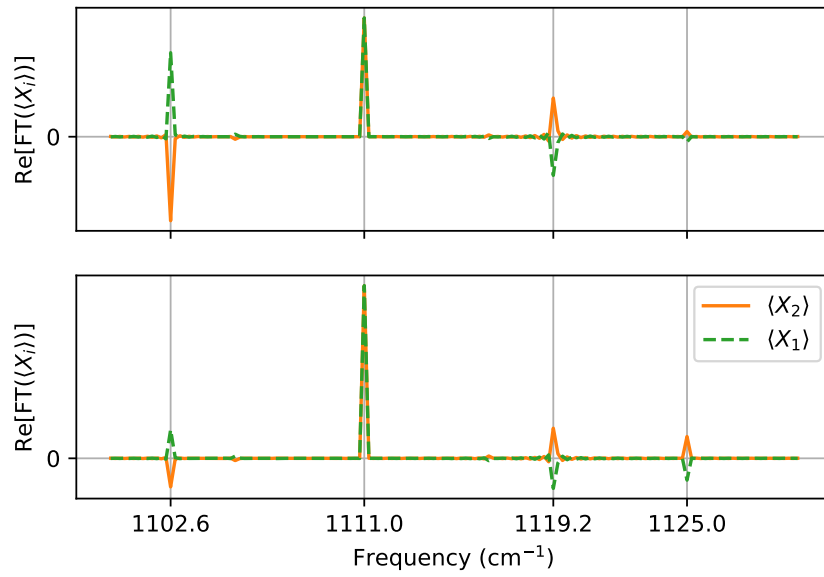
Figure 3.7: Real part of Fourier Transform of $\langle X_i \rangle$ at 0.15 ps (top half) and 1.50 ps (bottom half) during open system evolution.

how a change in the amplitude of the coherences has occurred in the latter case and the two signals appear much more similar. The dominant contributions come from the three positively synchronised coherences $|\psi_0\rangle\langle\psi_2|$, $|\psi_1\rangle\langle\psi_5|$ and $|\psi_3\rangle\langle\psi_7|$ (solid lines). These coherences constructively interfere to dominate the oscillations seen in $\langle X_i(t) \rangle$ and therefore a value of 1 in $C_{\langle X_1 \rangle, \langle X_2 \rangle}(t)$. It is this change in the ratio of coherences over time that determines the emergence of synchronisation.

In previous studies [27] the mechanism for synchronisation has been related to a difference in the decay rates of eigenmodes of the Liouvillian superoperator, $\mathscr{L}$. The reasoning is that synchronisation occurs when one eigenmode of $\mathscr{L}$, that is equally coupled to the operators of interest such that their evolutions are synchronised, significantly outlives the other eigenmodes, transiently dominates the dynamics, and holds the operators in a synchronised state. Recently this explanation has been consolidated analytically with an exact treatment of a single dissipating qubit coupled to a probe qubit [26]. In the original case these normal modes are found by diagonalising $\mathscr{L}$ and finding the conjugate pair of eigenvectors that have eigenvalues with real parts closest to zero and which couple significantly to the desired operator. Applying this process here results in an eigenmode of the Liouvillian that
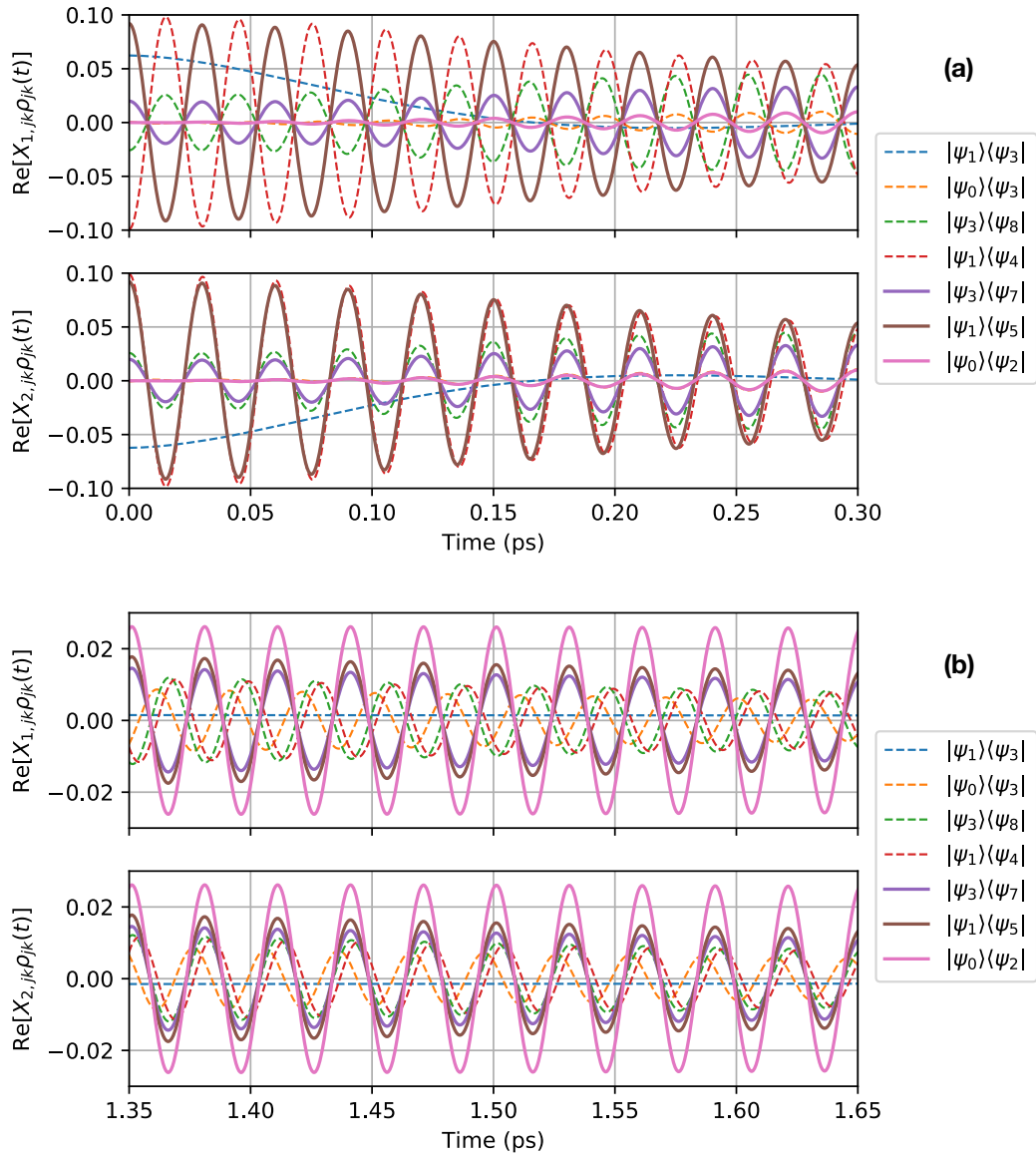
Figure 3.8: Evolution of Real part of exciton-vibration coherences in the open system scaled by their coupling to $\langle X_1(t) \rangle$ (top halves) and $\langle X_2(t) \rangle$ (bottom halves) at times (a) $0 - 0.30$ ps (b) $1.35 - 1.65$ ps.

consists almost entirely of exciton-vibration coherence $|\psi_0\rangle\langle\psi_2|$. This analysis corroborates with our results which we present by plotting the absolute value of each coherence in Figure 3.9. We find coherence $|\psi_0\rangle\langle\psi_2|$ is indeed longest lived.
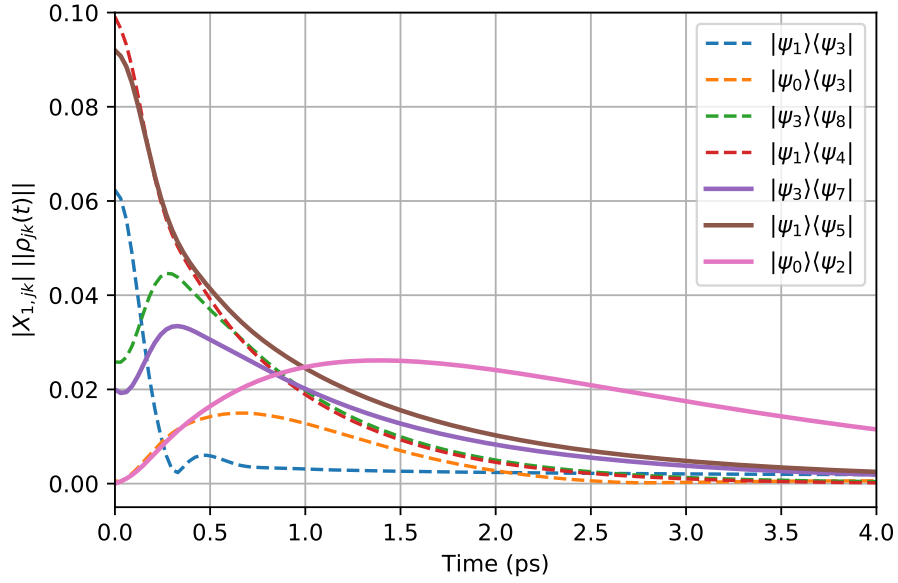
Figure 3.9: Complex magnitude of exciton-vibration coherences scaled by the absolute value of their corresponding position matrix element in the open quantum system evolution. $|X_{1,jk}| = |X_{2,jk}|$.

The Liouvillian eigenmode analysis provides a straightforward prediction of the emergence of synchronisation at long times, but it does not facilitate an understanding of the early transient synchronisation dynamics. Neither does it provide understanding of why certain eigenmodes survive longer than others. The tracking of coherences we present in this paper however is capable of giving us insight into these early transients. In addition it allows us to give a qualitative explanation of why certain coherences survive longer in the presence of dissipation and dephasing.

	$|\psi_0\rangle\langle\psi_2|$	$|\psi_0\rangle\langle\psi_3|$	$|\psi_1\rangle\langle\psi_4|$	$|\psi_1\rangle\langle\psi_5|$	$|\psi_3\rangle\langle\psi_7|$	$|\psi_3\rangle\langle\psi_8|$	$|\psi_1\rangle\langle\psi_3|$
$\langle\psi_k|\sigma_x|\psi_j\rangle$	0.000	0.385	0.340	0.000	0.000	0.384	0.196
$\langle\psi_k|G_{12}|\psi_j\rangle$	0.161	-0.144	-0.131	0.133	0.032	0.026	-0.351

Table 3.2: Seven largest amplitude exciton-vibration coherences and the values of operator matrix elements. First row: coupling to inter-exciton coherence. Second row: coupling to ground state of both modes where $G_{12} = |0_1\rangle\langle0_1| \otimes |0_2\rangle\langle0_2|$.

We expect pure dephasing to result in exponential decays in excitonic coherences and thermal dissipation to cause exponential decays in the population of modes [6]. In Table 3.2 we consider the matrix elements of an operator relating to excitonic coherences only $\sigma_x = |E_1\rangle\langle E_2| + |E_2\rangle\langle E_1|$, and the combined vibrational ground-state projector operator $G_{12} = |0_1\rangle\langle 0_1| \otimes |0_2\rangle\langle 0_2|$. Exciton-vibration coherences that result in a large matrix element for σ_x will be more affected by the fast electronic dephasing. Similarly coherences that result in largest values for the projector of the ground vibrational states would last the longest due to thermal dissipation operating on a longer timescale and preferentially populating such ground states.

Out of the set of coherences considered the one that has the lowest exciton coherence component and the largest ground-state vibrational component is $|\psi_0\rangle\langle\psi_2|$. Referring again to Figure 3.9 we find indeed that $|\psi_0\rangle\langle\psi_2|$ is the longest lived coherence. In fact Figure 3.9 reveals that the timescale at which $|\psi_0\rangle\langle\psi_2|$ becomes the dominant coherence is the same timescale at which the synchronisation measure reports positive synchronisation. This figure gives a clear perspective on the competition between positively and negatively synchronised coherences mentioned above. At early times the total magnitude of negatively synchronised coherences outweighs that of the positively synchronised coherences. During the open system evolution, the negatively synchronised coherences decay and positively synchronised coherence is generated. Between $0.5 - 1$ ps the total magnitude of positive synchronised coherences overtakes the negative and the phase shifts to positive synchronisation.
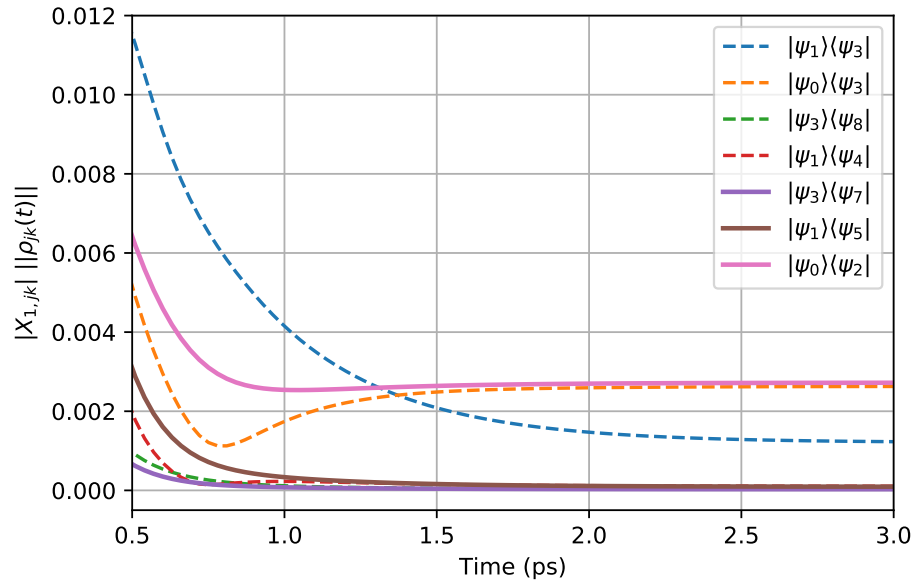
Figure 3.10: Complex magnitude of exciton-vibration coherences scaled by the absolute value of their corresponding position matrix element for modified dephasing $\Gamma_{el} = [0.2\text{ ps}]^{-1}$ and dissipation $\Gamma_{th} = [0.1\text{ ps}]^{-1}$ rates.
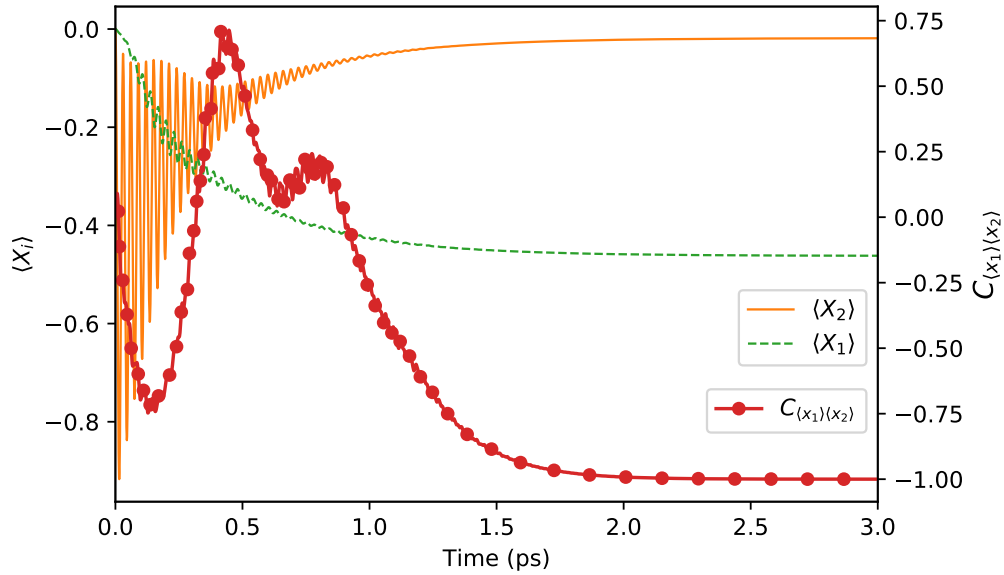
Figure 3.11: Expectation value of mode positions and their synchronisation measure $C_{\langle X_1 \rangle, \langle X_2 \rangle}$ for modified dephasing $\Gamma_{el} = [0.2\text{ ps}]^{-1}$ and dissipation $\Gamma_{th} = [0.1\text{ ps}]^{-1}$ rates.

Finally, we present further evidence for this mechanism of synchronisation with a numerical test. We set the thermal dissipation rate to $\Gamma_{th} = [0.1\text{ ps}]^{-1}$ and

the dephasing rate to $\Gamma_{el} = [0.2 \text{ ps}]^{-1}$ and repeat the analysis of before. In this case we would expect eigenstate coherences containing a larger excitonic coherence component to survive longer as the electronic dephasing is slower relative to the thermal dissipation. Indeed we find that the coherences $|\psi_0\rangle\langle\psi_3|$ and $|\psi_1\rangle\langle\psi_3|$ are much longer lived in this regime and compete with $|\psi_0\rangle\langle\psi_2|$. The results of this investigation are summarised in Figures 3.10 and 3.11. Figure 3.10 shows that the contribution to mode position oscillations from negatively synchronised coherences outweighs that of positively synchronised coherences in the long time regime. This manifests in the negative synchronisation of Figure 3.11 when $C_{\langle X_1\rangle,\langle X_2\rangle}(t)$ falls to -1 after 2 ps. We also note that due to the increased thermal dissipation rate, the mode position oscillations are much smaller. This effect can be observed even in tiny oscillations.

In summary we have shown how the interplay between exciton-vibration dynamics and the different noise sources considered lead to a rich synchronisation dynamics for the local modes and shown how said dynamics maps directly to the evolution of exciton-vibration coherences.

3.5 The Role of Coherent Energy Transfer in Synchronisation

Thus far we have described the coherent and dissipative contributions to the dynamics of exciton-vibration coherences and therefore to the dynamics of synchronisation. Presently we turn our attention to the electronic energy transfer dynamics of the light-harvesting unit considered, its coherent character and its relation to synchronisation of local displacements.

We can intuitively understand how ET is essential for the synchronisation of local displacements in the prototype dimers studied by recalling both the quasi-localised nature of the excitons for the parameter regime considered and the local nature of the electronic-vibration interactions. Trivially, ET between excitons must occur for the intramolecular modes to become effectively coupled, exchange energy and synchronise. However the precise relations between the degree of coherent electronic ET and synchronisation is less obvious. In our synchronisation analysis so far we observe that the ET period (0 - 0.5 ps) is concomitant with the negatively synchronised transient of Figure 3.6. It appears that during this energy transfer period the displacements of the modes tend towards being negatively synchronised. This suggests a signature of coherent ET could be found in a measure of synchronisation of local mode displacements, which we discuss further in Section 3.6.

To investigate the relationship between coherent ET and synchronisation quantitatively, we compare scenarios in which the resonance condition between exciton energy splitting and mode energy quanta is kept fixed but the degree of delocalisation of excitons is increased such that coherent ET transfer is enhanced. We also analyse the case in which the frequency of the modes are detuned from the exciton energy splitting to illustrate the fundamental role of the energy matching condition both for ET and for synchronisation.

The energy difference between exciton splitting and vibrational energies, i.e. $\Delta = \Delta E - \omega$; the coupling strength between local vibrational and electronic degrees of freedom g; and the exciton size or delocalisation θ which depends on the ratio $\eta = 2|V|/\Delta E$ all influence the coherent character of ET. An approximate indicator

of the degree of coherent ET is derived from the transition probability between the two exciton-vibration states dominating electronic ET in our prototype dimer [57]. The indicator is an estimate of the maximum amplitude A for the population oscillations and is given by:

$$A = \frac{1}{1 + \left(\frac{\Delta}{2g\sin(2\theta)}\right)^2} \tag{3.10}$$

The base parameter regime used throughout this work (see Section 2.1.4) corresponds to $A = 0.76$. For the off-resonant modes we choose a frequency of 1500 cm^{-1} (a mode at this frequency is also present in PE545 [81]), resulting in $A = 0.04$. For increased exciton delocalisation we choose $\eta = 0.5$ but keep the energy resonance condition Δ fixed, resulting in $A = 0.95$.
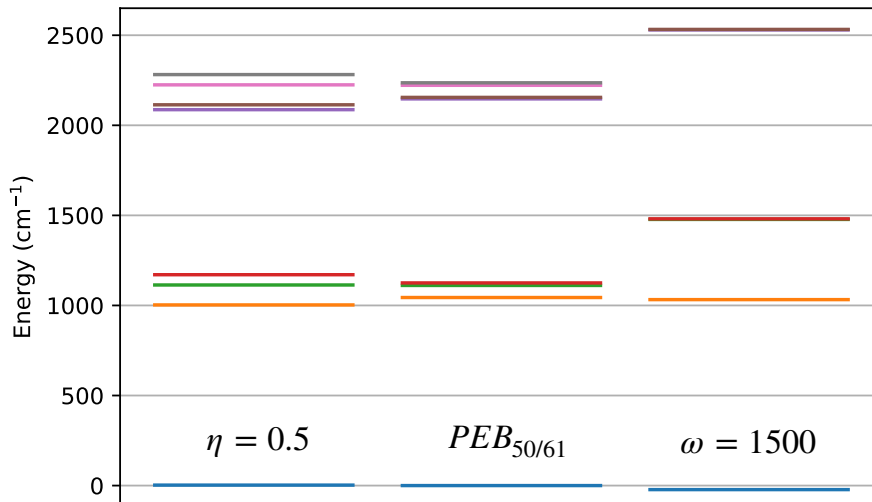
Figure 3.12: Changes in eigenenergies for three different transport regimes characterised by the measure A. From left to right: modified exciton localisation $\eta = 0.5$ with $A = 0.95$, unmodified PE545 parameters corresponding to Table 2.1 with $A = 0.76$ and modified mode frequencies $\omega = 1500 \text{ cm}^{-1}$ with $A = 0.04$.

The changes to the system in these three parameter regimes is usefully represented by the change in eigenenergies which we present in Figure 3.12. We can see that in the detuned regime $\omega = 1500 \text{ cm}^{-1}$ the eigenenergies are much further separated and therefore coherent transitions between eigenstates are less probable. In

the more delocalised regime $\eta = 0.5$ the resonance is preserved but the quasi-local compositions of eigenstates is significantly different. In general the eigenstates have larger contributions from both of the exciton states therefore transitions between them transfer more exciton population and ET is enhanced. We choose to show numerical evidence of the changes in ET in Figure 3.13 by presenting the lowest exciton population dynamics (operator $|E_1\rangle\langle E_1|$) alongside the dynamics of synchronisation and the selected exciton-vibration coherences (as in Figure 3.9 from the previous analysis) for each regime. Together these plots allow us to compare the three different ET regimes and consider their effects on synchronisation.

Firstly we note the clear change in magnitude of coherent ET from high in Figure 3.13a, to low in Figure 3.13c and that the time taken for synchronisation to occur appears to follow the same pattern. Positive synchronisation is achieved in 0.5 ps when $A = 0.95$, 1 ps when $A = 0.76$ and is not reached in the 2 ps window presented when $A = 0.04$. This correlation is also reflected in the exciton-vibration coherence evolutions in Figures 3.13(d–f) (note we have removed two of the seven exciton-vibration coherences for clarity). When $A = 0.95$ (Figure 3.13d) negatively synchronised coherences (plotted with shape markers) decay faster than when $A = 0.76$ (Figure 3.13e). This results in the positively synchronised coherences (solid lines) dominating from an earlier time and hence the earlier emergence of positive synchronisation. When $A = 0.04$ (Figure 3.13f) we observe that positively and negatively synchronised coherences have almost identical amplitude throughout the evolution and therefore neither can dominate. Small differences are amplified and interferences prevent synchronisation in the time scale considered. Positive synchronisation only emerges at around 10 ps (not shown) when positive synchronised coherences finally outlive the negative synchronised ones however by this time the oscillation amplitudes have nearly decayed to zero.

Additionally we identify that the eigenstate coherence $|\psi_1\rangle\langle\psi_3|$ can be used as an indicator of the magnitude of coherent ET. In the three regimes considered its amplitude appears correlated with the amplitude of coherent ET. This can be understood by considering the composition of the eigenstates involved and their
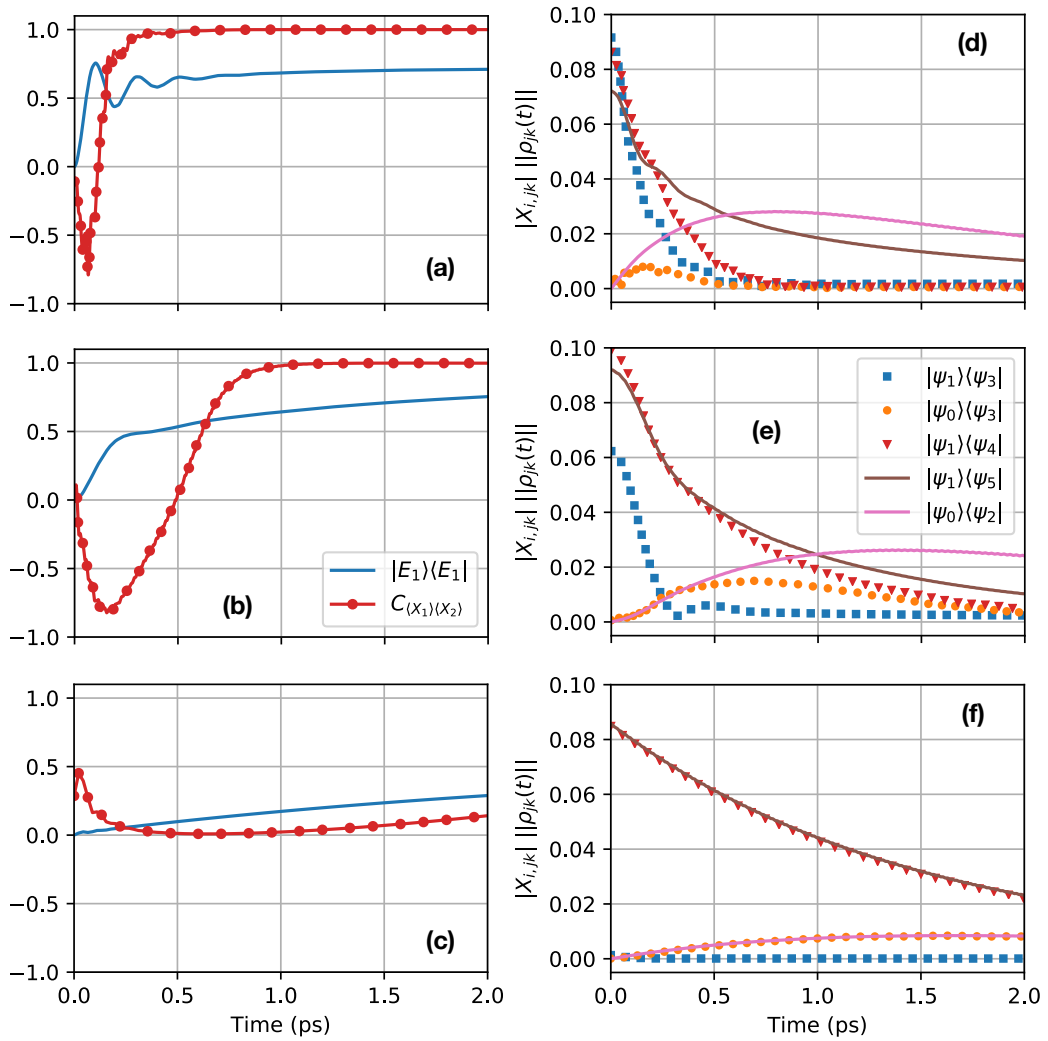
Figure 3.13: Comparison of dynamics of ET with synchronisation of $\langle X_i(t) \rangle$ and the magnitude of exciton-vibration coherences for three different parameter regimes: (b)(e) for central PEB dimer in PE545 (parameters in Table 2.1) corresponding to A=0.76; (a)(d) modified parameters $\eta = 0.5$ corresponding to A=0.95; (c)(f) modified parameters $\omega = 1500 \text{ cm}^{-1}$ corresponding to A=0.04.

energy splitting. Firstly, the eigenstates $|\psi_1\rangle$ and $|\psi_3\rangle$ have an energy splitting of only $81 \text{ cm}^{-1} \ll \omega$ which leads to resonance energy transfer between them. Secondly, in the quasi-local basis $\{|E_d, n_1, n_2\rangle\}$, these eigenstates have the following

approximate compositions:

$$|\psi_1\rangle \approx 0.3|E_1\rangle(|01\rangle - |10\rangle) + 0.9|E_200\rangle - 0.2|E_201\rangle$$
$$|\psi_3\rangle \approx 0.6|E_1\rangle(|01\rangle - |10\rangle) - 0.4|E_200\rangle + 0.1|E_201\rangle$$

(3.11)

which shows that a transition between them would transfer exciton population. Together this suggests the coherence $|\psi_1\rangle\langle\psi_3|$ is part of the ET mechanism and explains why its amplitude scales in accordance with the changes in ET.

Our analyses clearly highlight a correlation between the amplitude of coherent excitation transport and the time it takes for mode displacements to synchronise. This is significant as it suggests that a degree of control of quantum synchronisation can be achieved by adjusting only coherent exciton-vibration interactions and specifically without changing the environment-induced dissipation or dephasing.

The relationship we observe can be understood as follows: parameter changes that increase ET effectively increase the coupling between the subsystems and allow a faster exchange of energy; the electronic subsystem 'overshoots' its equilibrium position and ET oscillations occur; the damping of pure exciton coherences accelerates and in turn the decay of negatively synchronised exciton-vibration coherences accelerates; the system becomes dominated by positive synchronised coherences in a shorter time scale and exhibits the shorter synchronisation times we observe.

Spectroscopic analysis of pigment-protein complexes have revealed possible signatures of synchronised vibrational motion. In a fluorescence depolarisation study of Light-Harvesting Complex 1 from Rhodobacter Sphaeroides, in phase oscillations were observed between parallel and perpendicular signals [5]. This behaviour was later reproduced in a theoretical model suggesting that the origin of the in-phase oscillations were synchronised vibrational motions [13]. The theoretical analysis of the synchronisation dynamics presented in this chapter corroborates these early signatures of synchronisation in photosynthetic pigment-protein complexes.

3.6 Summary and Discussion

The results of Sections 3.4 and 3.5, indicate negative synchronisation is concomitant with coherent energy transport. Moreover, our analysis of the exciton-vibration coherences that are negatively synchronised showed that they all have a large component of excitonic coherence. This raises the question: can we conclude that the negative synchronisation of local mode displacements is a signature of the survival of excitonic coherence? A transient shift towards negative synchronisation persists in all different initial preparations of exciton state (except for an initial state equal to the the steady state), and the shift becomes less pronounced as coherent exciton population transport inhibited. Additionally, as reported in Section 3.4, if dephasing rates are slower than thermal relaxation i.e. excitonic coherence is longer lived, we find that the length of this negative synchronisation period extends to the steady state. Altogether this suggests that, for the system considered, a negatively synchronised transient in the positions of intramolecular modes can indeed be a signature of excitonic coherence and coherent energy transfer.

The parameter regime studied throughout this chapter is for the special case of $\omega_1 = \omega_2$. This restriction allowed us to focus on the complex relationship between synchronisation, coherence and dissipation. However, it also raises some interesting points.

Firstly, a classical view of two coupled oscillators with $\omega_1 = \omega_2$ might lead one to expect synchronisation to trivially always occur. We have shown that in the quantum setting, due to the exciton-vibration nature of the complex, the frequencies at which the local mode positions may oscillate are not equal and, in fact, change over time. This effect cannot be thought of classically. On the other hand, the relationship between ET and synchronisation can be thought of as analogous to how increasing the coupling strength between two classical oscillators allows them to synchronise faster. Our intramolecular modes are coupled to local electronic states that exchange energy through electronic coupling. Increasing ET involves increasing the electronic coupling which leads to a stronger effective coupling between the modes.

Secondly, as mentioned in Section 3.4, the exciton-vibration coherences we study have precisely equal or opposite values in $X_{i,kj}$. We can explain this result by examining our Hamiltonian for differences between X_1 and X_2. Whilst $\omega_1 = \omega_2$, swapping X_i would result in no changes to H_{vib} and a sign change on excitonic coherences in $H_{exc-vib}$ i.e. $\langle E_2 | \Theta_1 | E_1 \rangle = -\langle E_2 | \Theta_2 | E_1 \rangle$. This -1 scaling is the source of the differences between $X_{1,kj}$ and $X_{2,kj}$ seen in this investigation. If $\omega_1 \neq \omega_2$, H_{vib} is no longer symmetric upon exchange of X_i. We expect this detuning would result in a wide range of $X_{i,kj}$ and therefore contributions of different phases to the dynamics. We explore this further in the next chapter.

To summarise we have predicted the transient spontaneous synchronisation of the displacements of intramolecular modes on neighbouring molecules in a bio-inspired vibronic dimer. Until now, synchronisation had not been investigated in a hybrid quantum system where excitonic and vibrational coherence overlap in such a way. We have presented an understanding of the mechanism for synchronisation as the survival of specific exciton-vibration coherences, and detailed how coherences are selected for by dissipation. This analysis may provide a perspective from which we can understand synchronisation in other dissipating hybrid quantum systems such as larger multi-chromophore systems.

We showed that both dissipative and coherent dynamics play an important role in the formation of synchronisation in these systems. Coherent ET is positively correlated with the time scale in which synchronisation is achieved. Dissipation is required for the decay of exciton-vibration coherences to allow one to dominate and can control the form of synchronisation that occurs. The parameter regime that most closely resembles a real photosynthetic dimer appears to be one where there is a balance between coherent and dissipative dynamics in which synchronisation can emerge before the steady state is reached. Our work highlights a novel possible role for exciton-vibrational coherence in biomolecular complexes, namely supporting the synchronisation of out-of-equilibrium vibrational motions.

Chapter 4

Synchronisation Phase as an Indicator of Quantum Correlations Between Subsystems

In this chapter we explore the dynamics of synchronisation in a bio-inspired exciton vibration dimer as a function of the difference between the natural frequencies of the synchronising molecular motions. We show that there exists a window of frequency difference (detuning) within which synchronisation is achieved with a constant non-zero phase difference between mode oscillations. This 'synchronisation phase' increases as the mode detunings increase, up to a breaking point where synchronisation is no longer achieved. We show that this synchronisation phase is fundamentally different to those predicted elsewhere [48]. We explain how this phase difference arises from the asymmetric participation of modes in long-lived synchronised eigenstates. Lastly we connect the synchronisation phase as a function of detuning to the degree of quantum correlations between the synchronising subsystems. We postulate that this synchronisation phase could be used as an indicator of quantum correlations.

4.1 Introduction

So far in our investigation of synchronisation of molecular motions in bio-inspired vibronic dimers we have considered only the case of identical mode frequencies, i.e. $\omega_1 = \omega_2$. This allowed us to focus our analysis on the effects of coherent and dissipative processes on the dynamics of synchronisation. When the two modes are detuned from one another, more complex phase dynamics become possible, and this is what we explore in this chapter.

In the classical literature, the 'robustness' of synchronisation is often measured by the ability of oscillators to lock in phase despite their natural frequencies being different. Generally there exists a range of detunings for which the resultant frequencies of the oscillators match, and that this resultant frequency lies somewhere between the two undisturbed oscillator frequencies. Naturally, the quantum literature has attempted to recreate this using quantum oscillators. The behaviour is found to be mostly the same [27] with a notable exception: one study of coupled van der Pol oscillators revealed that, contrary to classical expectations, some detuning can enhance synchronisation [43].

The equation of motion for the phase difference between two weakly coupled classical oscillators, to first order, is [61]:

$$\frac{d\Delta\phi(t)}{dt} = -\Delta\nu + \varepsilon f(\Delta\phi(t)) \tag{4.1}$$

where $\Delta\phi(t)$ is the difference between the phases of two oscillators, $\Delta\nu$ is the difference between their natural frequencies, ε is a constant proportional to their coupling strength and $f(\Delta\phi(t))$ is a time-dependent periodic function of $\Delta\phi(t)$. Synchronisation occurs for the stationary solutions of Equation 4.1, all of which fulfil the condition:

$$\Delta\nu < max|\varepsilon f(\Delta\phi(t))| \tag{4.2}$$

Therefore Equation 4.1 predicts synchronisation in the presence of non-equal frequencies to occur at a constant non-zero phase. From here on we refer to this phase difference as the synchronisation phase.

Despite detuning being a well studied parameter for synchronisation and synchronisation phase being predicted classically, the detailed phase dynamics of synchronisation with detuning is not well explored in the quantum regime. One significant review of the literature states that measures need to be improved to account for synchronisation without exactly positive or negative phase but does not formally investigate it [24]. Synchronisation phase is described as 'delayed synchronisation' in Ref. [3] where it is noted to arise from detuning but again is not investigated in depth. Analytic equations similar to the form of Equation 4.1 have been derived in non-linear many-body quantum systems [86] and in exciton-polariton condensates [89]. Synchronisation phase has been shown in linear quantum systems comparable to bio-inspired vibronic dimers [48]. However they derive an analytic expression for the phase which unusually does not have any mode frequency dependence. The question of whether detuning results in synchronisation phase in linear open quantum systems such as the Exciton-Vibration Dimer with Markovian dissipation remains unanswered.

This chapter is organised as follows: in Section 4.2.1 we introduce a modification to the system Hamiltonian to accurately account for detuning; in Section 4.2.2 we present the results of detuning on synchronisation in the bio-inspired vibronic dimer; in Section 4.2.3 we study an alternative model which exhibits a synchronisation phase; in Section 4.2.4 we explain the mechanism for the observed synchronisation phase; in Section 4.3.1 we introduce quantum correlation measures and in Sections 4.3.2 and 4.3.3 we present a connection between synchronisation phase and quantum correlations. Finally in Section 4.4 we summarise the results.

4.2 Synchronisation in the Presence of Detuning

4.2.1 Reorganisation Energy Contributions to the Hamiltonian

In order to accurately account for the effects of different frequency modes on the dynamics of the Exciton-Vibration Dimer, we must include reorganisation energy contributions to the Hamiltonian [47, 64, 76]. In the following we derive these changes.

The Hamiltonian for a two level electronic system, with intersite interaction and where each site is locally coupled to a vibrational mode has the general form [64]:

$$
\begin{aligned}
H = {} & \left(e_1 + \frac{1}{2}\omega_1^2(\hat{x}_1 - d_1)^2 \right) |e_1\rangle\langle e_1| \\
& + \left(e_2 + \frac{1}{2}\omega_2^2(\hat{x}_2 - d_2)^2 \right) |e_2\rangle\langle e_2| \\
& + V\left(|e_2\rangle\langle e_1| + |e_1\rangle\langle e_2| \right) \\
& + \frac{1}{2}\hat{p}_1^2 + \frac{1}{2}\hat{p}_2^2
\end{aligned}
\tag{4.3}
$$

where e_1 and e_2 are the energies of the bare electronic states, $\hat{x}_1$ and $\hat{p}_1$ are the position and momentum operators of mode 1 coupled to site 1, and d_1 is the displacement of the equilibrium position of mode 1 due to electronic state $|e_1\rangle$. This displacement is effectively the site-mode coupling strength. Expanding and rearranging we have:

$$
\begin{aligned}
H = {} & + \left(e_1 + \frac{1}{2}\omega_1^2 d_1^2 \right) |e_1\rangle\langle e_1| + \left(e_2 + \frac{1}{2}\omega_2^2 d_2^2 \right) |e_2\rangle\langle e_2| \\
& + \frac{1}{2}\omega_1^2\hat{x}_1^2 + \frac{1}{2}\hat{p}_1^2 + \frac{1}{2}\omega_2^2\hat{x}_2^2 + \frac{1}{2}\hat{p}_2^2 \\
& - \omega_1^2\hat{x}_1 d_1 |e_1\rangle\langle e_1| - \omega_2^2\hat{x}_2 d_2 |e_2\rangle\langle e_2| \\
& + V\left(|e_2\rangle\langle e_1| + |e_1\rangle\langle e_2| \right)
\end{aligned}
\tag{4.4}
$$

Now we can define the reorganisation energy $\lambda_i = \frac{1}{2}\omega_i^2 d_i^2 = \omega_i S_i$ contribution of the mode to the site energy, where S_i is the Huang-Rhys factor which is experimentally observable through measurements of the Stokes shift [47]. If $\omega_1 = \omega_2$ and $d_1 = d_2$

the site energies are both shifted by the same amount and the reorganisation energy has no affect on dynamics. Here however, we are interested in $\omega_1 \neq \omega_2$ and the reorganisation energy contributions to site energies cannot be discarded. Introducing the position and momentum operators in terms of the creation and annihilation operators: $\hat{x}_i = \frac{1}{\sqrt{2}}\sqrt{\frac{1}{\omega_i}}\left(b_i^\dagger + b_i\right)$ and $\hat{p}_i = \frac{i}{\sqrt{2}}\sqrt{\omega_i}\left(b_i^\dagger - b_i\right)$ and substituting into the previous expression, we obtain:

$$
\begin{aligned}
H =& + (e_1 + \omega_1 S_1)\,|e_1\rangle\langle e_1| + (e_2 + \omega_2 S_2)\,|e_2\rangle\langle e_2| \\
& + \omega_1\left(b_1^\dagger b_1 + \frac{1}{2}\right) + \omega_2\left(b_2^\dagger b_2 + \frac{1}{2}\right) \\
& - \omega_1\sqrt{S_1}\left(b_1^\dagger + b_1\right)|e_1\rangle\langle e_1| - \omega_2\sqrt{S_2}\left(b_2^\dagger + b_2\right)|e_2\rangle\langle e_2| \\
& + V\left(|e_2\rangle\langle e_1| + |e_1\rangle\langle e_2|\right)
\end{aligned}
\tag{4.5}
$$

which we then rotate into a new frequency-dependent exciton basis with matrix $U(\tilde{\theta}(\omega_1,\omega_2))$ where U is a rotation matrix of the form of Equation 2.5 and $\tilde{\theta}(\omega_1,\omega_2) = \frac{1}{2}\arctan\left(\frac{2|V|}{(e_2+\omega_2 S_2)-(e_1+\omega_1 S_1)}\right)$. This results in a Hamiltonian:

$$
\begin{aligned}
H =& + E_1(\omega_1,\omega_2)|E_1\rangle\langle E_1| + E_2(\omega_1,\omega_2)|E_2\rangle\langle E_2| \\
& + \omega_1 b_1^\dagger b_1 + \omega_2 b_2^\dagger b_2 \\
& + \omega_1\sqrt{S_1}\tilde{\Theta}_1 X_1 + \omega_2\sqrt{S_2}\tilde{\Theta}_2 X_2
\end{aligned}
\tag{4.6}
$$

where we have shifted the ground state energies of mode 1 by $\frac{\omega_1}{2}$ and mode 2 by $\frac{\omega_2}{2}$. We define a new $\tilde{\Theta} = U\left(\tilde{\theta}(\omega_1,\omega_2)\right)|e_i\rangle\langle e_i|U^\dagger\left(\tilde{\theta}(\omega_1,\omega_2)\right)$ in the same way as in Section 2.1.1. The exciton eigenenergies are now also mode frequency dependent:

$$
\begin{aligned}
E_1(\omega_1,\omega_2) =& \frac{1}{2}\left((e_1 + \omega_1 S_1) + (e_2 + \omega_2 S_2) - \sqrt{\Delta e^2(\omega_1,\omega_2) + 4V^2}\right) \\
E_2(\omega_1,\omega_2) =& \frac{1}{2}\left((e_1 + \omega_1 S_1) + (e_2 + \omega_2 S_2) + \sqrt{\Delta e^2(\omega_1,\omega_2) + 4V^2}\right)
\end{aligned}
\tag{4.7}
$$

where $\Delta e(\omega_1,\omega_2) = (e_2 + \omega_2 S_2) - (e_1 + \omega_1 S_1)$. We note that for large detunings this new formulation will have a significant effect on the coherent dynamics of the dimer. The detunings considered in the following investigation are small enough

for the effect to be subtle but it must still be included for more physically accurate results.

4.2.2 Detuning in a Bio-Inspired Dimer

We define the detuning $\Delta\omega = \omega_2/\omega_1$ and choose to change the frequency of ω_2 only. This choice allows us to fix the time window of the synchronisation measure $C_{\langle X_1 \rangle, \langle X_2 \rangle}(t|\Delta t)$ as $\Delta t = \frac{2\pi}{\omega_1}$ whilst still probing detuning.

Using the initial state Equation 2.18 and system parameters from Table 2.1 we show in Figure 4.1 the effects on the synchronisation measure $C_{\langle X_1 \rangle, \langle X_2 \rangle}(t)$ for two different regimes of detuning, $\Delta\omega = 1.002$ and $\Delta\omega = 1.02$. These are chosen to illustrate two distinct scenarios in synchronisation dynamics, namely synchronised and not synchronised. These results are best understood by first reminding oneself of the characterisation of the synchronisation function in Section 3.2.

Figure 4.1: Synchronisation measure $C_{\langle X_1 \rangle, \langle X_2 \rangle}(t)$ of expectation value of mode positions for two regimes of detuning: $\Delta\omega = 1.002$ where synchronisation occurs and $\Delta\omega = 1.02$ where it does not.

We find that for $\Delta\omega = 1.02$, the synchronisation measure $C_{\langle X_1 \rangle, \langle X_2 \rangle}(t)$ oscillates, indicating the phase between the two oscillators is continuously changing, in turn showing that the frequencies at which the observables $\langle X_1 \rangle$ and $\langle X_2 \rangle$ oscillate

are different and have not synchronised. If we plot higher detunings (not shown) we find that the frequency of these phase oscillations is correlated with the increased detuning. This is what we would expect from classical dynamics of Equation 4.1. The phase relationship $\Delta\phi(t)$ outside the synchronisation region would change at a rate proportional to their detuning d with periodic fluctuations from $\varepsilon q(\Delta\phi(t))$.

The case of small detuning tells a different story. The straight line for $\Delta\omega = 1.002$ in Figure 4.1 indicates that there is a constant, non-zero phase relationship between $\langle X_1 \rangle$ and $\langle X_2 \rangle$. Their frequencies have synchronised but they are not perfectly aligned in phase. This result also agrees with the predictions of Equation 4.1 within the synchronisation region.

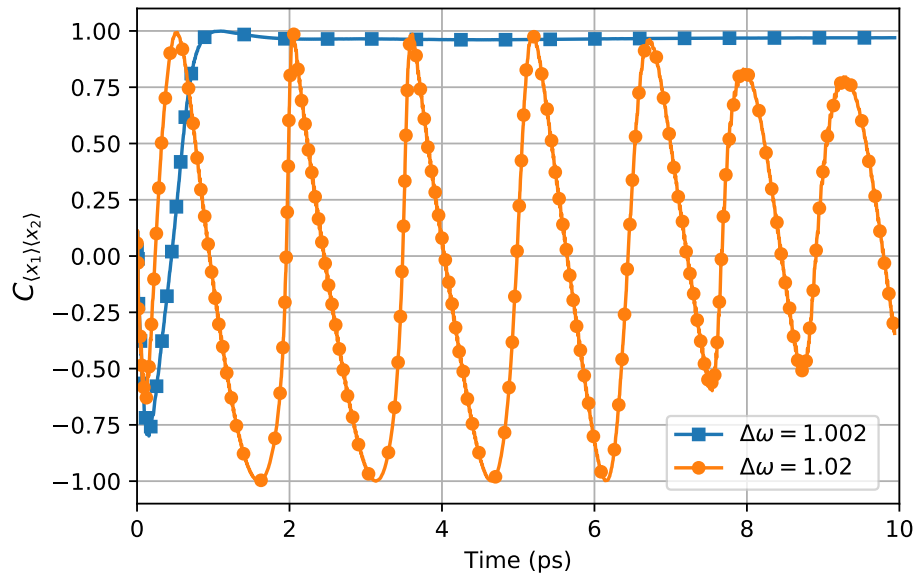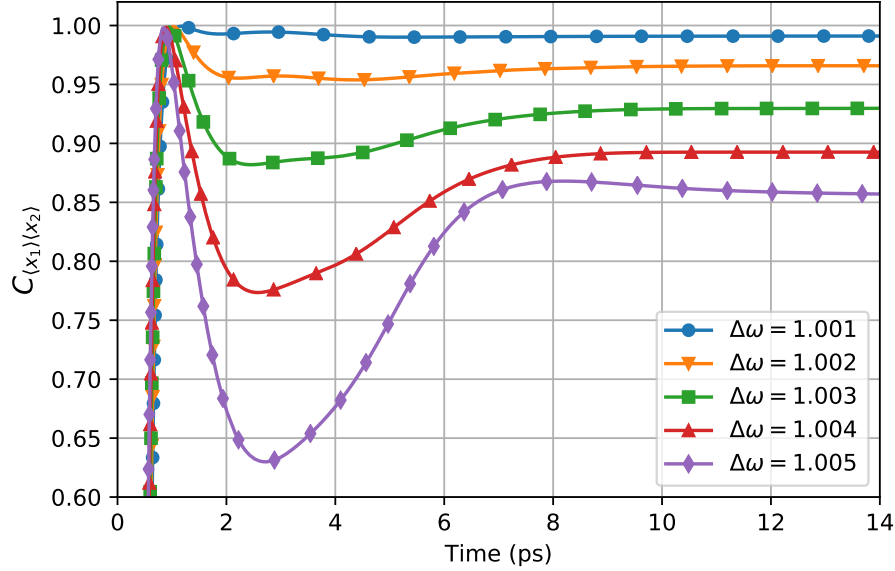**Figure 4.2:** Synchronisation measure $C_{\langle X_1 \rangle, \langle X_2 \rangle}(t)$ of expectation value of mode positions revealing synchronisation phase as a function of detuning. Detuning parameters listed in-figure.

To take a closer look at this relationship we calculate the synchronisation dynamics for a range of detunings. Investigating only the detunings for which a synchronised state is reached i.e. a constant $C_{\langle X_1 \rangle, \langle X_2 \rangle}(t)$ value, we produce the results in Figure 4.2. We see a clear negative relationship between the magnitude of detuning and the stable value of $C_{\langle X_1 \rangle, \langle X_2 \rangle}(t)$ reached i.e. increasing detuning increases the synchronisation phase, up to a breaking point where synchronisation is not reached.

The overall dynamics of $C_{\langle X_1 \rangle, \langle X_2 \rangle}(t)$ for the detunings presented in this section are similar to what would be expected in the classical case. There exists a window of detunings within which synchronisation occurs and the time taken to reach a synchronised state increases with detuning. The quantum mechanism for this observed behaviour is explained fully in Section 4.2.4. In order to do so with clarity, we first explore synchronisation phase as investigated in a different system [48] and analyse its origins.

4.2.3 Militello et al. Case Study

The investigation by Militello et al. [48] demonstrates synchronisation phase in a relaxing quantum system comparable to the Exciton-Vibration Dimer. In the following we aim to clarify that the origin of synchronisation phase they present is distinct from the detuning mechanism presented in the previous section. Furthermore, the similarities between the quantum systems studied may provide insight into the mechanism producing a synchronisation phase in the previous section.

Militello et al.'s model consists of a TLS and two QHOs with a Jaynes-Cummings interaction Hamiltonian which, using the same notation as for the Exciton-Vibration Dimer, has the form:

$$
\begin{aligned}
H = & +e_1|e_1\rangle\langle e_1| + e_2|e_2\rangle\langle e_2| \\
& + \omega_1 b_1^\dagger b_1 + \omega_2 b_2^\dagger b_2 \\
& + g_1 \left(e^{i\phi_1} b_1 + e^{-i\phi_1} b_1^\dagger \right) \sigma_x + g_2 \left(e^{i\phi_2} b_2 + e^{-i\phi_2} b_2^\dagger \right) \sigma_x
\end{aligned}
\tag{4.8}
$$

where $\sigma_x = |e_1\rangle\langle e_2| + |e_2\rangle\langle e_1|$ and $\phi_{1,2}$ are variables in the range $0 \leq \phi \leq \pi$ that control the coupling between the TLS and the QHOs. The electronic subsystem is coupled to a zero-temperature reservoir the effects of which are modelled by the master equation:

$$
\dot{\rho}(t) = -i[H, \rho(t)] + D_{\sigma_-}[\rho(t)]
\tag{4.9}
$$

where D_{σ_-} is a Lindblad-type dissipator of the form described in Section 2.3.1 with transition operator $\sigma_- = |e_1\rangle\langle e_2|$ and rate Γ_{σ_-}. The modes do not experience any direct dissipation.

A key finding of their work is that when synchronisation occurs, the constant phase difference between the two mode oscillations ϕ_S is determined by the parameters ϕ_1 and ϕ_2 from their Hamiltonian:

$$\phi_S = \pi - (\phi_1 - \phi_2) \tag{4.10}$$

This equation is derived by approximating the effects of dissipation on an initial coherent state of the modes. We note how the synchronisation phase they predict has no dependence on detuning. They investigate the synchronisation phase as a function of variables ϕ_1 and ϕ_2 only. Here we show that we can sufficiently predict the synchronisation phases of Equation 4.10 simply by analysing their Hamiltonian, Equation 4.8. Furthermore we can do so without taking into account any detuning or asymmetric coupling i.e. from the case of $\omega_1 = \omega_2$ and $g_1 = g_2$. This demonstrates a clear distinction between Militello et al.'s analysis and the results of the previous section.

Firstly, by fixing $\phi_2 = 0$ we can see that changing ϕ_1 controls the form of coupling between mode and electronic subsystems:

$$
\begin{aligned}
H_I(\phi_1 = 0) &= g\sigma_x (X_2 + X_1) \\
H_I\left(\phi_1 = \frac{1}{4}\pi\right) &= g\sigma_x \left(X_2 - \frac{X_1}{\sqrt{2}} - \frac{P_1}{\sqrt{2}}\right) \\
H_I\left(\phi_1 = \frac{2}{4}\pi\right) &= g\sigma_x (X_2 + P_1) \\
H_I\left(\phi_1 = \frac{3}{4}\pi\right) &= g\sigma_x \left(X_2 + \frac{X_1}{\sqrt{2}} + \frac{P_1}{\sqrt{2}}\right) \\
H_I(\phi_1 = \pi) &= g\sigma_x (X_2 - X_1)
\end{aligned}
\tag{4.11}
$$

where P_1 is the dimensionless momentum operator for mode 1. Evolution in each of these scenarios would result in synchronisation of the mode observables $\langle X_i \rangle$ with a different phase difference ϕ_S. As we know the only source of dissipation in their model is the transition operator $|e_1\rangle\langle e_2|$ on the electronic subsystem, the dynamics of the modes depend critically on which operators enter this interaction. In the case of $\phi_1 = 0$ we can see that the sum of the mode position operators, also known as the

collective 'centre-of-mass' mode $X_+ = X_1 + X_2$ is directly coupled to the electronic subsystem. In this case it is easy to see that the orthogonal 'relative-displacement' mode $X_- = X_1 - X_2$ is completely decoupled from the electronic system and is therefore free from dissipation. When evolving from an initial coherent state that contains some amplitude in both these modes, the centre-of-mass mode would decay rapidly and the relative-displacement mode would remain indefinitely. Survival of only this collective mode would trivially appear as synchronisation with a constant π phase between $\langle X_1 \rangle$ and $\langle X_2 \rangle$. Indeed Equation 4.10 predicts $\phi_S = \pi - (0-0) = \pi$.
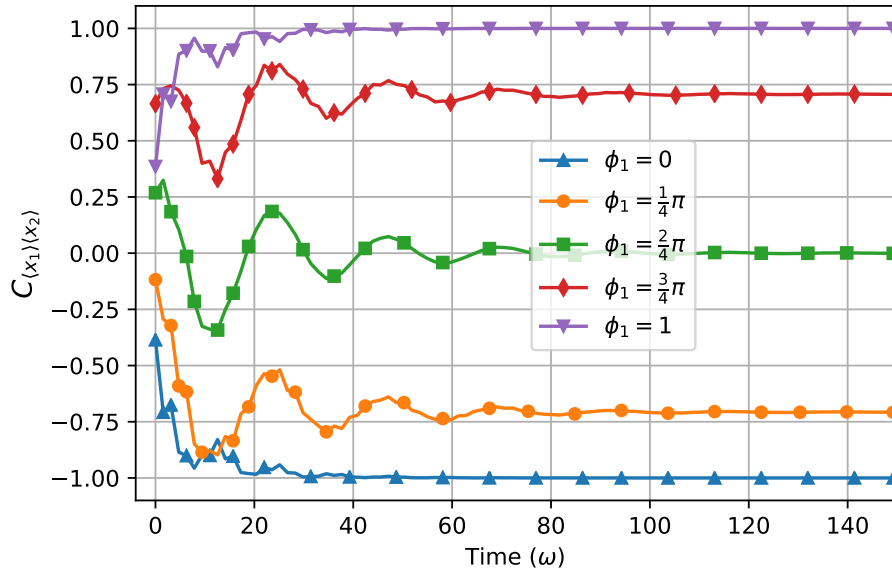

Figure 4.3: Synchronisation measure $C_{\langle X_1 \rangle, \langle X_2 \rangle}(t)$ of expectation value of mode positions for a different values of ϕ_1 as shown in Equation 4.11 for Militello et al.'s model. Initial state: $\rho_0 = |e_1\rangle\langle e_1| \otimes \rho_{vacuum} \otimes \rho_{coherent}$. Parameters $\Delta e = e_2 - e_1$, $\omega = \Delta e$, $g = \Delta e$, $\Gamma_{\sigma_-} = 0.2\Delta e$ [48].

The same logic can be applied to all the in-between phases. In each of the cases there exists some collective mode orthogonal to the one entering the interaction Hamiltonian. E.g. for $\phi_1 = \frac{2}{4}\pi$ the collective mode $P_2 - X_1$ is decoupled from the electronic subsystem and, as position and momentum have a phase difference of $\frac{1}{2}\pi$ this is in agreement with the predictions of Equation 4.10: $\phi_S = \pi - \left(\frac{2}{4}\pi - 0\right) = \frac{1}{2}\pi$. We reproduce their model and use the synchronisation function to measure the phase dynamics of evolution under the five example interaction Hamiltonian phases and

present in Figure 4.3. Using the characterisation of the synchronisation function presented in Figure 3.1 we can see that our calculations predict exactly the phases that Militello et al. predict.

4.2.3.1 Detuning in Militello et al.'s model

We have been able to reproduce the synchronisation phase dynamics demonstrated in Militello et al's study without allowing for any detuning. One question that remains is whether their system can produce the synchronisation phase as a function of detuning that we demonstrated in the Exciton-Vibration Dimer. In order to test this numerically we fix $\phi_2 = 0$ and $\phi_1 = \pi$ and detune the mode frequencies $\Delta\omega = \omega_2/\omega_1$. In Figure 4.4 we show that we can produce a behaviour that closely resembles that of Figure 4.1. This behaviour reveals that even under Militello et al's different interaction we still see the detuning and synchronisation phase effect. An
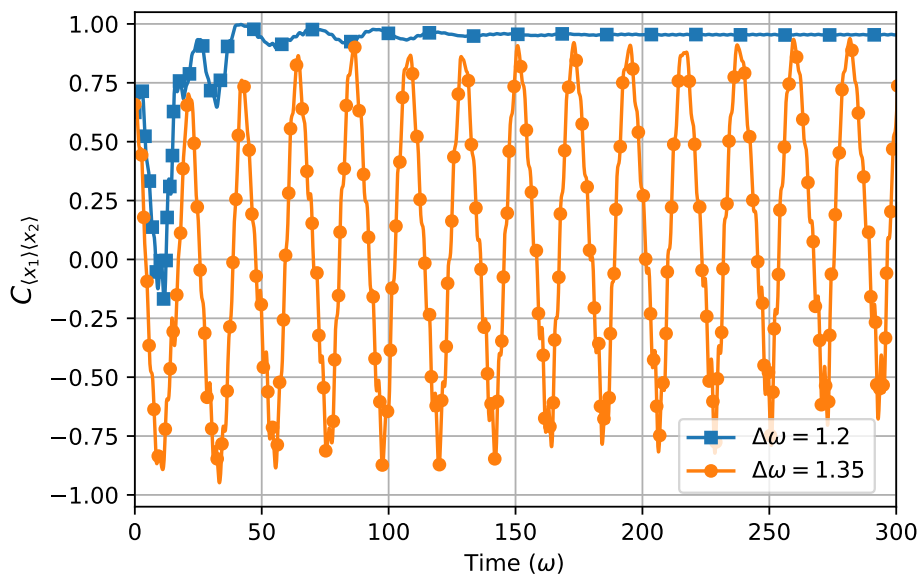
Figure 4.4: Synchronisation measure $C_{\langle X_1 \rangle, \langle X_2 \rangle}(t)$ of expectation value of mode positions for two regimes of detuning in Militello et al.'s model: $\Delta\omega = 1.2$ where synchronisation occurs and $\Delta\omega = 1.35$ where it does not. Initial state: $\rho_0 = |e_1\rangle\langle e_1| \otimes \rho_{vacuum} \otimes \rho_{coherent}$. Parameters $\Delta e = e_2 - e_1$, $\omega = \Delta e$, $g = \Delta e$, $\Gamma_{\sigma_-} = 0.2\Delta e$ [48].

important conclusion can be drawn from this result. Militello et al.'s model does not account for reorganisational energy changes to the coupling strengths of modes

or site energies when detuning mode frequencies, which we introduced to the dimer model in Section 4.2.1. Despite this we still see the same effect of detuning creating a phase difference which suggests that reorganisation energy changes are not the origin of the phase difference. Furthermore their model does not have any mode frequency dependence in its interaction Hamiltonian. This suggests the origin is not the interaction. To arrive at a satisfactory explanation for the origin of this phase difference we compare the two models studied so far in the following section.

4.2.4 Origin of Synchronisation Phase with Detuning

To begin we expand the interaction Hamiltonian of our dimer model to include sigma matrices for the exciton basis:

$$\Theta_1 = U(\theta)|e_1\rangle\langle e_1|U^\dagger(\theta) = \frac{1}{2}\left(\mathbb{1} - \cos 2\theta \sigma_z - \sin 2\theta \sigma_x\right) \tag{4.12}$$

$$\Theta_2 = U(\theta)|e_2\rangle\langle e_2|U^\dagger(\theta) = \frac{1}{2}\left(\mathbb{1} + \cos 2\theta \sigma_z + \sin 2\theta \sigma_x\right) \tag{4.13}$$

where we used trigonometric identities: $\cos^2\theta = \frac{1+\cos 2\theta}{2}$, $\sin^2\theta = \frac{1-\cos 2\theta}{2}$ and $\sin\theta\cos\theta = \frac{\sin 2\theta}{2}$. This results in:

$$H_I(dimer) = g(\cos 2\theta \sigma_z + \sin 2\theta \sigma_x)(X_2 - X_1) \tag{4.14}$$

where we have dropped the frequency dependence of the mode coupling strengths and the excitonic operators for now. As θ is small for the parameters of the bio-inspired dimer, this can be approximated as largely a σ_z interaction. Choosing $\phi_1 = \pi$ in Militello et al's model — as this results in the positive synchronisation with no detuning — we have:

$$H_I(\phi_1 = \pi) = g\sigma_x(X_2 - X_1) \tag{4.15}$$

Comparing the two shows that the main difference is the electronic operator σ_x vs σ_z. As mentioned above Militello et al.'s model does not account for frequency dependence of the mode couplings and is still able to produce the synchronisation phase when detuned therefore we can deduce that both a σ_x and σ_z coupling can produce the effect. Even though the Exciton-Vibration Dimer adaptation introduced in

Section 4.2.1 has a H_I that changes with detuning, it is clear that the main contribution to synchronisation phase does not arise from the interaction Hamiltonian alone, unlike the effect presented in Militello et al.'s study.

This leads us to considering the change in the vibrational Hamiltonian — which is identical in both models — and the resultant effect on the vibronic eigenstates that are formed in the system. An in-depth analysis of the role of vibronic eigenstates in synchronisation was discussed in Chapter 3 and so here we repeat only the fundamental points and expand. Recall the equations of motion for each mode's average position:

$$\langle X_1 \rangle = \sum_{j,k} \rho_{jk}(t) X_{1,kj}$$
$$\langle X_2 \rangle = \sum_{j,k} \rho_{jk}(t) X_{2,kj}$$

(4.16)

where $X_{i,kj} = \langle \psi_k | X_i | \psi_j \rangle$. When $\omega_1 = \omega_2$, the values of $X_{i,kj}$ were restricted to either equal or opposite upon switching of X i.e. each mode participated equally or oppositely in every vibronic coherence (see Table 3.1). As synchronisation is the result of one vibronic coherence significantly out-living others, the resultant synchronisation phase was either 0 $(C_{\langle X_1 \rangle, \langle X_2 \rangle} = 1)$ or π $(C_{\langle X_1 \rangle, \langle X_2 \rangle} = -1)$ depending on which coherence(s) dominated. Breaking the symmetry of $\omega_1 \neq \omega_2$ would lead to asymmetric participation of each mode in the vibronic eigenstates. In the far detuning extreme, one mode may be so far off-resonance with the system energy scales that it does not participate in system dynamics at all and synchronisation cannot occur. In the smaller detuning regime the eigenstates that are formed are not restricted to symmetric and anti-symmetric values in $X_{1,jk}$ and $X_{2,jk}$ and will instead have a range of amplitudes. The time dependent parts of Equation 4.16 remain equal for $\langle X_1 \rangle$ and $\langle X_2 \rangle$ but the weights of each oscillating component changes. Within the region of synchronisation, these amplitude differences are small and manifest as a constant phase difference between the oscillations of each $\langle X_i \rangle$. This can be seen clearly by expressing each amplitude as an exponential: $X_{i,kj} = e^{\kappa_{i,kj}}$. When an amplitude is negative, κ is a complex number and contributes a phase to the signal. Outside the

region of synchronisation, these differences are large, the signals are composed of different frequencies and have an unstable phase difference.

4.3   Quantum Correlations

One of our aims in investigating synchronisation in the quantum regime is to high-light any uniquely quantum properties of the phenomena. In the previous chapter we presented a fully quantum mechanism for synchronisation, as measured by the correlation function $C_{\langle X_1 \rangle, \langle X_2 \rangle}(t)$. We connected synchronisation to the interferences between quantum coherences, a subset of which contributed a relative-displacement collective motion to the dynamics and were also connected with increased magnitude of ET. This relative-displacement mode has previously been identified as exhibiting non-classical thermal fluctuations during ET [58]. Together this provides a good foundation of evidence of the quantum nature of synchronisation in these complexes. However, in an effort to quantify how 'quantum' this synchronisation is, in the following sections we investigate the dynamics of quantum correlations between the synchronising subsystems.

The quantum mutual information quantifies the total correlation between two subsystems and the quantum discord quantifies how much of this correlation is purely quantum. The quantitative relations between quantum synchronisation and quantum discord have been previously investigated. In the first study of spontaneous quantum synchronisation [25] the emergence of synchronisation was correlated with preservation of quantum discord. Since then it has been investigated in a range of quantum synchronisation settings [1, 3, 23, 25, 27, 44, 45, 86, 91]. Later it was shown that synchronisation is correlated with the generation of entanglement from an initially unentangled state [3]. Quantum mutual information has even been proposed as a measure of synchronisation that is capable of being used in both deep quantum and semi-classical regimes [1].

In the following we add evidence to the connection between synchronisation and quantum correlations. The detailed phase information provided by our adapted synchronisation measure introduced in Chapter 3, combined with the quantum correlation measures introduced in the next section, provides us with a unique perspective from which to relate the two properties. Specifically, we reveal that the synchronisation phase of the previous section indicates a change in magnitude of

quantum discord between the synchronising subsystems. This is of interest as it is evidence that our adapted synchronisation measure may be used to quantify a purely quantum feature.

4.3.1 Quantum Correlation Measures

The quantum mutual information $I(A:B)$ is a measure of the total correlations between two subsystems A and B of a larger quantum system AB [49] and is defined as:

$$I(A:B) = S(\rho_A) + S(\rho_B) - S(\rho_{AB}) \tag{4.17}$$

where $S(\rho) = -Tr\{\rho log\rho\}$ is the von Neumann entropy and density matrices $\rho_A = Tr_B\{\rho_{AB}\}$, $\rho_B = Tr_A\{\rho_{AB}\}$ are subsystems of ρ_{AB}. We want to know how much of this shared information is classical and how much is quantum. An efficient way to achieve this starts by evaluating the classical information one subsystem has of the other [30]. This method calculates the difference in von Neumann entropy of a subsystem before and after a measurement is acted on the other subsystem:

$$J(B|A) = \max_{A_i^\dagger A_i} \left\{ S(\rho_B) - \sum_i p_i S(\rho_B^i) \right\} \tag{4.18}$$

where

$$\rho_B^i = \frac{Tr_A\left\{A_i^\dagger A_i \rho_{AB}\right\}}{Tr_{AB}\left\{A_i^\dagger A_i \rho_{AB}\right\}} \tag{4.19}$$

is the residual state of B after measurement of $A_i^\dagger A_i$ — which are positive operator valued measurements (POVM) — on subsystem A and p_i is the probability of this outcome. The measurements $A_i^\dagger A_i$ are generated in a random order and continue until the sum of 4.18 satisfactorily converges on its maximum. Note that this equation would be different for the classical correlations from subsystem A to B, which we would label $J(A|B)$.

The remaining portion of the mutual information that is not classical must be

quantum [55]. The simplest way of evaluating this computationally is:

$$D(B|A) = I(A:B) - J(B|A) \tag{4.20}$$

where $D(B|A)$ is called the quantum discord.

## 4.3.2 Synchronisation and Quantum Correlations

Using Equations 4.18, 4.17 and 4.20 to calculate the quantum correlations between mode subspaces is relatively straightforward. By reminding ourselves of the structure of our dimer model in Section 2.1.1 we can see that density matrices for the subsystems are easily accessible. Intuitively we would expect some mutual information between modes to be maintained in a synchronised state as, if they were completely uncorrelated, then they should oscillate at independent frequencies and phases. Indeed from the analysis of Chapter 3 we know that, in the systems considered, synchronisation requires vibronic eigenstates with sufficient participation from both modes. We also postulate that these quantum correlations would not persist in the long-time limit if synchronisation is not achieved. The detuning scenarios introduced in the first half of this chapter provide the ideal regime to test this.

Figure 4.5 shows numerical calculations of the mutual information, quantum discord and classical information between the two intramolecular modes with PE545 parameters and for two different scenarios: Figure 4.5a shows a detuning of $\Delta\omega = 1.002$ in which synchronisation occurs and in Figure 4.5b a detuning of $\Delta\omega = 1.02$ in which synchronisation does not occur.

Firstly we notice a sharp increase in all correlations from uncorrelated initial state at 0 ps to a peak at around 0.4 ps. This is significant as we can state that the correlations do not originate from the initial state and are generated by the coherent interactions in our system. The peak at 0.4 ps exactly coincides with the coherent ET period that is characteristic of the dynamics in these bio-inspired vibronic dimers (see Figure 3.13b). We know the ET mechanism involves transitions between vibronic eigenstates which involve both modes, therefore it makes sense that the quantum correlations between the modes peak here too.
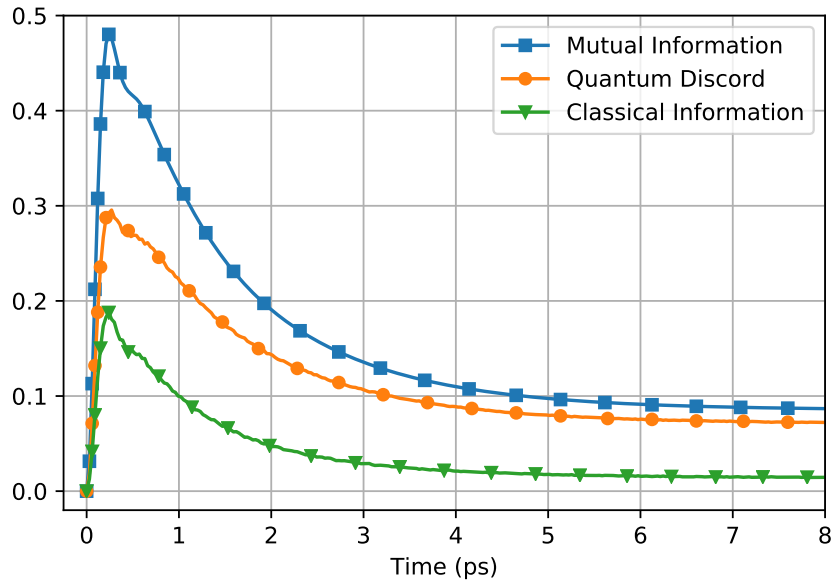
(a)
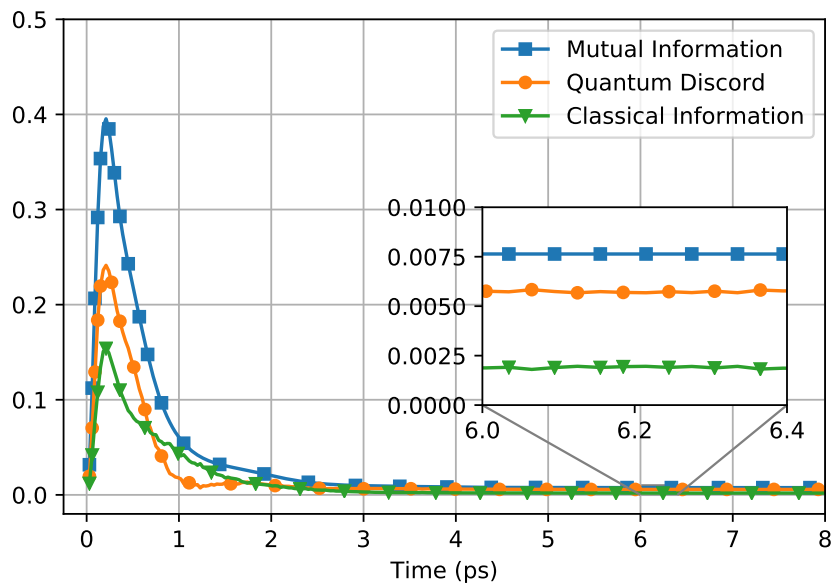
(b)

Figure 4.5: Dynamics of quantum mutual information, quantum discord and classical information between mode subsystems in the Exciton-Vibration Dimer model with PE545 parameters (Table 2.1) and initial state Equation 2.18 for two detuning scenarios (a) where synchronisation is achieved $\Delta\omega = 1.002$ and (b) where it is not $\Delta\omega = 1.02$.

Secondly we note the decay in correlations from 0.4 ps onward. This behaviour is due to the decay of coherent dynamics and the dominance of incoherent pro-

cesses. In the synchronising case of Figure 4.5a we see that the modes remain significantly correlated in the long time limit whereas in Figure 4.5b we see that correlations decay rapidly to a much lower value. This clear correlation between synchronisation and the preservation of quantum correlations is in agreement with previous findings.

Thirdly we note that in the synchronising case the majority fraction of the mutual information is quantum, as characterised by the quantum discord. In the non-synchronising case however, we see that there exists a time period within which classical information is greater than quantum discord. This leads us to hypothesise a novel connection between synchronisation and quantum correlations: for quantum synchronisation to occur, the quantum discord must always be greater than classical information, whereas for non-synchronising cases there may exist periods where the greater fraction of correlations are classical.

So far we have considered only the cases of synchronising and non-synchronising. Next we turn our attention to the in-between detuning regime that exhibits a synchronisation phase as found in the first half of this chapter. We measure the long-time stable value of quantum discord for a range of detuning regimes that exhibit a synchronisation phase. Figure 4.6 presents the long-time constant $C_{\langle X_1 \rangle, \langle X_2 \rangle}(t)$ value against the long-time stable quantum discord value (normalised to discord at no detuning) for two coherent regimes of our dimer model. The blue line is for the standard PE545 parameters and detunings from Figure 4.2, whereas the orange line is for the modified $\eta = 0.5$ regime from Section 3.5. This graph reveals that a larger synchronisation phase as measured by $C_{\langle X_1 \rangle, \langle X_2 \rangle}(t)$ indicates weaker quantum correlations between the modes. This is significant as we have given evidence that our modified synchronisation measure is able to infer a change in quantum discord between subsystems. Before further discussing the implications of this connection we show a similar behaviour in the model of Militello et al. introduced above.
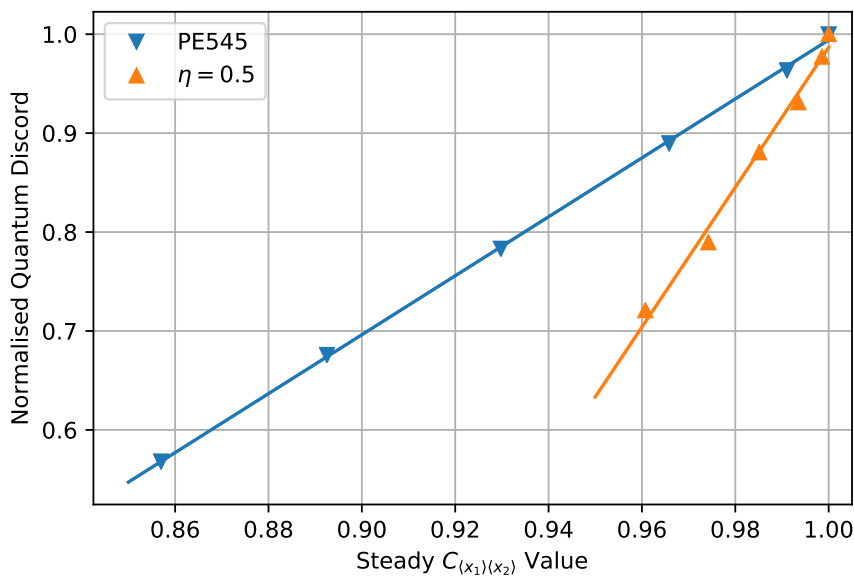
Figure 4.6: Long-time stable value of quantum discord between mode subsystems plotted against long-time stable value of synchronisation measure $C_{\langle X_1 \rangle, \langle X_2 \rangle}(t)$ of expectation value of mode positions. Each data point corresponds to a value of detuning and quantum discord is normalised to 1 for zero detuning. Two parameter regimes of the Exciton-Vibration Dimer are shown: standard parameters for PE545 (Table 2.1) and modified parameters $\eta = 0.5$ from Section 3.5. Linear regressions are plotted using standard methods to emphasise the relationship.

4.3.3 Quantum Correlations in Militello et al.'s Model

In the following we measure the quantum correlations between modes synchronising with a constant phase as produced by Militello et al.'s original interaction Hamiltonian changes. We previously showed the phases produced to be different from the effects we see with detuning. As the changes in ϕ_1 and ϕ_2 only change the mode observables and not the coupling strengths or frequencies of the modes, we expect that there will be no change in the quantum correlations between modes for all values of ϕ_1.

In Figure 4.7 we plot the long-time stable values of mutual information, classical information and quantum discord for a range of ϕ_1 alongside the long-time stable value of $C_{\langle X_1 \rangle, \langle X_2 \rangle}(t)$ which indicates the phase. Indeed we find that the long time correlations are unchanged by the phase introduced by the interaction Hamil-

tonian. The $C_{\langle X_1 \rangle, \langle X_2 \rangle}(t)$ dynamics presented as a function of ϕ_1 is exactly what we would expect from two sine waves with a constant phase shift between, as can be seen in the characterisation of our synchronisation function presented in Figure 3.1.
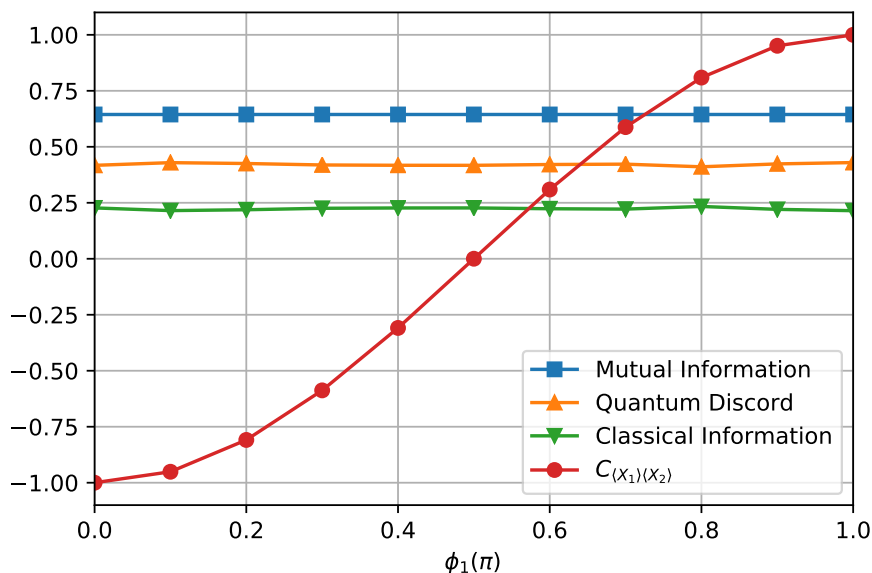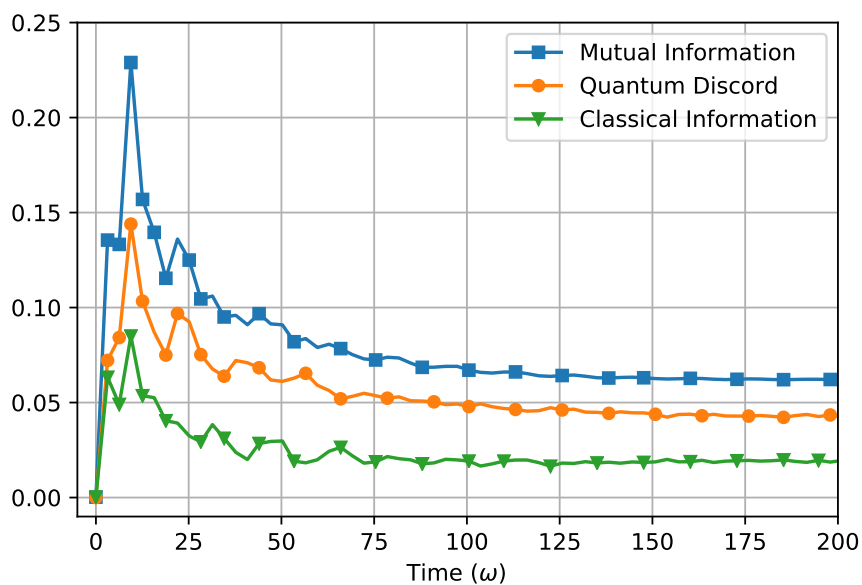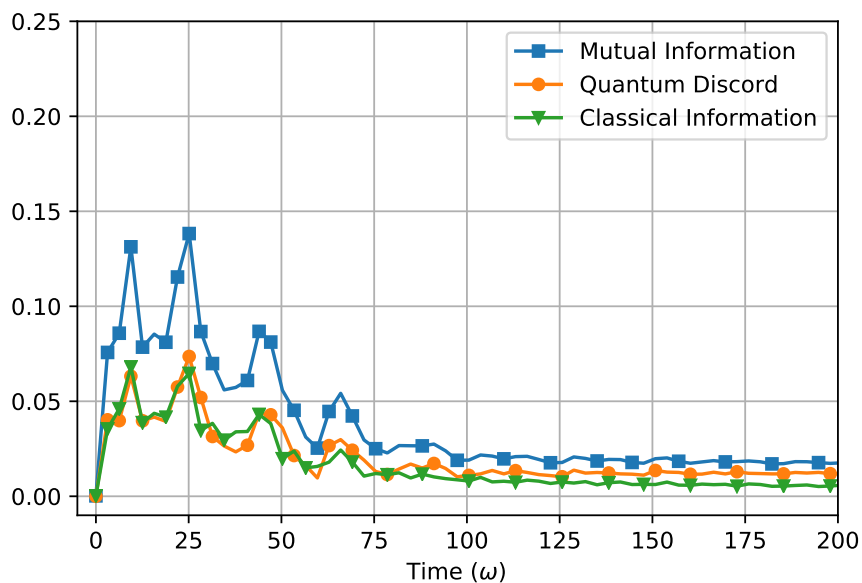

Figure 4.7: Long-time limit stable values of quantum mutual information, quantum discord and classical information between mode subsystems and long-time limit stable value of synchronisation function $C_{\langle X_1 \rangle, \langle X_2 \rangle}(t)$ of expectation values of mode positions. Both calculated as a function of ϕ_1 in Militello et al.'s interaction Hamiltonian (Equation 4.11) [48].

Finally we investigate the presence of synchronisation and quantum correlations in Militello et al's model for synchronising and non-synchronising regimes. We produce Figure 4.8 which is of the same form as Figure 4.5. We find the same qualitative relationship as in Exciton-Vibration Dimer model with detuning. It adds further evidence to our hypothesis that for a synchronising case the quantum discord is always larger than the classical information, whereas in the non-synchronising case classical information can, for some time periods, outweigh quantum discord.

(a)

(b)

Figure 4.8: Dynamics of quantum mutual information, quantum discord and classical information between mode subsystems in Militello et al.'s model for two detuning scenarios: (a) where synchronisation is achieved $\Delta\omega = 1$ and (b) where it is not $\Delta\omega = 1.35$. Initial state: $\rho_0 = |e_1\rangle\langle e_1| \otimes \rho_{vacuum} \otimes \rho_{coherent}$. Parameters $\Delta e = e_2 - e_1$, $\omega = \Delta e$, $g = \Delta e$, $\Gamma_{\sigma_-} = 0.2\Delta e$ [48].

4.4 Summary and Discussion

In this chapter we investigated the dynamics of synchronisation as a function of detuning in a bio-inspired vibronic dimer with Markovian dissipation and explored what forms of information about the synchronising subsystems can be captured by our synchronisation measure.

Firstly, we revealed that in the natural parameter regime synchronisation can occur with some detuning but with a constant phase difference in the synchronised state (which we call synchronisation phase). We showed that the origin of this synchronisation phase can be traced back to the vibrational Hamiltonian and the asymmetric participation of modes in vibronic eigenstates. We explained how the asymmetric coupling of vibronic eigenstates to local position operators introduced a phase between the expectation value of operators. We showed that the origin of synchronisation phase presented in an alternate model is different to what we observe, but also that the synchronisation phase as a function of detuning can be reproduced there. This suggests that the mechanism for synchronisation phase is a more general feature of synchronising quantum systems.

Secondly, we explored the relationship between synchronisation and quantum correlations. We showed that in the synchronising cases studied, the shared information between synchronising subsystems always has a majority share of quantum discord, whereas in the non-synchronising cases classical information is, at times, greater than the quantum discord. This is further evidence of the quantum nature of the synchronisation mechanism presented in this thesis. Furthermore we presented a novel connection between synchronisation phase and the degree of quantum correlations between synchronising subsystems. Quantum discord between synchronising subsystems decreases linearly as the synchronisation measure decreases from 1. This final result is worth emphasising. This effect is observable because of the adapted synchronisation measure we introduced in Chapter 3. The results here suggest that this measure is capable of capturing information about a purely quantum property of synchronising subsystems. This adds motivation to the use of synchronisation as a tool for exploring the quantum properties of a range of systems.

Generally in photosynthetic pigment-protein complexes there are multiple other quasi-coherent intramolecular modes that have different frequencies and coupling strengths to the system [18, 53]. Whilst many of these will be off-resonant with the system energy scales, there may be some that are harmonically resonant i.e. an integer multiple of the main frequency. These modes may participate in eigenstates and may be capable of exhibiting a form of synchronisation. This question is reserved for future work.

Chapter 5

Synchronisation Dynamics under non-Markovian Decoherence Effects

In this chapter we explore the effects of a non-Markovian environment on the dynamics of synchronisation of molecular motions in a bio-inspired exciton-vibration dimer. We reveal that the non-Markovian behaviour of the environment can have a positive or negative impact on synchronisation times depending on the system-environment coupling. Under moderate system-environment coupling, the time taken for synchronisation to emerge is positively correlated with the relaxation rate of the environment. However, under weak system-environment coupling, slow relaxation can have a stabilising effect on synchronisation. We propose a mechanism for the detrimental effects of a slowly relaxing environment on synchronisation by considering an effective mode representation of the environment and its effects on ET, which has been previously connected with synchronisation. Finally, we show that the synchronisation phase can be reproduced and is negatively correlated with the environment relaxation rate.

5.1 Introduction

So far we have seen that the form of dissipation in synchronising quantum systems is critical to the emergence of synchronisation. A natural question therefore is what effects would a non-Markovian environment and its associated complex decoherence processes have on the dynamics of synchronisation? As far as we are aware, this is unexplored in the quantum synchronisation literature.

For the majority of this thesis we have defined the combined TLS and modes (Exciton-Vibration Dimer) as our system of interest, allowing us to solve the joint electronic-vibrational dynamics and to develop a deep understanding the role of exciton-vibration coherence in the synchronisation process. We treated the environment as a perturbation to the system dynamics in the Markovian master equation (Equation 2.23). While this approach allowed us to capture the importance of decoherence in achieving synchronisation, it did not capture the full quantitative and qualitative influence of the thermal environments for the systems of interest. In recent years considerable effort has been put into deriving methods that are able to extend to arbitrarily strong system-environment couplings and to treat the system-environment interactions exactly [16].

One approach that is commonly used for solving excitation transfer dynamics in photosynthetic pigment-protein complexes is the Hierarchical Equations of Motion (HEOM) [80]. It is particularly useful as it can capture the effects of a reorganisation process of a complex solvent environment and is valid in the full range of system-environment coupling strengths [35, 78, 79].

There have been many studies which analyse the role of complex environments on a TLS. A common approach is to re-cast the bath into an effective single mode [34] or chain of modes [9, 8, 12, 32, 46, 62, 88]. The single mode picture allows the non-Markovianity of the environment to be included in a new larger system which then evolves under a modified Markovian master equation [34]. The chain modes picture allows efficient numerical techniques such as the time-adaptive Density Matrix Renormalisation Group to be applied [62]. By representing the environment as effective modes one can apply knowledge of interacting QHOs to gain a physical

insight into the effects on the system dynamics. Other methods such as the variational polaron approach have explained how system parameters such as the inter-site coupling are rescaled due to coupling to a bath [73] therefore altering the coherent dynamics.

In this chapter we use the HEOM method to explore the dynamics of synchronisation in a bio-inspired vibronic dimer. However, to provide physical insight we make use of a mapping of the environment as a chain of effective modes when interpreting the results.

The chapter is organised as follows: in Section 5.2.1 we introduce a description of environments with spectral density and correlation functions; in Section 5.2.2 we introduce the HEOM method for solving system dynamics; in Section 5.2.3 we show how environment correlations can be extracted from HEOM; in Section 5.2.4 we describe a representation of the Exciton-Vibration Dimer in non-Markovian environments; and in Section 5.2.5 we explain how we solve the HEOM numerically. The remaining sections are results: in Section 5.3.1 we report the effects of non-Markovian environments on the short time dynamics of synchronisation; in Section 5.3.2 we connect these synchronisation dynamics to the dynamics of the collective bath mode and ET; in Section 5.3.3 we show how the effects of the non-Markovian environment can be understood qualitatively with the use of an effective modes representation; in Section 5.3.4 we explore the effects of a non-Markovian environment on synchronisation phase as reported in Chapter 4. Finally in Section 5.4 we summarise and discuss.

5.2 Theoretical Formulation

5.2.1 Environment Correlation Function and Spectral Density

In the master equation formalism described in Section 2.3.1 the precise form of the environment H_E and its interactions with the system of interest H_I (see Equation 2.21) were not explicitly stated. Instead we constructed Lindblad-form dissipators which can phenomenologically describe a variety of environment effects. Here we describe a correlation-function approach which describes more complex structured environments.

The influence of a general environment on the system can be represented by a correlation function of the form: $C_{jj}(t + \Delta t) = \langle E_j(t + \Delta t)E_j(t)\rangle$ where E_j is the environment operator coupled to system operator S_j. Assuming linear system-environment coupling and a general bosonic environment the interaction Hamiltonian takes the form: $H_I = \sum_j S_j \otimes \sum_{jq} g_{jq} \left(b_{jq} + b_{jq}^\dagger\right)$ where S_j is an operator of the electronic system, $E_j = \sum_{jq} g_{jq} \left(b_{jq} + b_{jq}^\dagger\right)$ is the environment operator, and $\left(b_{jq} + b_{jq}^\dagger\right)$ is the position operator of the local harmonic mode q. For this interaction the correlation functions take a well-known form [47]:

$$
\begin{aligned}
C(t) &= \sum_q g_q^2 \left((1+B)e^{i\omega_q t} + Be^{-i\omega_q t}\right) \\
&= \frac{1}{\pi} \int_0^\infty d\omega J(\omega) \left(\coth \frac{\omega}{2k_B T} \cos \omega t - i \sin \omega t\right)
\end{aligned}
\tag{5.1}
$$

where B is the mean number of quanta in a thermally occupied mode (as specified in Section 2.3.3) and the function $J(\omega)$ is known as the spectral density which captures the coupling strength g_q of a continuum of environment QHOs of different frequencies ω_q to the system of interest and in general can be represented mathematically as $J(\omega) = \pi \sum_q g_q^2 \delta(\omega - \omega_q)$. We have suppressed subscripts jj here (and from here on) as we only consider identical, local and uncorrelated environments coupled to system operators S_j.

In the context of bio-inspired vibronic dimers as described so far, an accurate environment is well captured by a combination of spectral densities of different forms. The effects of damped motions of the solvent and protein scaffold are often

represented by a power law rise in coupling strength followed by a decay after a cut-off frequency [51], however the most appropriate form of this cut-off still debated [38]. Here we choose a Drude-Lorentz cut-off to form the spectral density for its wide use in bio-inspired ET calculations [35, 77, 79]:

$$J_D(\omega) = 2\lambda_D\omega\frac{\gamma_D}{\omega^2 + \gamma_D^2} \tag{5.2}$$

where λ_D is the reorganisation energy of the environment, γ_D is the cut-off frequency and we restrict to $\omega > 0$. From here on we refer to this type of environment as a Drude bath.

This broad continuum of frequencies is often combined with narrow peaks to more accurately represent a bio-inspired environment. These narrow peaks represent strongly-coupled intramolecular motions of the chromophores and their properties can be determined from fluorescence spectroscopy [15, 60, 85]. These have spectral densities of the form:

$$J_q(\omega) = 2\lambda_q\omega_q^2\frac{\gamma_q\omega}{\left(\omega^2 - \omega_q^2\right)^2 + \gamma_q^2\omega^2} \tag{5.3}$$

where mode q has frequency ω_q, reorganisation energy λ_q, and is underdamped at rate γ_q, and again we restrict to $\omega > 0$.

The associated correlation functions for these spectral densities can be exponentially expanded. For the Drude bath this has the form:

$$C_D(t) = c_D^{(0)}e^{-\gamma_D t} + \sum_{m=1}^{\infty} c_D^{(m)}e^{-\nu_m t} \tag{5.4}$$

where $c_D^{(0)} = \gamma_D\lambda_D\left(\cot\frac{\gamma_D}{2k_BT} - i\right)$ and $c_D^m = \frac{4k_BT\lambda_D\gamma_D\nu_m}{\nu_m^2 - \gamma_D^2}$ and Matsubara frequencies are $\nu_m = 2\pi k_BTm$. For the underdamped modes it has the form:

$$C_q(t) = c_q^+e^{-\nu_q^+ t} + c_q^-e^{-\nu_q^- t} + \sum_{m=1}^{\infty} c_q^{(m)}e^{-\nu_m t} \tag{5.5}$$

where $c_q^{\pm} = \pm i\frac{\lambda_q\omega_q^2}{2\sqrt{\omega_q^2 - \gamma_q^2/4}}\left(\cot\frac{\nu_q^{\pm}}{2k_BT} - i\right)$ and $c_q^{(m)} = \frac{-4k_BT\lambda_q\gamma_q\omega_q^2\nu_m}{(\omega_q^2 + \nu_m^2)^2 - \gamma_q^2\nu_m^2}$ and $\nu_q^{\pm} = \frac{\gamma_q}{2} \pm$

$i\sqrt{\omega_q^2 - \gamma_q^2/4}$.

We note that the dominant exponential in the expansion of the correlation function for a Drude bath has exponent $-\gamma_D t$. This means that the inverse of the cut-off frequency characterises the main timescale of dissipation of the environment reorganisation energy, in other words, the relaxation rate of the bath. This is a useful parameter for exploring non-Markovianity as it effectively determines the timescale in which non-Markovian effects can take place. Shorter relaxation times are closer to a memory-less Markovian approximation.

5.2.2 Hierarchical Equations of Motion for Open Quantum Systems Dynamics

The Hierarchical Equations of Motion (HEOM) method for calculating the dynamics of a reduced system makes use of the exponential form of environment correlation functions introduced above. It is formed of a set of coupled differential equations each of which tracks part of the system-environment interaction. The solutions of the equations are often presented as an interconnected pyramid of auxiliary density matrices (ADOs), where the system density matrix is at the top and descending down the pyramid contains contributions from system-environment interactions of increasing order. The derivation, based on path-integrals, is given fully elsewhere [35, 77, 79] and here we present and explain the general form:

$$
\begin{aligned}
\dot{\sigma}_{\underline{n}}(t) = {} & -i[H_S, \sigma_{\underline{n}}(t)] - \sum_{jk} n_{jk} v_{jk} \sigma_{\underline{n}}(t) \\
& -i\sum_{jk} \left(S_j \sigma_{\underline{n}_{jk}^+}(t) - \sigma_{\underline{n}_{jk}^+}(t) S_j^\dagger \right) \\
& -i\sum_{jk} n_{jk} \left(c_{jk} S_j \sigma_{\underline{n}_{jk}^-}(t) - \sigma_{\underline{n}_{jk}^-}(t) c_{jk}^* S_j^\dagger \right)
\end{aligned}
\tag{5.6}
$$

where S_j is the system operator that couples the system to the environment in H_I, where v_{jk} are the exponents and c_{jk} are the amplitudes of each exponential in the expansion of the environment correlation functions (Equation 5.4 and 5.5). The multi-index $\underline{n}$ is a vector of length $j \times k$ that records an order value for each jk element and is used to label each auxiliary density matrix in the hierarchy. For example

if we consider two environments $j = \{1,2\}$ that both require two exponential terms $k = \{1,2\}$, the vector $\underline{n}$ then has 4 elements corresponding to $(n_{11}, n_{12}, n_{21}, n_{22})$ which each take an integer value corresponding to the order that each exponential is taken to. The notation $\sigma_{\underline{n}_{jk}^{\pm}}$ refers to an auxiliary matrix where one vector element n_{jk} differs by ± 1 from the element in $\underline{n}$ from $\sigma_{\underline{n}}$.

We can dissect Equation 5.6 into its contributions from different levels of the hierarchy. For any ADO, the dynamics can be broken down into the following contributions: the first line is the action of the system Hamiltonian plus exponential decays due to the environment character; the second line is contributions from higher order matrices in the hierarchy and the third line is contributions from lower order matrices. This equation produces a complex inter-connected set of equations of motion that must all be solved in parallel. The HEOM can be organised by grouping the auxiliary matrices by their tier value: $T_n = \sum_{jk} n_{jk}$. These 'tiers' represent corrections in the system-environment coupling to the order of at least $2T_n$. Using the example environments given above we notate each density matrix as $\sigma_{n_{21}n_{22}}^{n_{11}n_{12}}$. In this example first three tiers of the hierarchy would look like:

$$
\begin{aligned}
T_n = 0 &\implies \sigma_{00}^{00}, \\
T_n = 1 &\implies \sigma_{10}^{00} \sigma_{01}^{00} \sigma_{00}^{10} \sigma_{00}^{01}, \\
T_n = 2 &\implies \sigma_{20}^{00} \sigma_{11}^{00} \sigma_{02}^{00} \sigma_{10}^{10} \sigma_{01}^{01} \sigma_{10}^{01} \sigma_{01}^{10} \sigma_{00}^{20} \sigma_{00}^{11} \sigma_{00}^{02}
\end{aligned}
\tag{5.7}
$$

5.2.3 Environment Observables within HEOM

Previous works have shown that the first tier of the ADOs in the HEOM contains information on the system-environment correlations [37, 41, 69, 92]. The original derivation extracted the expectation value of the general environment operator [37] but more recently the extraction of contributions from individual environment components was detailed [69]. This is derived in the following.

The equation of motion for the system can be derived by tracing out the envi-

ronment from a global state ρ_G and its Hamiltonian H_G:

$$
\begin{aligned}
\dot{\rho}_S(t) &= Tr_E\left\{-i[H_G,\rho_G]\right\} \\
&= -i[H_S,\rho_S] - iTr_E[H_I,\rho_G] \\
&= -i[H_S,\rho_S] - i\sum_j [S_j, Tr_E\{E_j\rho_G\}]
\end{aligned}
\tag{5.8}
$$

Since ρ_G here is a density operator defined in the full Hilbert space, the partial trace $Tr_E\{E_j\rho_G\}$ returns an operator on the system Hilbert space. An equation for the system can also be determined from the HEOM at zeroth order. From Equation 5.6 we have:

$$
\dot{\rho}_S(t) = \dot{\sigma}_{00}^{00}(t) = -i[H_S, \sigma_{00}^{00}] - i\sum_{jk}\left[S_j, \sigma_{\underline{n}}(T_n = 1)\right]
\tag{5.9}
$$

where $\sigma_{\underline{n}}(T_n = 1)$ restricts the sum to only the first tier of ADOs. Comparing the two equations we can find that:

$$
\sum_j Tr_E\{E_j\rho_G\} = \sum_{jk}\sigma_{\underline{n}}(T_n = 1)
\tag{5.10}
$$

which shows that information about the environment operator is contained in the first tier of ADOs. As the expected value of the environment operator E_j coupled to the system is given by: $\langle E_j \rangle = Tr_S\{Tr_E\{E_j\rho_G\}\}$ we must trace out the system from the ADOs. For the environments considered we defined $E_j = g_j\left(b_j + b_j^\dagger\right) = g_j X_j$ meaning that this extracted environment operator is proportional to the position operator, which is what we want to study in synchronisation. Thus we can arrive at equations for the expectation values of position operators which are comparable to those used in previous chapters. Furthermore by careful ordering of the exponential terms in $C(t)$ that enter the HEOM we can extract the ADO that contains the contribution from a specific sub-environment.

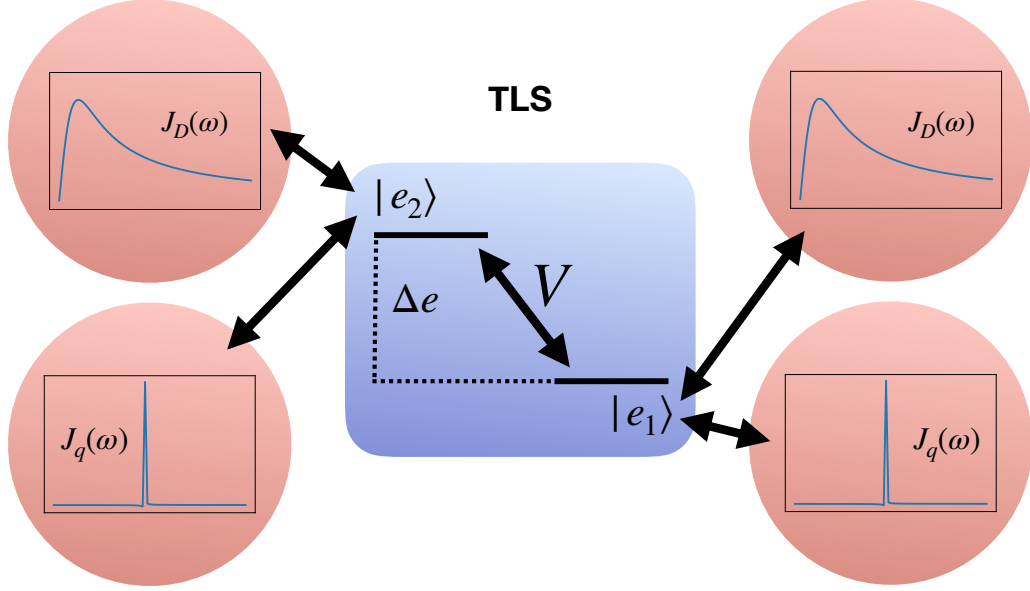### 5.2.4 Representing the Exciton-Vibration Dimer

Figure 5.1: Schematic illustration of a bio-inspired vibronic dimer coupled to non-Markovian environments. Each site $|e_i\rangle$ is coupled to an environment described by a broad Drude-Lorentz spectral density $J_D(\omega)$ and a narrow peaked spectral density $J_q(\omega)$.

We aim to construct a HEOM that represents the exciton-vibration dimer studied throughout this thesis. As shown in the previous section it is possible to extract environment observables from the HEOM. This eliminates the need to include the synchronising modes in our system of interest and drastically reduces computation time (see Section 5.2.5). We consider separate environments on each site of our system, each having a spectral density that is a combination of a Drude bath and a single underdamped intramolecular mode:

$$C(t) = c_D^{(0)} e^{-\gamma_D t} + \sum_m c_D^{(m)} e^{-\nu_m t} + c_q^+ e^{-\nu_q^+ t} + c_q^- e^{-\nu_q^- t} + \sum_{m'} c_q^{(m')} e^{-\nu_{m'} t} \quad (5.11)$$

where m and m' are the counters for Matsubara terms in the Drude bath and underdamped mode spectral densities respectively.

We can extract the desired environment observables by using Equation 5.10:

$$\langle X_1 \rangle = Tr_S \left\{ \sigma_{1k_{q^+}} + \sigma_{1k_{q^-}} + \sum_{m'} \sigma_{1k_{m'}} \right\}$$
$$\langle X_2 \rangle = Tr_S \left\{ \sigma_{2k_{q^+}} + \sigma_{2k_{q^-}} + \sum_{m'} \sigma_{2k_{m'}} \right\}$$

$$(5.12)$$

where we have labelled the ADOs with the exponential terms from our specific environment correlation function (Equation 5.11). We are also interested in the position of the collective coordinate of the Drude bath:

$$\langle X_{D2} \rangle = Tr_S \left\{ \sigma_{2k_D} + \sum_m \sigma_{2k_m} \right\}$$

$$(5.13)$$

The parameter regime we investigate is inspired by the central dimer $PEB_{50/61}$ of pigment-protein complex PE545 which is introduced in Section 2.1.4. Here we repeat the important values for reference: inter-site energy splitting Δe = 1042 cm^{-1}; inter-site coupling V = 92 cm^{-1}; mode energies initially set equal at $\omega_2 = \omega_1 = 1111$ cm^{-1} where reorganisation energies $\lambda_1 = \lambda_2 = \omega_1 S_1 = 64$ cm^{-1} (see Section 4.2.1); we consider identical Drude bath environments on each site with reorganisation energy $\lambda_D = 110$ cm^{-1} [57] and cut-off frequencies $\gamma_D = 100$ cm$^{-1} = [0.053 \text{ ps}]^{-1}$. These parameters correspond to a low temperature regime i.e. the important energy scales are larger than the thermal temperature $\frac{\Delta e}{k_B T} \approx 5$ and $\frac{\omega}{k_B T} \approx 5$. This has implications for the numerical implementation which we discuss in the next section. We fix our initial state of the system as the higher energy exciton state and the environments at equilibrium with the system in its ground state. This choice is equivalent to the initial state of previous chapters which we justified in Section 2.1.3 and it allows us to compare results between Markovian and non-Markovian regimes.

5.2.5 Numerical Implementation

In the following we give an example to unpack the form of Equation 5.6 and explain how this can be calculated. Choosing σ_{10}^{00} as an example ADO we can see how Equation 5.6 works:

$$
\begin{aligned}
\dot{\sigma}_{10}^{00}(t) = {} & -i[H_S, \sigma_{10}^{00}(t)] - ((0)v_{11} + (0)v_{12} + (1)v_{21} + (0)v_{22})\,\sigma_{10}^{00} \\
& -i\left(S_1\sigma_{10}^{10} + S_1\sigma_{10}^{01} + S_2\sigma_{20}^{00} + S_2\sigma_{11}^{00}\right) \\
& +i\left(\sigma_{10}^{10}S_1^\dagger + \sigma_{10}^{01}S_1^\dagger + \sigma_{20}^{00}S_2^\dagger + \sigma_{11}^{00}S_2^\dagger\right) \\
& -i\left((0)c_{11}S_1\sigma_{10}^{00} + (0)c_{12}S_1\sigma_{10}^{00} + (1)c_{21}S_1\sigma_{00}^{00} + (0)c_{22}S_1\sigma_{10}^{00}\right) \\
& +i\left(\sigma_{10}^{00}(0)c_{11}^*S_1^\dagger + \sigma_{10}^{00}(0)c_{12}^*S_1^\dagger + \sigma_{00}^{00}(1)c_{21}^*S_1^\dagger + \sigma_{10}^{00}(0)c_{22}^*S_1^\dagger\right)
\end{aligned}
\tag{5.14}
$$

which, noting the n_{jk} elements that are zero, can be reduced to:

$$
\begin{aligned}
\dot{\sigma}_{10}^{00}(t) = {} & -i[H_S, \sigma_{10}^{00}(t)] - v_{21}\sigma_{10}^{00} \\
& -i\left(S_1\sigma_{10}^{10} + S_1\sigma_{10}^{01} + S_2\sigma_{20}^{00} + S_2\sigma_{11}^{00}\right) \\
& +i\left(\sigma_{10}^{10}S_1^\dagger + \sigma_{10}^{01}S_1^\dagger + \sigma_{20}^{00}S_2^\dagger + \sigma_{11}^{00}S_2^\dagger\right) \\
& -i\left(c_{21}S_1\sigma_{00}^{00} - \sigma_{00}^{00}c_{21}^*S_1^\dagger\right)
\end{aligned}
\tag{5.15}
$$

We note that each ADO has dimensions equal to that of the system. Numerical implementation of the HEOM requires construction of all the ADO equations of motion and simultaneously solving. The inclusion of a large number tiers is desirable for accuracy but rapidly becomes computationally intractable. It is therefore desirable to use the smallest necessary system size, the minimum number of exponential terms in the correlation function expansion of the environments and the minimum number of tiers the HEOM is calculated to, whilst maintaining accuracy.

Treating the underdamped modes as part of the environment allowed us to keep the system size small and computationally accessible whilst maintaining access to the desired environment information. A reduction can be made in the number of exponential terms in each environment by combining the Matsubara terms of the Drude bath and underdamped mode [79]. This provides a computational benefit but

also means that the contributions from Matsubara terms in Equations 5.12 and 5.13 are all contained in one term and cannot be separated as we have shown. However, in the parameter regimes we explore we find that the contributions from each Matsubara term are negligible in comparison to the other terms in Equations 5.12 and 5.13. In this case we may discard the Matsubara terms in the calculation of environment observables, allowing their combination in the correlation functions and providing a computational speed up whilst maintaining accuracy. We emphasise that this does not affect the Matsubara term contributions to the dynamics of the system or other ADOs.

The numerical implementation we use here makes use of two convergence improvements for the number of tiers required: firstly a rescaling of all density matrices is implemented such that the higher tier matrices become vanishingly small and enable earlier truncation [72]; and secondly a Markovian truncation which replaces correlation functions in the penultimate tier with delta functions [36]. The latter is particularly useful for accuracy in low temperature regimes, where the characteristic energy scales of the system are larger than the environment temperature which we have in the case studied in this thesis. The code used to solve the HEOM was originally written by Richard Stones in Python 3 and is adapted by the author of this work.

5.3 Results

In the following sections we numerically explore the dynamics of synchronisation of intramolecular mode displacements during the ET process of the exciton-vibration dimer in the presence of non-Markovian decoherence processes.

We vary the system-bath interaction via the reorganisation energy λ_D and cut-off frequency γ_D whilst keeping all other parameters constant. λ_D and γ_D alter the shape of the bath spectral density and therefore the correlation function that enters the HEOM. We select two reorganisation energy regimes: the first represents moderate system-bath coupling where $\lambda_D = 110$ cm^{-1} is comparable to inter-site coupling of the dimer $V = 92$ cm^{-1} and mode reorganisation energy $\lambda_q = 64$ cm^{-1} and the second representing weak system-bath coupling where $\lambda_D = 11$ cm$^{-1} <$ $\lambda_q < V$. In both these regimes we then vary the relaxation time of the Drude bath with the cut-off frequency: $\gamma_D = 100$ cm$^{-1} = [0.053$ ps$]^{-1}$, $\gamma_D = 400$ cm$^{-1} = [0.013$ ps$]^{-1}$ and $\gamma_D = 1600$ cm$^{-1} = [0.003$ ps$]^{-1}$.

We expect the dynamics of synchronisation and ET to be different to the Markovian case for two main reasons. Firstly, we recall from the results of Chapter 3 that the emergence of synchronisation depends on a separation of timescales of electronic and vibrational coherence. Coupling the system to a non-Markovian bath introduces a complex multi-exponential decoherence process which may disrupt the balance necessary for synchronisation. Secondly, these processes may also inhibit the ET mechanism, which, also from the results of Chapter 3 we know would inhibit synchronisation.

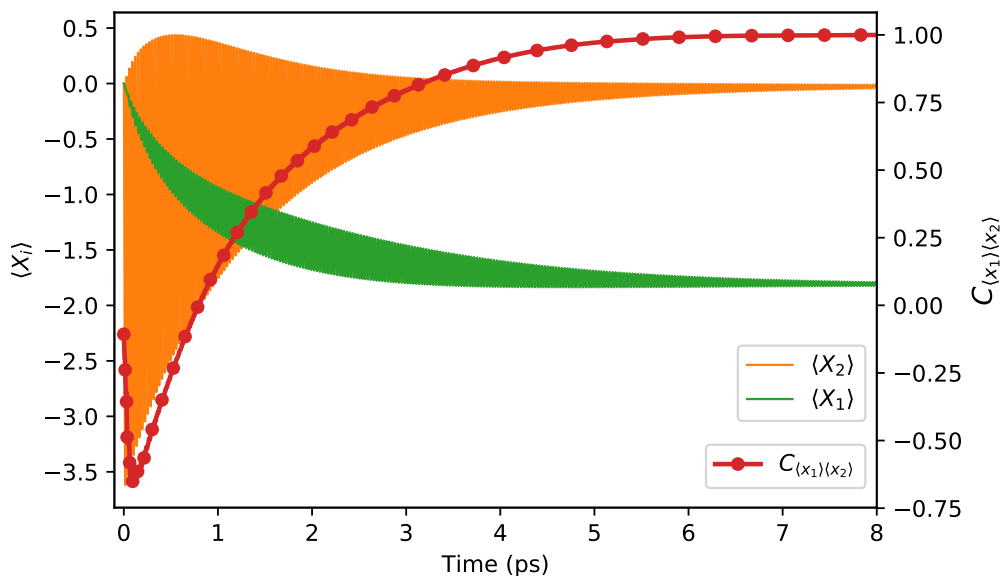### 5.3.1 Effects of non-Markovian Environments on Synchronisation Dynamics

Figure 5.2: Expectation value of mode positions and their synchronisation $C_{\langle X_1 \rangle \langle X_2 \rangle}(t)$ for the bio-inspired dimer with non-Markovian environments as described in Section 5.2.4.

Using the parameters specified in Section 5.2.4, we calculate the dynamics of synchronisation and display our results in Figure 5.2. We observe that positive synchronisation is still achieved but its emergence is delayed until around 8 ps. We find the characteristic negative synchronisation dip that we showed to be concomitant with coherent energy transfer and vibronic coherence involving the two excitons as discussed in Chapter 3. This suggests that the same ET mechanism is still present.

Figure 5.3a displays the synchronisation dynamics for the three values of γ_D and the same reorganisation energy as Figure 5.2. We observe that the dynamics follow the same profile but synchronisation is reached within a shorter timescale for faster bath relaxation. For faster relaxation the dynamics approach that of the Markovian regime of Figure 3.6 which is expected. This behaviour suggests that slow relaxation of the bath is detrimental to synchronisation time. However, the picture for $\lambda_D = 11$ cm^{-1} in Figure 5.3b reveals that under weak system-bath coupling slower bath relaxation can be beneficial for synchronisation. For fast bath

relaxation $\left(\gamma_D = 1600\ \text{cm}^{-1}\right)$ the synchronisation measure oscillates in a pattern reminiscent of the purely coherent vibronic dimer of Figure 3.3 and does not reach a stable phase in the timescale presented. This result is what would be expected from a Markovian regime with weak system-bath coupling (slow dephasing rate). For slower bath relaxation $\gamma_D = 100, 400\ \text{cm}^{-1}$ the phase dynamics are more stable and positive synchronisation emerges in the timescale presented. This suggests that in certain regimes slow bath relaxation can be beneficial to synchronisation.

Furthermore by comparing the lines of equal γ_D in Figure 5.3b and 5.3a we can see the effect of increasing the system-bath coupling strength alone on the synchronisation dynamics. In the weaker system-bath coupling of Figure 5.3b synchronisation emerges on a shorter timescale. In this regime the system-mode coupling is stronger than the system-bath coupling and therefore dynamics of the system becomes more dominated by interaction with the modes. We postulate that this reduces synchronisation times by enhancing ET and we will show evidence for this in the next section.

Overall the results of Figure 5.3 show that the non-Markovian nature of an environment coupled to a synchronising complex can have a positive and negative impact on synchronisation times. In order to gain more insight into the mechanism behind its effect on synchronisation we analyse the dynamics of ET and the expectation value of the environment operator in the next section.
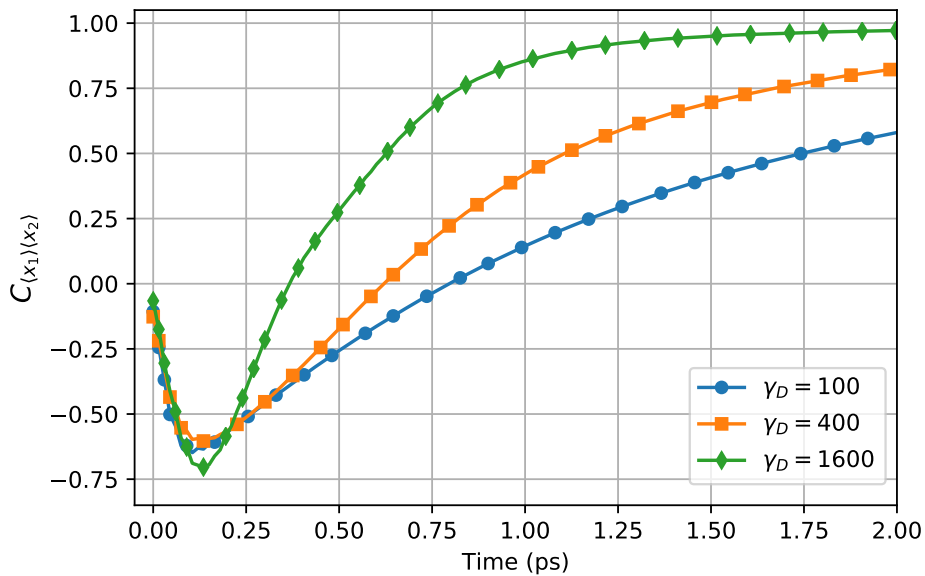
(a)
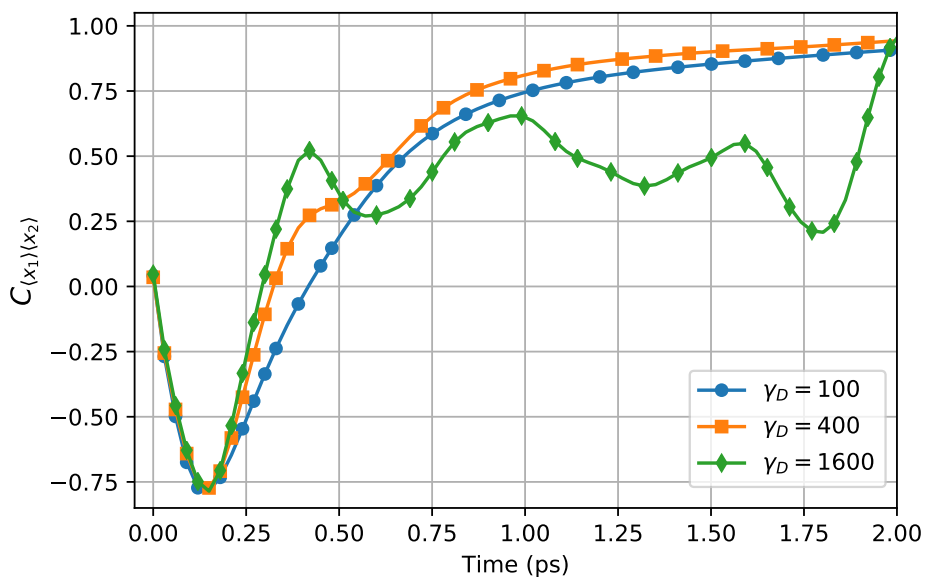
(b)

Figure 5.3: Synchronisation dynamics of mode positions as a function of Drude bath relaxation rate (cut-off frequency γ_D) and for two regimes of system-bath coupling (a) $\lambda_D = 110\,\text{cm}^{-1}$ (b) $\lambda_D = 11\,\text{cm}^{-1}$. Values of γ_D labelled in-figure in units of cm^{-1}.

### 5.3.2 Bath Displacement and Excitation Transport Dynamics

At $t = 0$ the ADOs in HEOM are set to zero which corresponds to the environments being at equilibrium with the system's ground state. In the first instant after the system is excited the environments coupled to each site are displaced and begin to relax towards a new equilibrium position with the system. At early times, the rate at which this relaxation takes place is dominated by γ_D. As the bath relaxation timescales we consider here $[0.003 - 0.05 \text{ ps}]^{-1}$ are shorter than the characteristic coherent ET timescale $[0 - 1 \text{ ps}]$, we can witness the bath relaxation by examining the average value of the collective bath operator at early times. The initial state for the system is almost entirely excited on a single site and therefore the Drude bath coupled to this site will be displaced towards a new equilibrium position at a rate proportional to γ_D. This behaviour can be observed in the expectation value of the bath operator which we labelled $\langle X_{D2} \rangle$ in Equation 5.13. In Figure 5.4 we show the dynamics of $\langle X_{D2} \rangle$ over the synchronisation period for both system-bath coupling regimes and bath relaxation times described in the previous section.

In the insets of both Figure 5.4a and 5.4b we display the short time displacements of $\langle X_{D2} \rangle$. Immediately we can see that they follow an exponential decay with decay constants approximately equal to $\gamma_D = 100$ cm^{-1} = $[0.053 \text{ ps}]^{-1}$, $\gamma_D = 400$ cm^{-1} = $[0.013 \text{ ps}]^{-1}$ and $\gamma_D = 1600$ cm^{-1} = $[0.003 \text{ ps}]^{-1}$. This is numerical assurance that the cut-off frequency characterises the timescale of reorganisation of the bath due to the changes in the system. It corroborates our understanding that high cut-off frequencies have faster synchronisation times as they are closer to the Markovian approximation of instantaneous bath reorganisation.

However, this is not the only effect of changing the cut-off frequency. The dynamics of $\langle X_{D2} \rangle$ on a longer time-scale change dramatically as a function of γ_D in both the strong and weak coupling regimes. To help us understand this behaviour we finally turn to analysing the electronic system. In particular we measure the population of the higher energy exciton state $|E_2\rangle$ as a function of γ_D and both system-bath coupling regimes and present our results in Figure 5.5.
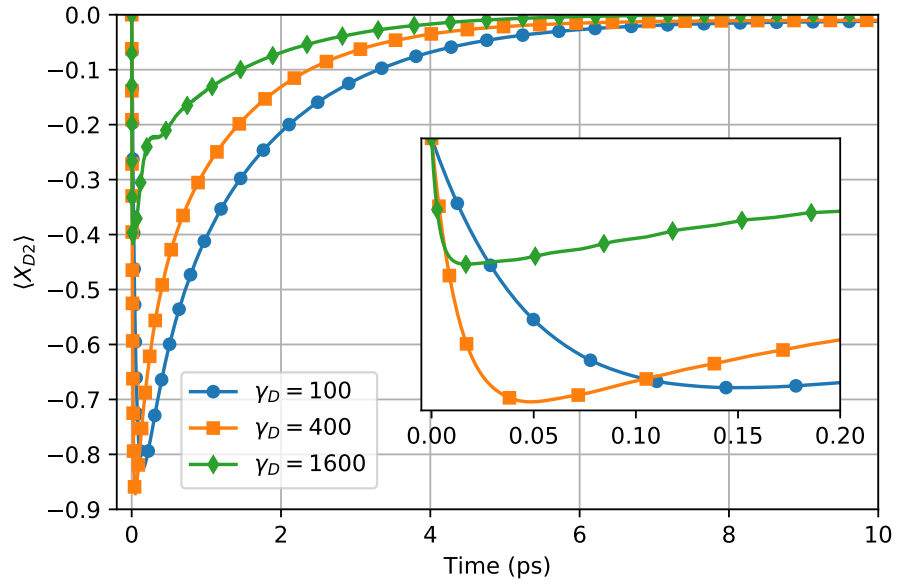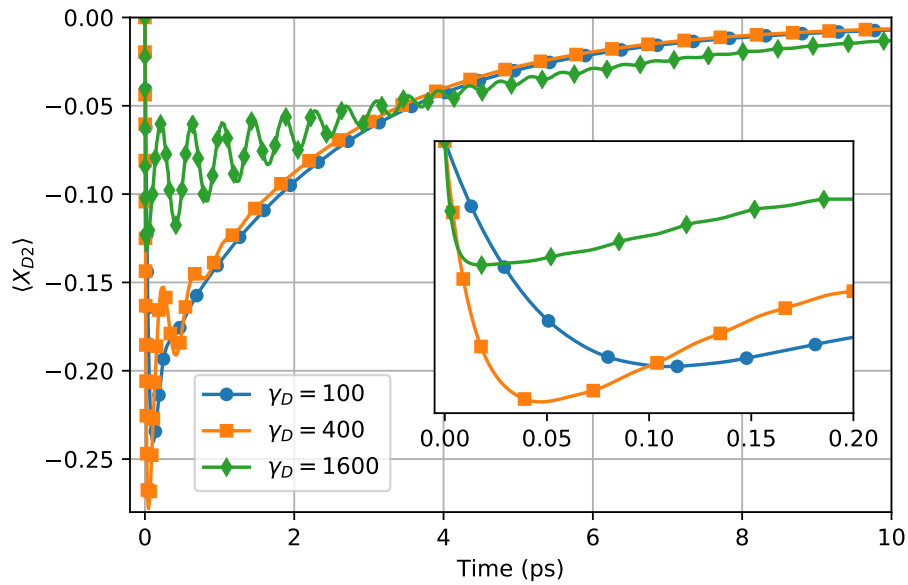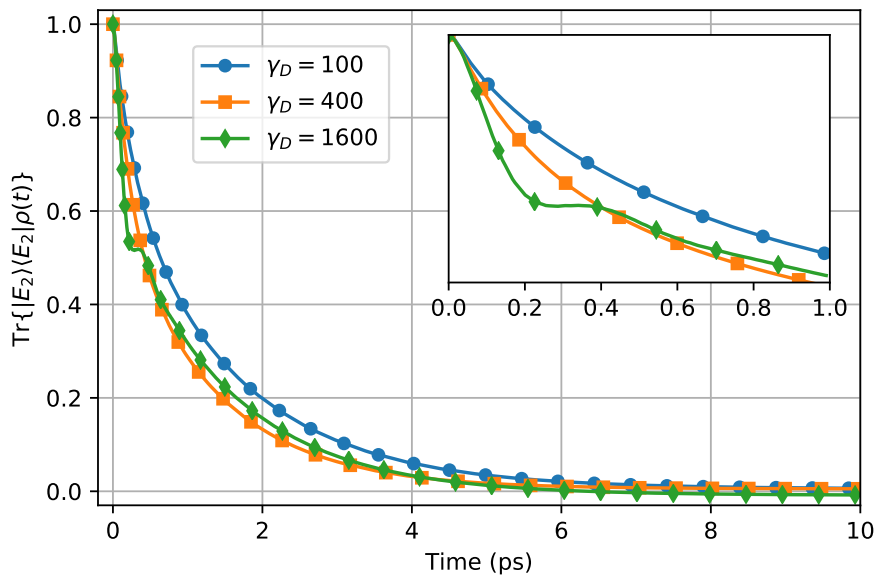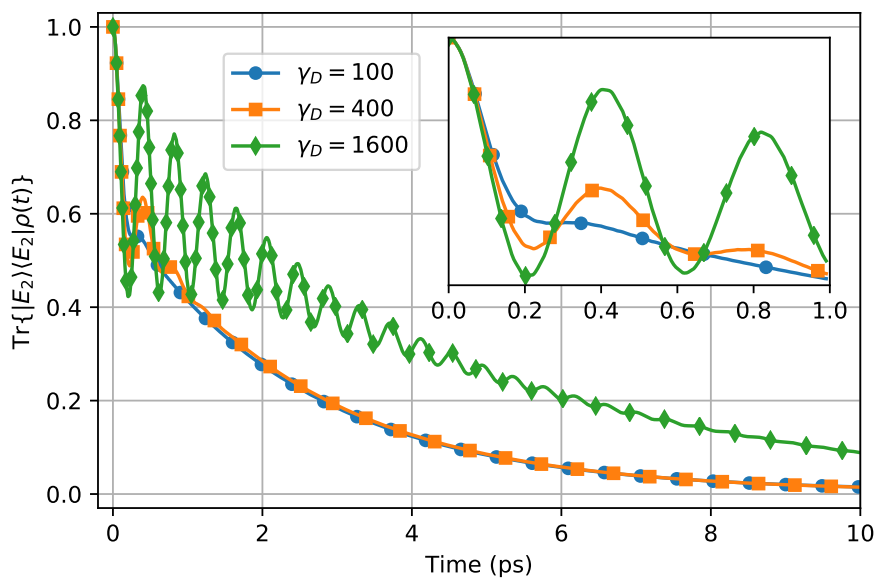
Figure 5.4: Expectation value of Drude bath environment operator as a function of Drude bath relaxation rate γ_D and for two regimes of system-bath coupling (a) $\lambda_D = 110 \text{ cm}^{-1}$ (b) $\lambda_D = 11 \text{ cm}^{-1}$. Values of γ_D labelled in-figure in units of cm^{-1}.

(a)

(b)

Figure 5.5: Population of higher energy exciton state $|E_2\rangle$ as a function of Drude bath relaxation rate γ_D and for two regimes of system-bath coupling (a) $\lambda_D = 110$ cm^{-1} (b) $\lambda_D = 11$ cm^{-1}. Values of γ_D labelled in-figure in units of cm^{-1}.

We observe that ET, represented here by the change in population of $|E_2\rangle$, also changes as a function of bath relaxation rate. The changes follow the same pattern as that of the synchronisation of mode positions in Figure 5.3. As mentioned above this is what we expect if we consider the connection between ET and synchronisation in the exciton-vibration dimer with Markovian environments of Chapter 3. We can use the understanding gained from these works to infer a mechanism for the effects of non-Markovian bath we see here.

Firstly, the oscillation pattern in exciton population for $\gamma_D = 1600$ cm^{-1} in Figure 5.5b can be identified as the same coherent oscillation as observed for the closed system evolution of the Exciton-Vibration Dimer in Figure 2.3. This is clear evidence that the HEOM reproduces the same coherent ET dynamics that has been studied throughout this thesis. These oscillations are what would be expected from the Exciton-Vibration Dimer evolving under weak electronic dephasing. Fast bath relaxation, $\gamma_D = 1600$ cm^{-1}, and weak system-bath coupling approximates to this. The oscillation in $C_{\langle X_1 \rangle \langle X_2 \rangle}(t)$ of Figure 5.3b is exactly what would be expected of this very coherent regime. Furthermore we can see that the oscillations in $\langle X_{D2} \rangle$ at high γ_D are a reaction to the site population oscillations. The bath is relaxing almost instantaneously to its new equilibrium and thus follows the change in population of $|E_2\rangle$.

Secondly when the system-bath coupling is increased, which is presented in Figure 5.5a, coherent ET is suppressed. As mentioned in the previous section, the balance between reorganisation energies of modes and Drude baths determines how much each component contributes to the system dynamics. From Chapter 3 we know that the coherent ET mechanism requires system-mode interaction. When the system interacts more strongly with the Drude bath, the ability for the system to interact with the modes is inhibited. This suppresses coherent ET mechanism which, also from the results of Chapter 3, we know slows the emergence of synchronisation.

Finally, we observe that lower cut-off frequencies destroy the coherent ET in both the weak and moderate system-bath coupling regimes, which as we expect also

slows synchronisation. However, in the weak system-bath coupling regime this is beneficial as it acts to stabilise ET and synchronisation.

Demonstrating the effects of slow bath relaxation on the coherent ET mechanism helped us understand the effects on synchronisation however it does not satisfactorily explain the mechanism. In order to gain further insight we consider the effective modes representation of the Drude bath in the following section.

5.3.3   Drude Bath and Effective Modes Picture

As mentioned in the introduction to this chapter, several works [9, 8, 12, 32, 46, 62, 88] have shown that it is possible to exactly map a complex non-Markovian environment to a chain of modes. Each new mode has an effective frequency and effective coupling strength to its neighbour in a one dimensional (1D) chain. This then allows the dynamics to be solved using, for example, the time-adaptive Density Matrix Renormalisation Group technique [62]. In the following we show that considering a 1D chain representation of the non-Markovian environment provides a clearer physical perspective from which to understand its effects on synchronisation.

Figure 5.6 is a schematic diagram of the system-environment complex with the Drude bath cast into a series of modes. The nearest neighbour coupling strengths g_{c_n} and chain mode frequencies ω_{c_n} can be found analytically for specific spectral densities [12] but for a Drude bath they are calculated numerically [62]. As we are not interested in calculating exact dynamics here and only require a qualitative picture, we use the analytic formulas for an ohmic spectral density with exponential cut-off in the following discussion: $\omega_{c_n} \approx \gamma_D(2n+2)$ [12].

The first point to note from viewing the bath as a chain of modes is the change of overall picture from two underdamped modes interacting via a TLS with complex decoherence processes, to many modes competing for interaction with the TLS. If the effective bath modes are near resonant with the system energy splitting then they are able coherently interact and exchange energy with the system in a similar way the the quasi-coherent underdamped modes. If the effective bath modes are more strongly coupled to the system than the underdamped modes, then the interaction between system and underdamped modes would be reduced. As explained in the previous section this would result in an inhibition of the ET mechanism and therefore a slowing of synchronisation. We find that this mechanism can explain the results observed for different bath relaxation rates in the previous section.

Firstly we consider the case of $\gamma_D = 1600$ cm^{-1} where we have shown the dynamics of synchronisation are similar to the Exciton-Vibration Dimer under Marko-
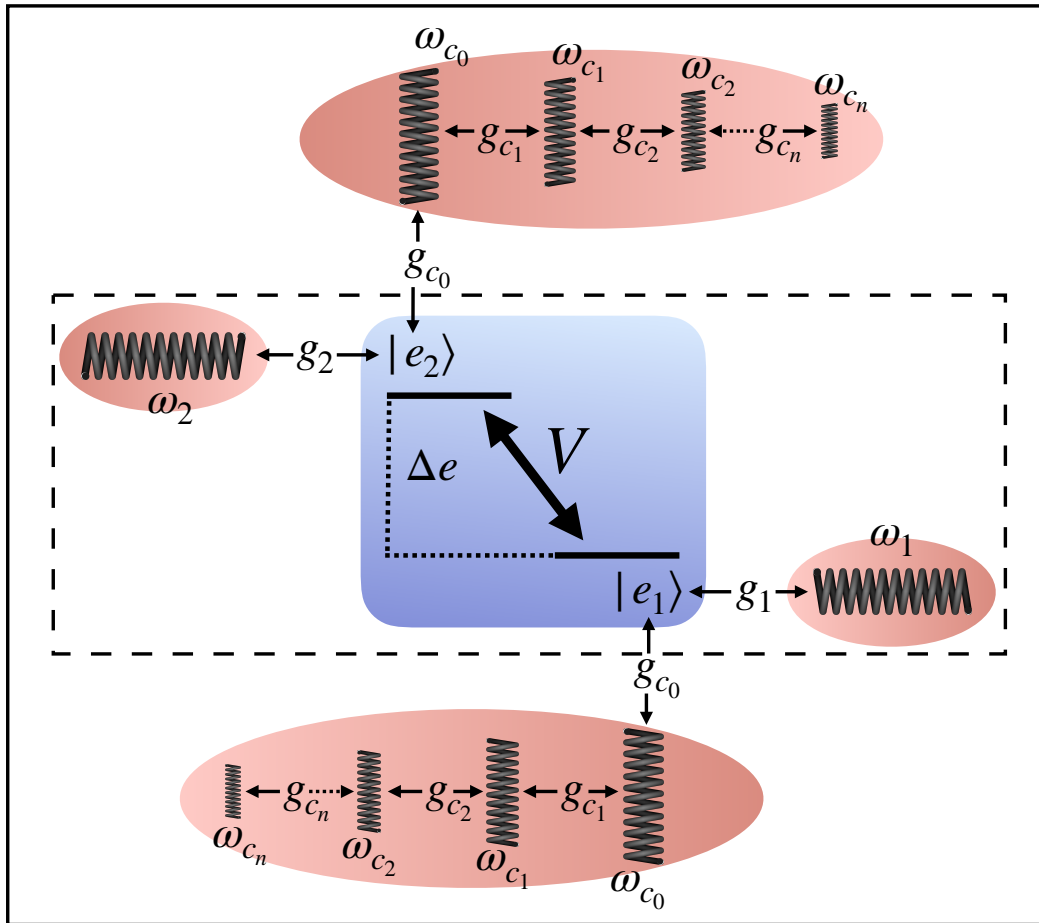
Figure 5.6: Schematic representation of the system-environment complex with Drude baths represented as chains of modes. Each site $|e_{1(2)}\rangle$ of a TLS is coupled to an underdamped mode of energy $\omega_{1(2)}$ with strength $g_{1(2)}$ and a 1D chain of modes where coupling to the first mode of energy ω_{c_0} is g_{c_0}. Coupling strengths of remaining modes in chain are between nearest neighbours only. Dotted line shows the boundary of the Exciton-Vibration Dimer introduced in Chapter 2.

vian decoherence processes. In this case the first bath mode would have a frequency of approximately $2\gamma_D = 3200$ cm^{-1}. This frequency is much larger than the system energy splitting of $\Delta e = 1048$ cm^{-1} which means it is not likely to coherently interact with the system. The next mode in the chain would have an even larger frequency of approximately $4\gamma_D$ and would participate even less. Hence the interaction with the quasi-resonant underdamped modes dominates the coherent dynamics, and this regime more closely resembles that of the Exciton-Vibration Dimer.

For a more slowly relaxing bath however, multiple modes in the chain must be considered. For $\gamma_D = 100$ cm^{-1} the bath mode frequencies along the chain $\omega_{c_0} = 200$, $\omega_{c_1} = 400$, $\omega_{c_2} = 600$, $\omega_{c_3} = 800$, $\omega_{c_4} = 1000$ cm^{-1} become closer to the system energies. In this case the system will interact with multiple modes along the chain and therefore its interaction with the underdamped modes is decreased. The same logic again applies: less interaction with underdamped modes, leads to inhibited ET, which leads to slower synchronisation.

5.3.4 Synchronisation Dynamics of Detuned Modes with non-Markovian Environments
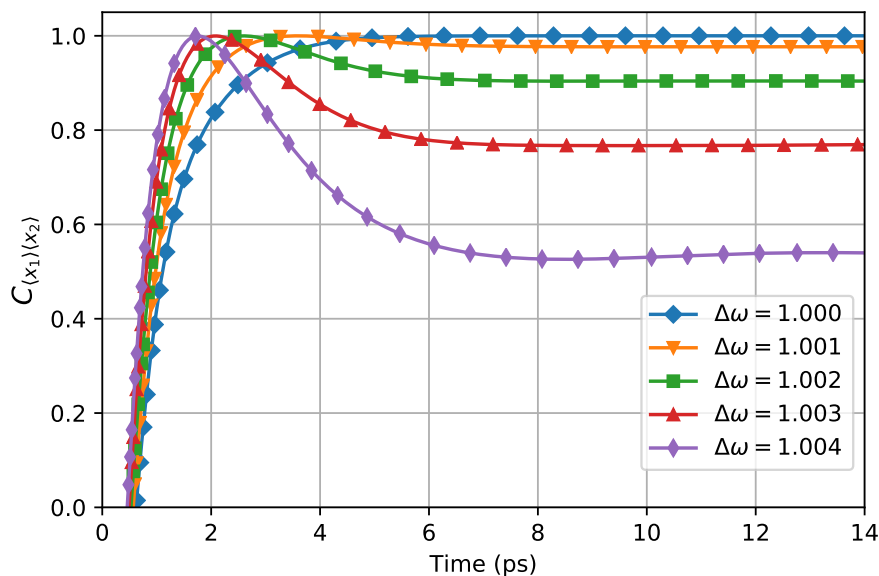

Figure 5.7: Synchronisation measure of expectation value of mode positions for a range of mode frequency detunings. Parameters listed in Section 5.2.4 except for $\gamma_D = 400$.

In this final section we investigate the effects of bath relaxation rates on the ability of detuned modes to synchronise. Firstly we demonstrate that we are able to reproduce the synchronisation phase as a function of detuning as seen in Chapter 4. This is displayed in Figure 5.7 for moderate system-bath coupling $\lambda_D = 110$ cm^{-1} and cut-off frequency $\gamma_D = 400$ cm^{-1}. The fact that we observe the same relationship as seen in the Markovian regime consolidates the results of both chapters. It is evidence that the synchronisation phase observed is not an artefact of a simplified Markovian environment and arises under more complex decoherence processes. It also provides further numerical assurance that including the underdamped modes as part of the environment in the HEOM produces results equivalent to calculating the quantum dynamics of the full exciton-vibration dimer.

In order to probe the effects of the non-Markovian bath on the synchronisation phase we fix the detuning $\Delta\omega = 1.002$ we vary γ_D and present the dynamics in Figure 5.8. We find that faster bath relaxation times, which are beneficial to syn-
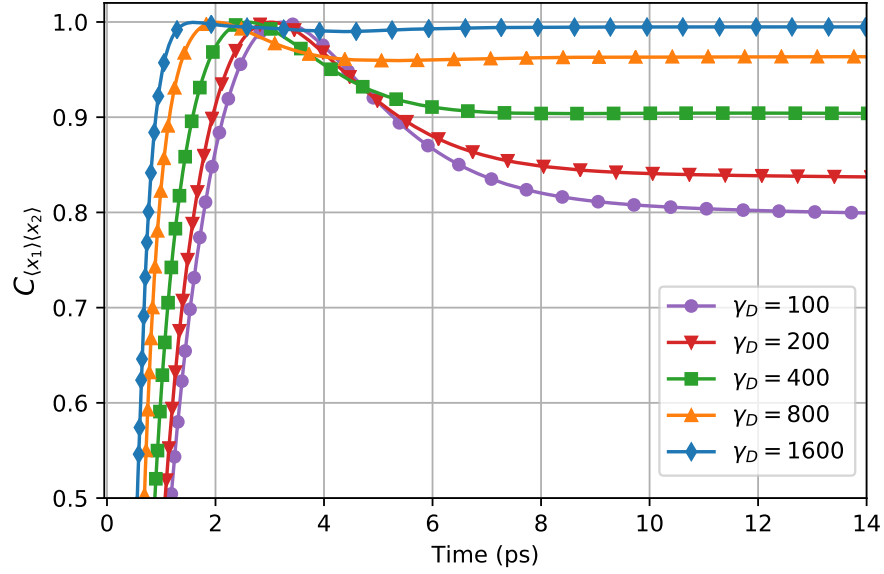
Figure 5.8: Synchronisation measure of expectation value of mode positions for a range of bath relaxation rates γ_D and fixed mode frequency detuning $\Delta\omega = 1.002$. Other parameters listed in Section 5.2.4.

chronisation time in this regime, decrease the synchronisation phase. We know from the results of Chapter 4 that stronger system-mode interaction reduces the synchronisation phase produced by detuning. In other words it makes the synchronisation more robust to detuning. As discussed in the previous section, the effect of a slower relaxing bath is to introduce competing bath modes into the system-environment complex which weakens the interaction between system and underdamped modes. The results here corroborate our findings in the previous section. Applying the results of Chapter 4 one step further, we postulate that slower bath relaxation rates also reduce the quantum correlations between underdamped modes. We discuss this further in the following section.

5.4 Summary and Discussion

Throughout this chapter we have used the physical insight gained from studying the dynamics of the Exciton-Vibration Dimer in the Markovian regime to help us interpret results in the non-Markovian regime. This is justified as the HEOM method is exact in its treatment of system-environment interactions. Any interactions between system and underdamped modes that are present in the Markovian regime are accounted for in the non-Markovian regime. Indeed the fact that we observe the same features such as the negative synchronisation period in Figure 5.2, the coherent ET oscillations in Figure 5.5b and the synchronisation phase of Figure 5.7 all suggest that the Exciton-Vibration mechanisms identified with the Master equation approach are also present in our HEOM approach. However, in our implementation of the HEOM method we do not track the full quantum state of the underdamped modes. This means we cannot determine the presence of Exciton-Vibration coherences using the same approach as the previous chapters. Furthermore, in Section 5.3.4 we postulated that a slower bath relaxation rate reduces the quantum correlations between the modes. Again we are not able to use the same method as in previous chapters to measure this. To obtain full quantum states of the modes with the HEOM method would be too computationally expensive. Obtaining more information about state of the environments from the HEOM ADOs has been shown to be possible [69] and could be a focus of future work.

The results of this chapter contribute to two distinct fields of research. To the field of bio-inspired energy transfer it provides further evidence that synchronisation is a useful perspective from which to view the complex electronic-vibrational interactions of vibronic dimers. We have shown that the phenomena persists in the presence of more realistic non-Markovian environments.

To quantum synchronisation studies, the results can be viewed as an investigation of synchronisation of two QHOs coupled through a single TLS which is coupled to independent non-Markovian baths. It is shown that the properties of the non-Markovian baths can control synchronisation of the QHOs, specifically affecting the time taken for synchronisation to emerge and the robustness to detuning.

Furthermore it shows that the results of Chapter 4 persist in the presence of non-Markovian environment couplings which suggests that the synchronisation phase as a function of detuning and the reported mechanism is a more general feature of quantum synchronisation.

To summarise we have investigated the synchronisation dynamics of the displacements of modes in a bio-inspired vibronic dimer during energy transfer in non-Markovian environments. As far as we are aware, this has not been explored before. We have presented numerical evidence that a slowly relaxing bath is detrimental to synchronisation, except in the regime where ET is very coherent, where slow relaxation can have a stabilising effect. This suggests that the properties of a subset of non-Markovian environments can be used to control synchronisation of other environment operators which are coupled to the same TLS. Furthermore we showed that the non-Markovian environment weakens the robustness of synchronisation to detuning. These effects can be understood qualitatively by considering the competition between underdamped modes and effective chain modes of the slowly relaxing bath for interaction with the system.

Chapter 6

Summary

In this final chapter we summarise the main results of the thesis and highlight the key contributions made.

In Chapter 3 we presented an in-depth analysis of the mechanism of quantum synchronisation between two molecular vibrations in a bio-inspired vibronic dimer experiencing Markovian dissipation and decoherence. We presented a novel adaptation to a well-established synchronisation measure that enabled us to establish previously unreported connections between the synchronisation of molecular motions and electronic energy transfer. Specifically we revealed that the mechanism of quantum synchronisation is fundamentally a decoherence-mediated competition between interfering quantum coherences. The exciton-vibration coherences that support coherent excitation transfer also drive the vibrations towards a negatively synchronised state. Hence we revealed that the presence of a negatively synchronised transient between molecular vibrations is an indicator of excitonic coherence. Lastly, we showed that enhanced energy transfer is correlated with faster emergence of synchronisation. This demonstrated that quantum synchronisation between molecular motions could be controlled by adjusting the electronic system they are coupled to.

In Chapter 4 we demonstrated how information about the quantum correlations between synchronising subsystems can be captured by our adapted synchronisation measure. We presented an analysis of the dynamics of synchronisation as a function of detuning in the same system as Chapter 3 and revealed that, as seen in the

classical regime, synchronisation can occur with a non-integer phase difference between the oscillations. We presented a quantum mechanism for this phase based on the asymmetric participation of molecular vibrations in vibronic eigenstates. By measuring quantum correlations between the synchronising subsystems we consolidated previous reports of a positive relationship between the preservation of quantum discord and a synchronised state. Our unique contribution was to reveal that the synchronisation phase we measure can capture information about the degree of quantum correlations between synchronising subsystems.

In Chapter 5 we presented the first investigation of the influence of non-Markovian environment effects on synchronisation in a bio-inspired vibronic dimer. We showed that the presence of a slowly relaxing bath is detrimental to the emergence time of synchronisation. However, under weak system-bath coupling, a slowly relaxing bath can have a beneficial stabilising effect on synchronisation. We demonstrated that this effect can be understood physically by considering the competition between molecular vibrations and effective bath vibrations for interaction with the system.

Overall this thesis investigated in-depth the synchronisation of molecular motions in a bio-inspired vibronic dimer. It emphasises the physical insight that can be gained from exploring quantum synchronisation phenomena in these settings. It contributes further understanding to both the quantum dynamics of bio-inspired dimers and the fundamental mechanisms involved in quantum synchronisation.

Appendix A

Analytics of Markovian Master Equation

In this appendix we detail the form of the time evolution of an element of our density matrix under Markovian dissipation. The full master equation is as follows:

$$
\begin{aligned}
\dot{\rho}(t) = & -i\left(H\rho - \rho H\right) \\
& + \Gamma_{deph}\left(|e_1\rangle\langle e_1|\rho|e_1\rangle\langle e_1| - \frac{1}{2}\rho|e_1\rangle\langle e_1| - \frac{1}{2}|e_1\rangle\langle e_1|\rho\right) \\
& + \Gamma_{deph}\left(|e_2\rangle\langle e_2|\rho|e_2\rangle\langle e_2| - \frac{1}{2}\rho|e_2\rangle\langle e_2| - \frac{1}{2}|e_2\rangle\langle e_2|\rho\right) \\
& + \Gamma_{th}(1+B)\left(b_1\rho b_1^\dagger - \frac{1}{2}\rho b_1^\dagger b_1 - \frac{1}{2}b_1^\dagger b_1\rho\right) \\
& + \Gamma_{th}(B)\left(b_1^\dagger\rho b_1 - \frac{1}{2}\rho b_1 b_1^\dagger - \frac{1}{2}b_1 b_1^\dagger\rho\right) \\
& + \Gamma_{th}(1+B)\left(b_2\rho b_2^\dagger - \frac{1}{2}\rho b_2^\dagger b_2 - \frac{1}{2}b_2^\dagger b_2\rho\right) \\
& + \Gamma_{th}(B)\left(b_2^\dagger\rho b_2 - \frac{1}{2}\rho b_2 b_2^\dagger - \frac{1}{2}b_2 b_2^\dagger\rho\right).
\end{aligned}
\tag{A.1}
$$

We solve for each element separately. The Hamiltonian evolution contributes:

$$
-i\langle\psi_j|\left(H\rho - \rho H\right)|\psi_k\rangle = -i\Omega_{jk}\rho_{jk}.
\tag{A.2}
$$

The pure dephasing on site 1 (site 2 is easily substituted) has the form:

$$\langle\psi_j|\left(|e_1\rangle\langle e_1|\rho|e_1\rangle\langle e_1|-\frac{1}{2}\rho|e_1\rangle\langle e_1|-\frac{1}{2}|e_1\rangle\langle e_1|\rho\right)|\psi_k\rangle=$$

$$\left(\sum_\alpha\sum_{q,n_1,n_2}C(q,n_1,n_2)\langle E_q,n_1,n_2|e_1\rangle\langle e_1|\psi_\alpha\rangle\sum_{\alpha'}\sum_{q',n_1',n_2'}C(q',n_1',n_2')\langle\psi_{\alpha'}|e_1\rangle\langle e_1|E_q',n_1',n_2'\rangle\right.$$

$$-\frac{1}{2}\sum_\alpha\sum_{q,n_1,n_2}C(q,n_1,n_2)\langle E_q,n_1,n_2|\psi_\alpha\rangle\sum_{\alpha'}\sum_{q',n_1',n_2'}C(q',n_1',n_2')\langle\psi_{\alpha'}|e_1\rangle\langle e_1|E_q',n_1',n_2'\rangle$$

$$\left.-\frac{1}{2}\sum_\alpha\sum_{q,n_1,n_2}C(q,n_1,n_2)\langle E_q,n_1,n_2|\psi_\alpha\rangle\sum_{\alpha'}\sum_{q',n_1',n_2'}C(q',n_1',n_2')\langle\psi_{\alpha'}|e_1\rangle\langle e_1|E_q',n_1',n_2'\rangle\right)\Gamma_{deph}\rho_{\alpha,\alpha'}.$$

$$(A.3)$$

The elements for thermal dissipation have the form:

$$\langle\psi_j|\left(b_1\rho b_1^\dagger-\frac{1}{2}\rho b_1^\dagger b_1-\frac{1}{2}b_1^\dagger b_1\rho\right)|\psi_k\rangle=$$

$$\left(\sum_\alpha\sum_{q,n_1,n_2}\sqrt{n}C(q,n_1,n_2)\langle E_q,n_1-1,n_2|\psi_\alpha\rangle\sum_{\alpha'}\sum_{q',n_1',n_2'}\sqrt{n'+1}C(q',n_1',n_2')\langle\psi_{\alpha'}|E_q',n_1'+1,n_2'\rangle\right.$$

$$-\frac{1}{2}\sum_\alpha\sum_{q,n_1,n_2}(n+1)C(q,n_1,n_2)\langle E_q,n_1,n_2|\psi_\alpha\rangle\sum_{\alpha'}\sum_{q',n_1',n_2'}C(q',n_1',n_2')\langle\psi_{\alpha'}|E_q',n_1',n_2'\rangle$$

$$\left.-\frac{1}{2}\sum_\alpha\sum_{q,n_1,n_2}C(q,n_1,n_2)\langle E_q,n_1,n_2|\psi_\alpha\rangle\sum_{\alpha'}\sum_{q',n_1',n_2'}(n')C(q',n_1',n_2')\langle\psi_{\alpha'}|E_q',n_1',n_2'\rangle\right)\Gamma_{th}(1+B)\rho_{\alpha,\alpha'},$$

$$(A.4)$$

and:

$$\langle\psi_j|\left(b_1^\dagger\rho b_1-\frac{1}{2}\rho b_1 b_1^\dagger-\frac{1}{2}b_1 b_1^\dagger\rho\right)|\psi_k\rangle=$$

$$\left(\sum_\alpha\sum_{q,n_1,n_2}\sqrt{n+1}C(q,n_1,n_2)\langle E_q,n_1+1,n_2|\psi_\alpha\rangle\sum_{\alpha'}\sum_{q',n_1',n_2'}\sqrt{n'}C(q',n_1',n_2')\langle\psi_{\alpha'}|E_q',n_1'-1,n_2'\rangle\right.$$

$$-\frac{1}{2}\sum_\alpha\sum_{q,n_1,n_2}(n)C(q,n_1,n_2)\langle E_q,n_1,n_2|\psi_\alpha\rangle\sum_{\alpha'}\sum_{q',n_1',n_2'}C(q',n_1',n_2')\langle\psi_{\alpha'}|E_q',n_1',n_2'\rangle$$

$$\left.-\frac{1}{2}\sum_\alpha\sum_{q,n_1,n_2}C(q,n_1,n_2)\langle E_q,n_1,n_2|\psi_\alpha\rangle\sum_{\alpha'}\sum_{q',n_1',n_2'}(n'+1)C(q',n_1',n_2')\langle\psi_{\alpha'}|E_q',n_1',n_2'\rangle\right)\Gamma_{th}(B)\rho_{\alpha,\alpha'}.$$

$$(A.5)$$

From here we can see that all the dissipator terms can be cast into the same

form and gathered together, resulting in:

$$\dot{\rho}_{jk}(t) = -i\Omega_{jk}\rho_{jk}(t) + \sum_{\alpha,\alpha'} R_{j,k,\alpha,\alpha'}\rho_{\alpha,\alpha'}(t), \tag{A.6}$$

where the factors $R_{j,k,\alpha,\alpha'}$ contain the dissipation rates. This equation makes clear that the time evolution of element ρ_{jk} depends on its Hamiltonian solution plus contributions from every other element represented by the set α, α'. This is a complex set of coupled differential equations.

Bibliography

[1] V. Ameri, M. Eghbali-Arani, A. Mari, A. Farace, F. Kheirandish, V. Giovannetti, and R. Fazio, *Mutual information as an order parameter for quantum synchronization*, Physical Review A, 91 (2015).

[2] A. Baas, K. G. Lagoudakis, M. Richard, R. André, L. S. Dang, and B. Deveaud-Plédran, *Synchronized and desynchronized phases of exciton-polariton condensates in the presence of disorder*, Physical Review Letters, 100 (2008).

[3] C. Benedetti, F. Galve, A. Mandarino, M. G. Paris, and R. Zambrini, *Minimal model for spontaneous quantum synchronization*, Physical Review A - Atomic, Molecular, and Optical Physics, 94 (2016).

[4] D. Braak, *Integrability of the Rabi Model*, Physical Review Letters, 107 (2011).

[5] S. E. Bradforth, R. Jimenez, F. van Mourik, R. van Grondelle, and G. R. Fleming, *Excitation Transfer in the Core Light-Harvesting Complex (LH-1) of Rhodobacter sphaeroides: An Ultrafast Fluorescence Depolarization and Annihilation Study*, The Journal of Physical Chemistry, 99 (1995).

[6] H.-P. Breuer and F. Petruccione, *The Theory of Open Quantum Systems*, Oxford University Press, 2002.

[7] J. Buck and E. Buck, *Biology of Synchronous Flashing of Fireflies*, Nature, 211 (1966).

[8] R. BULLA, H.-J. LEE, N.-H. TONG, AND M. VOJTA, *Numerical renormalization group for quantum impurities in a bosonic bath*, Physical Review B, 71 (2005).

[9] R. BULLA, N. H. TONG, AND M. VOJTA, *Numerical renormalization group for bosonic systems and application to the sub-ohmic spin-boson model*, Physical Review Letters, 91 (2003).

[10] H. CHEN, X. WANG, A.-P. FANG, AND H.-R. LI, *Phonon-assisted excitation energy transfer in photosynthetic systems*, Chinese Physics B, 25 (2016).

[11] A. W. CHIN, J. PRIOR, R. ROSENBACH, F. CAYCEDO-SOLER, S. F. HUELGA, AND M. B. PLENIO, *The role of non-equilibrium vibrational structures in electronic coherence and recoherence in pigmentprotein complexes*, Nature Physics, 9 (2013).

[12] A. W. CHIN, . RIVAS, S. F. HUELGA, AND M. B. PLENIO, *Exact mapping between system-reservoir quantum models and semi-infinite discrete chains using orthogonal polynomials*, Journal of Mathematical Physics, 51 (2010).

[13] J. A. CINA AND G. R. FLEMING, *Vibrational Coherence Transfer and Trapping as Sources for Long-Lived Quantum Beats in Polarized Emission from Energy Transfer Complexes*, The Journal of Physical Chemistry A, 108 (2004).

[14] E. COLLINI, C. Y. WONG, K. E. WILK, P. M. G. CURMI, P. BRUMER, AND G. D. SCHOLES, *Coherently wired light-harvesting in photosynthetic marine algae at ambient temperature*, Nature, 463 (2010).

[15] T. M. H. CREEMERS, C. A. DE CARO, R. W. VISSCHERS, R. VAN GRONDELLE, AND S. VÖLKER, *Spectral Hole Burning and Fluorescence Line Narrowing in Subunits of the Light-Harvesting Complex LH1 of Purple Bacteria*, The Journal of Physical Chemistry B, 103 (1999).

[16] I. DE VEGA AND D. ALONSO, *Dynamics of non-Markovian open quantum systems*, Reviews of Modern Physics, 89 (2017).

[17] J. C. DEAN, T. MIRKOVIC, Z. S. TOA, D. G. OBLINSKY, AND G. D. SC-HOLES, *Vibronic Enhancement of Algae Light Harvesting*, Chem, 1 (2016).

[18] A. B. DOUST, C. N. MARAI, S. J. HARROP, K. E. WILK, P. M. CURMI, AND G. D. SCHOLES, *Developing a StructureFunction Model for the Cryptophyte Phycoerythrin 545 Using Ultrahigh Resolution Crystallography and Ultrafast Laser Spectroscopy*, Journal of Molecular Biology, 344 (2004).

[19] H.-G. DUAN, V. I. PROKHORENKO, R. J. COGDELL, K. ASHRAF, A. L. STEVENS, M. THORWART, AND R. J. D. MILLER, *Nature does not rely on long-lived electronic quantum coherence for photosynthetic energy transfer*, Proceedings of the National Academy of Sciences, 114 (2017).

[20] G. S. ENGEL, T. R. CALHOUN, E. L. READ, T.-K. AHN, T. MANČAL, Y.-C. CHENG, R. E. BLANKENSHIP, AND G. R. FLEMING, *Evidence for wavelike energy transfer through quantum coherence in photosynthetic systems*, Nature, 446 (2007).

[21] R. FRIESNER AND R. SILBEY, *Excitonphonon coupling in a dimer: An analytic approximation for eigenvalues and eigenvectors*, The Journal of Chemical Physics, 74 (1981).

[22] F. D. FULLER, J. PAN, A. GELZINIS, V. BUTKUS, S. S. SENLIK, D. E. WILCOX, C. F. YOCUM, L. VALKUNAS, D. ABRAMAVICIUS, AND J. P. OGILVIE, *Vibronic coherence in oxygenic photosynthesis*, Nature Chemistry, 6 (2014).

[23] F. GALVE, G. L. GIORGI, AND R. ZAMBRINI, *Entanglement dynamics of nonidentical oscillators under decohering environments*, Physical Review A, 81 (2010).

[24] F. GALVE, G. LUCA GIORGI, AND R. ZAMBRINI, *Quantum Correlations and Synchronization Measures*, in Lectures on General Quantum Correlations and their Applications, Springer, Cham, 2017.

[25] G. L. Giorgi, F. Galve, G. Manzano, P. Colet, and R. Zambrini, *Quantum correlations and mutual synchronization*, Physical Review A, 85 (2012).

[26] G. L. Giorgi, F. Galve, and R. Zambrini, *Probing the spectral density of a dissipative qubit via quantum synchronization*, Physical Review A, 94 (2016).

[27] G. L. Giorgi, F. Plastina, G. Francica, and R. Zambrini, *Spontaneous synchronization and quantum correlation dynamics of open spin systems*, Physical Review A, 88 (2013).

[28] H. Haken and G. Strobl, *An exactly solvable model for coherent and incoherent exciton motion*, Zeitschrift für Physik A Hadrons and nuclei, 262 (1973).

[29] E. Harel and G. S. Engel, *Quantum coherence spectroscopy reveals complex dynamics in bacterial light-harvesting complex 2 (LH2)*, Proceedings of the National Academy of Sciences, 109 (2012).

[30] L. Henderson and V. Vedral, *Classical, quantum and total correlations*, Journal of Physics A: Mathematical and General, 34 (2001).

[31] S. F. Huelga and M. B. Plenio, *Vibrations, quanta and biology*, Contemporary Physics, 54 (2013).

[32] K. H. Hughes, C. D. Christ, and I. Burghardt, *Effective-mode representation of non-Markovian dynamics: A hierarchical approximation of the spectral density. I. Application to single surface dynamics*, The Journal of Chemical Physics, 131 (2009).

[33] M. R. Hush, W. Li, S. Genway, I. Lesanovsky, and A. D. Armour, *Spin correlations as a probe of quantum synchronization in trapped-ion phonon lasers*, Physical Review A, 91 (2015).

[34] J. ILES-SMITH, N. LAMBERT, AND A. NAZIR, *Environmental dynamics, correlations, and the emergence of noncanonical equilibrium states in open quantum systems*, Physical Review A, 90 (2014).

[35] A. ISHIZAKI AND G. R. FLEMING, *Unified treatment of quantum coherent and incoherent hopping dynamics in electronic energy transfer: Reduced hierarchy equation approach*, The Journal of Chemical Physics, 130 (2009).

[36] A. ISHIZAKI AND Y. TANIMURA, *Quantum Dynamics of System Strongly Coupled to Low-Temperature Colored Noise Bath: Reduced Hierarchy Equations Approach*, Journal of the Physical Society of Japan, 74 (2005).

[37] J. JIN, X. ZHENG, AND Y. YAN, *Exact dynamics of dissipative electronic systems and quantum transport: Hierarchical equations of motion approach*, The Journal of Chemical Physics, 128 (2008).

[38] A. KELL, X. FENG, M. REPPERT, AND R. JANKOWIAK, *On the Shape of the Phonon Spectral Density in Photosynthetic Complexes*, The Journal of Physical Chemistry B, 117 (2013).

[39] A. KOLLI, E. J. OREILLY, G. D. SCHOLES, AND A. OLAYA-CASTRO, *The fundamental role of quantized vibrations in coherent light harvesting by cryptophyte algae*, The Journal of Chemical Physics, 137 (2012).

[40] T. E. LEE AND H. R. SADEGHPOUR, *Quantum synchronization of quantum van der Pol oscillators with trapped ions*, Physical Review Letters, 111 (2013).

[41] H. LIU, L. ZHU, S. BAI, AND Q. SHI, *Reduced quantum dynamics with arbitrary bath spectral densities: Hierarchical equations of motion based on several different bath decomposition schemes*, The Journal of Chemical Physics, 140 (2014).

[42] N. LÖRCH, E. AMITAI, A. NUNNENKAMP, AND C. BRUDER, *Genuine Quantum Signatures in Synchronization of Anharmonic Self-Oscillators*, Physical Review Letters, 117 (2016).

[43] N. LÖRCH, S. E. NIGG, A. NUNNENKAMP, R. P. TIWARI, AND C. BRUDER, *Quantum Synchronization Blockade: Energy Quantization Hinders Synchronization of Identical Oscillators*, Physical Review Letters, 118 (2017).

[44] G. MANZANO, F. GALVE, G. L. GIORGI, E. HERNÁNDEZ-GARCÍA, AND R. ZAMBRINI, *Synchronization, quantum correlations and entanglement in oscillator networks.*, Scientific Reports, 3 (2013).

[45] G. MANZANO, F. GALVE, AND R. ZAMBRINI, *Avoiding dissipation in a system of three quantum harmonic oscillators*, Physical Review A, 87 (2013).

[46] R. MARTINAZZO, B. VACCHINI, K. H. HUGHES, AND I. BURGHARDT, *Communication: Universal Markovian reduction of Brownian particle dynamics*, The Journal of Chemical Physics, 134 (2011).

[47] V. MAY AND O. KÜHN, *Electronic and Vibrational Molecular States*, in Charge and Energy Transfer Dynamics in Molecular Systems, Wiley-VCH Verlag GmbH & Co. KGaA, 2011.

[48] B. MILITELLO, H. NAKAZATO, AND A. NAPOLI, *Synchronizing quantum harmonic oscillators through two-level systems*, Physical Review A, 96 (2017).

[49] K. MODI, *A Pedagogical Overview of Quantum Discord*, Open Systems & Information Dynamics, 21 (2014).

[50] I. NITSAN, S. DRORI, Y. E. LEWIS, S. COHEN, AND S. TZLIL, *Mechanical communication in cardiac cell synchronized beating*, Nature Physics, 12 (2016).

[51] A. NITZAN, *Chemical Dynamics in Condensed Phases: Relaxation, Transfer, and Reactions in Condensed Molecular Systems*, Oxford Graduate Texts, 2006.

[52] F. NOVELLI, A. NAZIR, G. H. RICHARDS, A. ROOZBEH, K. E. WILK, P. M. G. CURMI, AND J. A. DAVIS, *Vibronic Resonances Facilitate Excited-State Coherence in Light-Harvesting Proteins at Room Temperature*, Journal of Physical Chemistry Letters, 6 (2015).

[53] V. I. NOVODEREZHKIN, A. B. DOUST, C. CURUTCHET, G. D. SCHOLES, AND R. VAN GRONDELLE, *Excitation dynamics in phycoerythrin 545: Modeling of steady-state spectra and transient absorption with modified redfield theory*, Biophysical Journal, 99 (2010).

[54] V. I. NOVODEREZHKIN, M. A. PALACIOS, H. VAN AMERONGEN, AND R. VAN GRONDELLE, *Energy-Transfer Dynamics in the LHCII Complex of Higher Plants: Modified Redfield Approach* , The Journal of Physical Chemistry B, 108 (2004).

[55] H. OLLIVIER AND W. H. ZUREK, *Quantum Discord: A Measure of the Quantumness of Correlations*, Physical Review Letters, 88 (2002).

[56] C. M. ORALLO, I. CARUGATI, P. G. DONATO, AND S. MAESTRI, *Study on Single-bin Sliding DFT algorithms: Comparison, stability issues and frequency adaptivity*, Measurement: Journal of the International Measurement Confederation, 69 (2015).

[57] E. J. O'REILLY, *Quantum Traits in the Dynamics of Biomolecular Systems*, PhD thesis, UCL (University College London), 2014.

[58] E. J. OREILLY AND A. OLAYA-CASTRO, *Non-classicality of the molecular vibrations assisting exciton energy transfer at room temperature*, Nature Communications, 5 (2014).

[59] G. PANITCHAYANGKOON, D. V. VORONINE, D. ABRAMAVICIUS, J. R. CARAM, N. H. C. LEWIS, S. MUKAMEL, AND G. S. ENGEL, *Direct evidence of quantum transport in photosynthetic light-harvesting complexes*, Proceedings of the National Academy of Sciences, 108 (2011).

[60] E. J. G. PETERMAN, T. PULLERITS, R. VAN GRONDELLE, AND H. VAN AMERONGEN, *ElectronPhonon Coupling and Vibronic Fine Structure of Light-Harvesting Complex II of Green Plants: Temperature Dependent Absorption and High-Resolution Fluorescence Spectroscopy*, The Journal of Physical Chemistry B, 101 (1997).

[61] A. PIKOVSKY, M. ROSENBLUM, AND J. KURTHS, *Synchronization*, Cambridge University Press, 2001.

[62] J. PRIOR, A. W. CHIN, S. F. HUELGA, AND M. B. PLENIO, *Efficient Simulation of Strong System-Environment Interactions*, Physical Review Letters, 105 (2010).

[63] H. QIU, R. ZAMBRINI, A. POLLS, J. MARTORELL, AND B. JULIÁ-DÍAZ, *Hybrid synchronization in coupled ultracold atomic gases*, Physical Review A, 92 (2015).

[64] T. RENGER, *Theory of Optical Spectra Involving Charge Transfer States: Dynamic Localization Predicts a Temperature Dependent Optical Band Shift*, Physical Review Letters, 93 (2004).

[65] G. H. RICHARDS, K. E. WILK, P. M. G. CURMI, H. M. QUINEY, AND J. A. DAVIS, *Coherent vibronic coupling in light-harvesting complexes from photosynthetic marine algae*, Journal of Physical Chemistry Letters, 3 (2012).

[66] B. S. ROLCZYNSKI, H. ZHENG, V. P. SINGH, P. NAVOTNAYA, A. R. GINZBURG, J. R. CARAM, K. ASHRAF, A. T. GARDINER, S.-H. YEH, S. KAIS, R. J. COGDELL, AND G. S. ENGEL, *Correlated Protein Environments Drive Quantum Coherence Lifetimes in Photosynthetic Pigment-Protein Complexes*, Chem, 4 (2018).

[67] E. ROMERO, R. AUGULIS, V. I. NOVODEREZHKIN, M. FERRETTI, J. THIEME, D. ZIGMANTAS, AND R. VAN GRONDELLE, *Quantum coherence in photosynthesis for efficient solar-energy conversion*, Nature Physics, 10 (2014).

[68] G. C. SCHATZ AND M. A. RATNER, *Correlation Functions and Dynamical Processes: Nonadiabatic Intramolecular Electron Transfer*, in Quantum Mechanics in Chemistry, Dover Publications, 2002, ch. 10.

[69] C. SCHINABECK, R. HÄRTLE, AND M. THOSS, *Hierarchical quantum master equation approach to electronic-vibrational coupling in nonequilibrium transport through nanosystems: Reservoir formulation and application to vibrational instabilities*, Physical Review B, 97 (2018).

[70] Y. L. SHEN AND Y. Q. TU, *Correlation theory-based signal processing method for CMF signals*, Measurement Science and Technology, 27 (2016).

[71] Y. L. SHEN, Y. Q. TU, L. J. CHEN, AND T. A. SHEN, *Phase difference estimation method based on data extension and Hilbert transform*, Measurement Science and Technology, 26 (2015).

[72] Q. SHI, L. CHEN, G. NAN, R.-X. XU, AND Y. YAN, *Efficient hierarchical Liouville space propagator to quantum dissipative dynamics*, The Journal of Chemical Physics, 130 (2009).

[73] R. SILBEY AND R. A. HARRIS, *Variational calculation of the dynamics of a two level system interacting with a bath*, The Journal of Chemical Physics, 80 (1984).

[74] R. J. SILBEY, D. A. BRYANT, G. D. SCHOLES, D. B. TURNER, K. E. WILK, R. M. ALVEY, P. M. G. CURMI, AND C. Y. WONG, *Electronic coherence lineshapes reveal hidden excitonic correlations in photosynthetic light harvesting*, Nature Chemistry, 4 (2012).

[75] S. SIWIAK-JASZEK AND A. OLAYA-CASTRO, *Transient synchronisation and quantum coherence in a bio-inspired vibronic dimer*, Faraday Discussions, (2019).

[76] R. STONES, *Electron Counting Statistics of Open Quantum Systems*, PhD thesis, University College London (UCL), 2017.

[77] J. STRÜMPFER AND K. SCHULTEN, *Light harvesting complex II B850 excitation dynamics*, The Journal of Chemical Physics, 131 (2009).

[78] Y. TANIMURA, *Stochastic Liouville, Langevin, FokkerPlanck, and Master Equation Approaches to Quantum Dissipative Systems*, Journal of the Physical Society of Japan, 75 (2006).

[79] Y. TANIMURA, *Reduced hierarchy equations of motion approach with Drude plus Brownian spectral distribution: Probing electron transfer processes by means of two-dimensional correlation spectroscopy*, The Journal of Chemical Physics, 137 (2012).

[80] Y. TANIMURA AND R. KUBO, *Time Evolution of a Quantum System in Contact with a Nearly Gaussian-Markoffian Noise Bath*, Journal of the Physical Society of Japan, 58 (1989).

[81] L. VIANI, M. CORBELLA, C. CURUTCHET, E. J. O'REILLY, A. OLAYA-CASTRO, AND B. MENNUCCI, *Molecular basis of the excitonphonon interactions in the PE545 light-harvesting complex*, Phys. Chem. Chem. Phys., 16 (2014).

[82] P. VÖHRINGER, R. A. WESTERVELT, T.-S. YANG, D. C. ARNETT, M. J. FELDSTEIN, AND N. F. SCHERER, *Solvent and frequency dependence of vibrational dephasing on femtosecond time-scales*, Journal of Raman Spectroscopy, 26 (1995), pp. 535–551.

[83] S. WALTER, A. NUNNENKAMP, AND C. BRUDER, *Quantum Synchronization of a Driven Self-Sustained Oscillator*, Physical Review Letters, 112 (2014).

[84] S. WALTER, A. NUNNENKAMP, AND C. BRUDER, *Quantum synchronization of two Van der Pol oscillators*, Annalen der Physik, 527 (2015).

[85] M. WENDLING, M. A. PRZYJALGOWSKI, S. I. E. VULTO, T. J. AARTSMA, R. V. GRONDELLE, AND H. V. AMERONGEN, *Electron - Vibrational Coupling in the Fenna - Matthews - Olson Complex of Prosthecochloris aestuarii*

Determined by Temperature-Dependent Absorption and Fluorescence Line-Narrowing Measurements, The Journal of Physical Chemistry B, 104 (2000).

[86] D. WITTHAUT, S. WIMBERGER, R. BURIONI, AND M. TIMME, *Classical synchronization indicates persistent entanglement in isolated quantum systems*, Nature Communications, 8 (2017).

[87] J. M. WOMICK AND A. M. MORAN, *Vibronic Enhancement of Exciton Sizes and Energy Transport in Photosynthetic Complexes*, The Journal of Physical Chemistry B, 115 (2011).

[88] M. P. WOODS, R. GROUX, A. W. CHIN, S. F. HUELGA, AND M. B. PLENIO, *Mappings of open quantum systems onto chain representations and Markovian embeddings*, Journal of Mathematical Physics, 55 (2014).

[89] M. WOUTERS, *Synchronized and desynchronized phases of coupled nonequilibrium exciton-polariton condensates*, Physical Review B, 77 (2008).

[90] M. ZHANG, G. S. WIEDERHECKER, S. MANIPATRUNI, A. BARNARD, P. MCEUEN, AND M. LIPSON, *Synchronization of Micromechanical Oscillators Using Light*, Physical Review Letters, 109 (2012).

[91] B. ZHU, J. SCHACHENMAYER, M. XU, F. HERRERA, J. G. RESTREPO, M. J. HOLLAND, AND A. M. REY, *Synchronization of interacting quantum dipoles*, New Journal of Physics, 17 (2015).

[92] L. ZHU, H. LIU, W. XIE, AND Q. SHI, *Explicit system-bath correlation calculated using the hierarchical equations of motion method*, The Journal of Chemical Physics, 137 (2012).